SYNTHESIS AND PROPERTIES OF NANOTWINNED SILVER AND ALUMINUM

A Dissertation

by

DANIEL CHARLES BUFFORD

Submitted to the Office of Graduate Studies of
Texas A&M University
in partial fulfillment of the requirements for the degree of

DOCTOR OF PHILOSOPHY

Approved by:

Chair of Committee,	Xinghang Zhang
Committee Members,	Tahir Cagin
	Ibrahim Karaman
	Haiyan Wang
Intercollegiate Faculty Chair,	Ibrahim Karaman

August 2013

Major Subject: Materials Science and Engineering

ABSTRACT

Recent studies of fcc metals with dense twins (~10 nm spacing) have revealed impressive mechanical properties, along with improved ductility and electrical conductivity in comparison to nanocrystalline metals with similar feature sizes. Many important fcc metals could benefit from these "nanotwinned" microstructures, however, not all fcc metals readily form such twins. The tendency of fcc metals to form twin boundaries is related to the twin boundary energy; those with low twin boundary energy, such as silver (Ag), easily form twins. Increasing twin boundary energy interferes with twin formation, to the point that in metals with high twin boundary energy, like aluminum (Al), twins are quite rare. This thesis focuses on the synthesis of nanotwinned Ag and Al via physical vapor deposition. Nanotwinned Ag is readily fabricated, however, a template approach had to be developed to induce twins in Al. The microstructures and their relationships to observed mechanical properties are also discussed.

Grain boundaries interfere with dislocation transmission by posing a slip system discontinuity between grains. Twin boundaries are a special class of grain boundaries in which the grains on either side of the boundary are related by mirror symmetry. Twin boundaries inhibit dislocation transmission, providing strength in the same manner as grain boundaries. However, their symmetrical structure reduces the free volume and grain boundary energy. Accordingly, coherent twin boundaries are often more energetically stable than grain boundaries, and their coherency allows plasticity mechanisms to remain active under conditions where such mechanisms may be inhibited at grain boundaries. Hence, twin

boundaries may provide a metal with unique combinations of high strength and good ductility, conductivity, and thermal stability.

DEDICATION

This thesis is dedicated to:

The memory of my grandparents, William and Laurine, Aloyse and Marie

My parents, Charles and Martha

My brothers, Joseph and Matthew

and to Katherine

ACKNOWLEDGEMENTS

First, I must thank my advisor, Dr. Xinghang Zhang for his support, guidance, and encouragement during my studies here at Texas A&M University. I thank my committee members, Drs. Tahir Cagin, Ibrahim Karaman, and Haiyan Wang for challenging me to produce great results in the pursuit of my degree. Additional thanks goes to Dr. Wang for the use of her laboratory facilities.

I greatly appreciate the Mechanical Engineering department staff at Texas A&M University, and I am indebted to the Materials Science and Engineering program coordinator, Jan Gerston, who guided me through my graduate studies, starting before I was even admitted to the University.

I want to thank my collaborators from the Wang group, Yuanyuan Zhu, and from Los Alamos National Laboratory, Drs. Zhenxing Bi and Quanxi Jia, for their direct contributions to this work. I want to thank former Zhang research group members, Drs. Osman Anderoglu, Engang Fu, and Nan Li for their guidance as I began my graduate school career. I also want to thank my friends and coworkers, Steven Rios, Dr. Kaiyuan Yu, Yue Liu, Youxing Chen, Byoungsoo Ham, Dr. Cheng Sun, David Foley, Shreyas Balachandran, Zach Levin, and Michael Martin for contributions during meeting discussions, support when working late at night and taking classes, and in general, their companionship through my graduate school journey.

Finally, I want to thank my parents, Chuck and Martha, brothers, Joe and Matt, and Katie for their constant support and understanding throughout the past years.

I acknowledge funding from the National Science Foundation's Division of Materials Research (NSF-DMR) grant program, without which this work would not have been possible. I acknowledge the Center for Integrated Nanotechnologies (CINT) at Los Alamos for use of their facilities, and the National Center for Electron Microscopy (NCEM) for the use of their microscopes. I also acknowledge the Texas A&M University Microscopy Center and Materials Characterization Facility for the use of numerous microscopes and other instruments.

NOMENCLATURE

Ag	Silver
Al	Aluminum
Ar	Argon
CTB	Coherent twin boundary
CVD	Chemical vapor deposition
DC	Direct current
fcc	Face-centered cubic
HAADF-STEM	High-angle annular dark field scanning transmission electron microscopy
ITB	Incoherent twin boundary
MD	Molecular dynamics
nc	Nanocrystalline
nt	Nanotwinned
PVD	Physical vapor deposition
RF	Radio frequency
SAD	Selected area electron diffraction
Si	Silicon
T	Twinning tendency
TEM	Transmission electron microscopy
T_m	Melting temperature

ufg	Ultra-fine grained
W	Watts

TABLE OF CONTENTS

LIST OF FIGURES

CHAPTER I

INTRODUCTION

I.1 Historical perspective

Over centuries of practicing their craft, blacksmiths and other metalworkers developed an intuitive knowledge of strength in metals. Some metals were innately stronger than others were, while some could be made stronger by processes such as working, quenching, and alloying. The development of first copper, then bronze, then iron and steel for use in tools and weapons fostered the rise of civilization. A wealth of knowledge developed over time of how metals could be chosen and processed working, quenching, or alloying to suit specific applications.

I.1.1 Size dependent strengthening

However, it is only within the last century that the physical mechanisms behind such strengthening have come to light. For a given metal, the microstructure is perhaps the most important aspect to consider when investigating its strength. Various features within the microstructure—grain boundaries, dislocations, precipitates, among others—interact with dislocations during plastic deformation, and have profound effects on the mechanical properties. The well-known Taylor and Hall-Petch strengthening models were among the first to quantify the concept of introducing barriers to dislocation motion as a method to increase strength. The Hall-Petch model;

$$\sigma_y = \sigma_0 + kd^{-n} \qquad \text{Equation 1}$$

was first empirically derived for steels. Here σ_y is the yield strength, σ_0 is the friction stress, k is the Hall-Petch slope, d is the grain size, and n is a constant typically ~0.5 [1-2]. In the equation above, σ_0 represents the contribution from the flow stress. The most famous aspect of this relationship is the $kd^{-1/2}$ dependence; k represents the resistance of the grain boundaries to dislocation transmission, while the d^{-n} dependence quantifies the contribution from grain boundary density. The Hall-Petch relationship may also be expressed in terms of material parameters by considering the case of dislocations emitted from a source piling up against a barrier, e.g. a grain boundary:

$$\Delta\sigma_y = M\left[\tau_0 + \left(\frac{\tau^*\mu b}{\pi(1-\nu)L}\right)^n\right]. \qquad \text{Equation 2}$$

Here, M is the Taylor factor, τ_0 is the lattice friction stress, τ^* is the critical stress required for cross slip across a grain boundary, μ is the shear modulus, b is Burgers vector, ν is Poisson's ratio, and L is the distance from a dislocation source to the grain boundary [3]. The most useful part of this form is that the contribution from k is expressed in terms of material parameters, shedding more light on factors contributing to strength. The Hall-Petch relation considers two-dimensional defects that essentially pose as walls for dislocations to penetrate.

A dispersed network of obstacles will also pin dislocations as they pass by. The Taylor dispersed barrier strengthening model

$$\Delta\sigma_y = \mu b\sqrt{\rho}\ , \qquad \text{Equation 3}$$

is used to quantify the contribution from such a network of defects. Here ρ is the barrier density. In practice, the obstacles are microstructure features like dislocation loops or precipitate particles embedded in larger grains. These relations describe two major strengthening mechanisms in metals, and have proved to be enormously useful for their predictive power in determining strength. In the decades following these famous early models, many more strengthening models have been developed; these include refinements to Equations 1 and 3, as well as other formulations that include the influence of numerous rate, temperature, direction, and structure dependent factors, just to name a few. However, the propagation of dislocations through various types of barriers remains of central importance to the deformation of metals.

As indicated by Equations 2 and 3, increasing the density of obstacles in the form of grain boundaries or dislocations corresponds to increases in strength. For the case of dispersed barrier hardening, this may be a result of increasing the size or density of precipitate particles or cold working to increase dislocation density. For grain boundary strengthening, increasing barrier density means decreasing grain size. Refinement of grain size has been of great importance to the development of higher strength metals. The Hall-Petch relation often holds well for grain size reduction from grains exceeding the millimeter range (10^{-3} m) in cast or annealed billets to grains just below the micrometer range (10^{-6} m). However, as grain size is reduced below several hundred nanometers the behavior tends to become more complicated.

I.1.2 Strengthening at the nanoscale

Richard Feynman's 1959 talk "There's Plenty of Room at the Bottom" famously outlined the incredible amount of room available in which to work when materials are miniaturized to the nanometer range (10^{-9} m) [4]. For readers unfamiliar with this length scale, the width of a human hair typically ranges from 10-100 micrometers; a hair is thus 1,000 to 10,000 times wider than 1 nanometer. Material behavior at the nanometer scale differs from bulk material in two major ways; (1) it is possible to incorporate microstructure features at incredible densities and (2) interfacial effects that are insignificant at large length scales come to dominate behavior. In the particular case of solids with nanometer scale grains, surface and interface effects come to dominate the behavior.

For metals, interesting effects begin to appear upon reduction of grain size to below ~100 nm. At this point the material enters the so-called nanocrystalline (nc) regime, and often changes in material behavior occur. (As a side note the term “nanocrystalline” is often applied to metals with grains in the 1-100 nm range. Metals with 100-1000 nm grains are often termed “ultra-fine grained” (ufg), however, there is some overlap in terminology among various authors, and sometimes the terms are used essentially interchangeably.) Different authors have developed varying criteria to define nc metals, however one agreed-upon hallmark is certain; grain boundaries may approach densities of 10^{19} cm^{-3} [5], and interfacial interactions influence a large fraction of atoms in the microstructure. As an example, the fraction of atoms comprising grain boundaries may be ~3% in a 100 nm grain metal, rising to ~30% for 10 nm grains, and ~50% for 5 nm grains [6]. This grain boundary density can result in activation of dramatically different mechanisms for plasticity, as well as macroscopically observable changes, such as measureable decreases of density in comparison to the bulk material [7].

The Hall-Petch relation (Equation 1) predicts dramatic strengthening upon entering the nc regime due to the $d^{-1/2}$ dependence of the yield strength. Indeed, nc metals often exhibit dramatically higher yield strength in comparison to their coarser-grained counterparts [8]. This high strength is a major reason that nc metals have received so much attention in recent decades. However, the singularity approached as $d \rightarrow 0$ is not seen; often a saturation in strengthening or even softening may occur at very small d.

Unfortunately, nc metals may also exhibit degradation of other properties as a result of such high grain boundary density. While the effect is negligible in larger grained metals, the mismatched atoms along the dense grain boundaries in nc metals creates measureable amounts of porosity, which in turn can result in reduced elastic modulus [9]. In fully dense nc metals, this reduction in modulus is seen at grain sizes of ~10 nm or smaller [10]. More importantly, ductility of nc metals is often low, as a result of several factors: (1) artifacts from processing (porosity), (2) tensile instability, or (3) crack nucleation or shear instability [11]. Dislocation-mediated plasticity can be suppressed at small length scales, leading to strain localization and reducing elongation to failure in macroscopic specimens, especially at room temperature or below. Hence, in nc metals unusual mechanisms (e.g. grain boundary shear, sliding, and grain rotation) may be activated to accommodate strain [8]. Some studies have reported a reversal of the Hall-Petch slope at nanometer length scales, but there is some question as to whether this is a result of a change in deformation mechanisms at fine grain sizes, or a result of loss of density [8]. The mismatch associated with grain boundaries, corresponds to stored energy. In nc metals, the high grain boundary density gives a very high stored energy content. Thermal stability may also suffer, as there is a large driving force to release energy stored in high-density grain boundaries via grain growth.

The attractiveness of high strength nc metals and their issues with ductility and thermal stability have driven researchers to attempt to solve these problems by various means, for instance, by segregation of chemical species at grain boundaries [12]. This thesis focuses on a different means. Here grain boundary engineering strategies, in which the type and orientation of boundaries in the metal are controlled to manipulate material properties, are considered. In particular, we will focus on twin boundaries.

I.2 Twin boundary structure

The term "twin" boundary refers to a special class of grain boundaries in which the lattices on either side are related by mirror symmetry across the so-called twinning plane. An essentially infinite number of twinning planes could theoretically be specified for an infinitely large crystal. However, in practice only a few twinning planes are typically observed for a given crystal structure, as it is usually easier to generate twins on lower-index planes. Common twinning planes vary from one crystal structure to the next. For fcc metals like the ones in this work, two kinds of twin boundaries are most important: the $\Sigma3\{111\}$ coherent twin boundary (CTB) and $\Sigma3\{112\}$ incoherent twin boundary (ITB).

The $\Sigma3\{111\}$ coherent twin boundary can be visualized by cleaving a perfect crystal on a $\{111\}$ plane, rotating one of the pieces 180° about the corresponding $<111>$ axis, then rejoining the pieces. The structure of such a boundary appears in Figure 1.

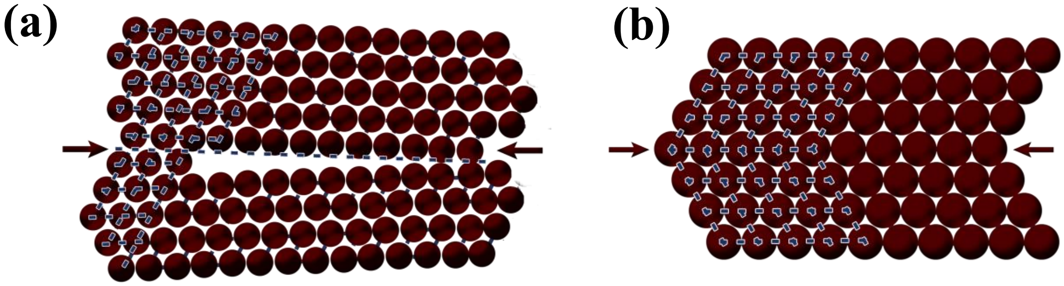

Figure 1: Schematic comparison of (a) a generic grain boundary and (b) a Σ3{111} coherent twin boundary viewed from a <110> zone axis.

Comparing the grain boundary and twin boundary schematics in Figure 1, it is immediately apparent that CTBs have a more coherent structure. These boundaries may form via deformation, annealing, or growth processes.

The Σ3{112} incoherent twin boundary is similarly visualized by cleaving a crystal on a {111} plane, then rotating 180° about the orthogonal <111> axis, then rejoining the two pieces. The configuration of this boundary is more complicated, as the boundary is not a direct match as it is in the CTB case. Instead, the smallest repeating structural unit of the boundary can be described as three successive {111} planes, with each plane displaced by a Burgers vector, which are related such that the sum of the vectors is zero. Hence, the boundary is made of repeating stacks of triplets. This structure appears below in Figure 2.

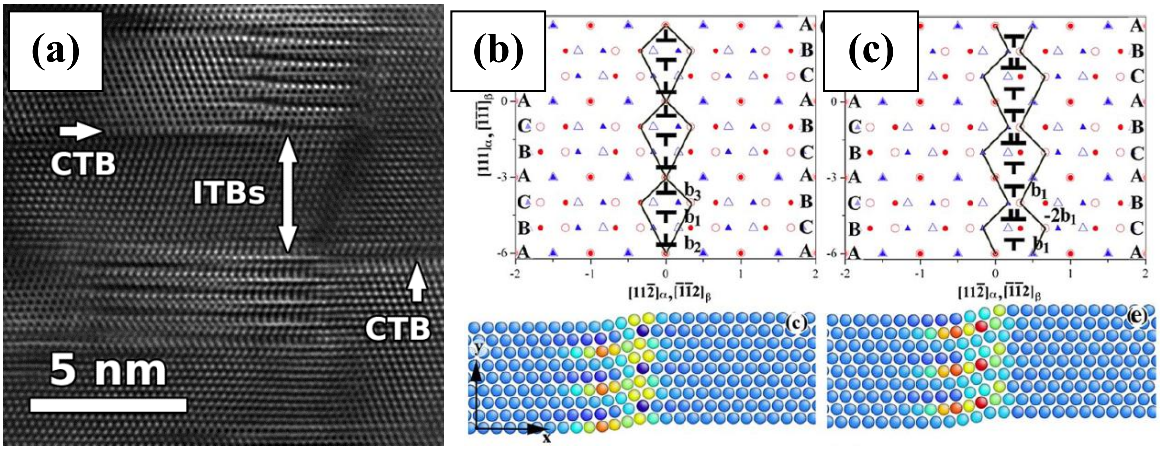

Figure 2: (a) Cross-section view TEM micrograph (from <110> zone axis) showing several CTBs and ITBs. The schematic (b) shows the dislocation structure associated with the ITB, while (c) shows a more widely dissociated form of the boundary caused by shear stress [13].

Alternatively, the ITB structure can be described as a 9R phase, and such boundaries have been observed previously in several fcc metals; e.g. Cu, Ag, Au, and in specially fabricated Al bicrystals [14-19]. The stable width of ITBs depends on several factors. First, the stacking fault energy (γ_{sf}) of the parent metal is important, as the structure of the boundary is essentially an array of stacking defects. Hence, an ITB is expected to be wider in low γ_{sf} metals, and narrower in higher γ_{sf} metals. Additionally, applied stress also may cause the ITB to dissociate, i.e. become wider. This dissociation occurs by the emission of stacking faults by the boundary [20].

CTB and ITB segments can join together to form a boundary structure separating twin and matrix variants on either side [21]. In nt metal films and foils formed by deposition processes, ITBs typically extend in the growth direction, which is usually the <111> direction, while CTBs form on the same {111} plane. Hence, CTB and ITB segments extend in perpendicular directions.

Twin boundaries, especially CTBs, are much different from other grain boundaries in that they have less free volume and disrupt the crystal structure less. In turn, the grain boundary energies associated with CTBs, ITBs, and more conventional high- and low-angle grain boundaries differ dramatically. For example, in Cu, the CTB, ITB, and high angle grain boundary energies are 24-39, 590-714, and 625-710 mJ/m^2, respectively [13, 22-23]. In nt metals, the CTB energy is often the lowest energy grain boundary present by a large margin, making CTBs much more stable than many other grain boundaries.

I.2.1 Twin boundary / dislocation interactions

The slip system discontinuity across a twin boundary is analogous to the discontinuity across conventional grain boundaries. Qualitatively, twin boundaries behave similarly to grain boundaries in that they both pose obstacles to dislocation transmission; dislocations must cross slip across the twin boundary in order to travel from the matrix to the twin variant. Different computational simulation techniques have proved to be valuable in probing these interactions. The simplest case considers the interaction of single dislocations with grain boundaries.

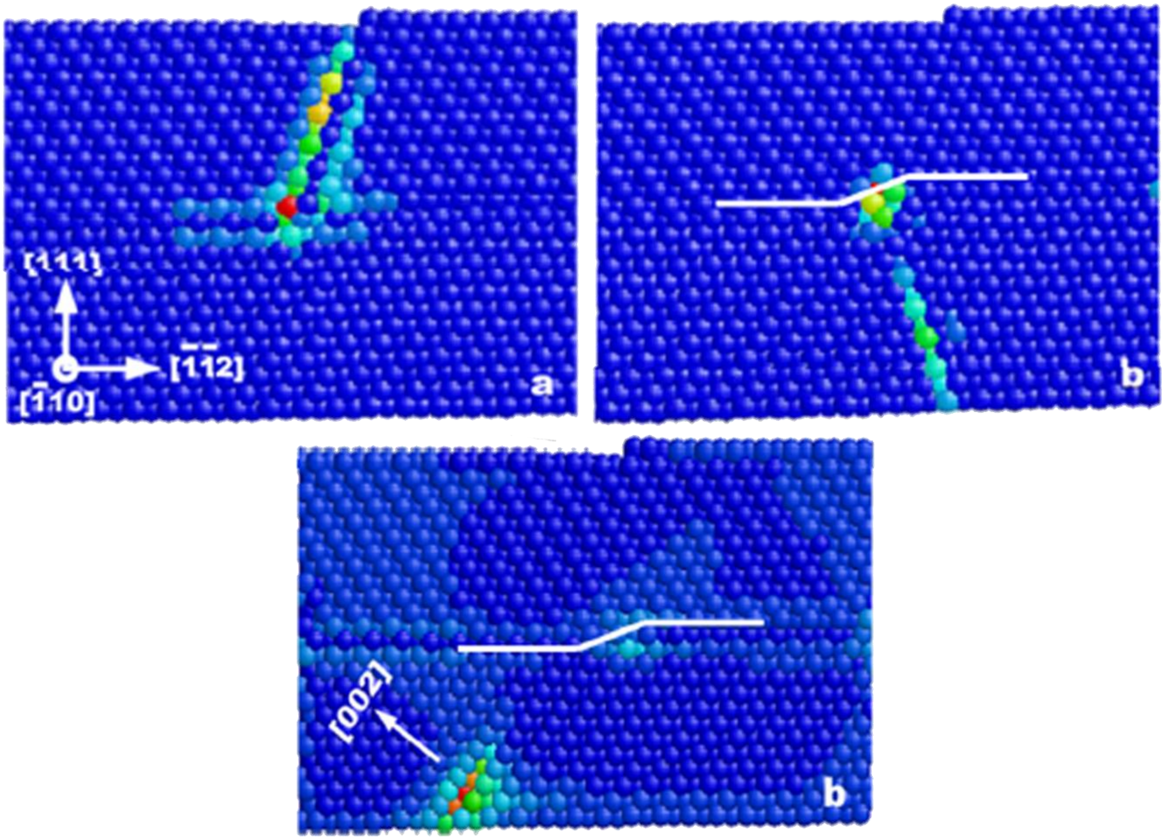

Figure 3: Molecular dynamics simulations of CTB/dislocation interactions during cross slip events [24-25].

Figure 3 shows the interactions between a single dislocation and twin boundary under pure shear and tension in Ni, as simulated by MD [24-25]. This interaction is vital to strengthening, as dislocation cross-slip across grain boundaries is at the heart of the Hall-Petch relation. Initially, a dislocation with b = ½ [101] resided on a matrix {111} plane at the top of the simulation cell (Figure 3a). After application of shear stress, the dislocation eventually cross slipped across the twin boundary onto the complementary twin {111} plane, leaving a Shockley partial dislocation on the twin boundary. A large applied shear stress of 1.77 GPa was necessary to initiate this cross slip. In tension, even larger stress was necessary. From the same starting point, an applied biaxial shear stress of 3 GPa (parallel to the interface) resulted in the dislocation cross slipping onto an unusual {200} plane, while depositing a residual dislocation along the boundary. Note that the simulations in Figure 3 investigate a simple case of a single dislocation slipping across a CTB. Other computational studies have investigated other interactions between dislocations and twin boundaries Figure 4.

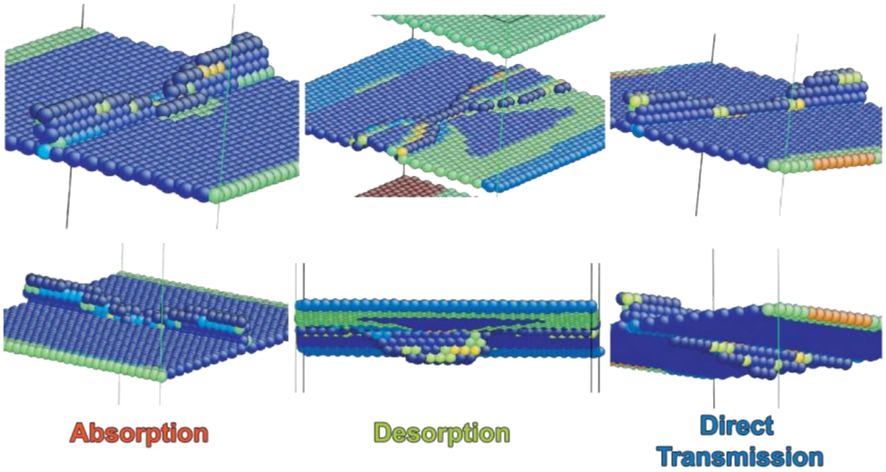

Figure 4: MD simulations showing different dislocation/twin boundary interactions; absorption and re-emission, as well as direct slip transmission [26].

As seen above, dislocations and twin boundaries may interact in several different ways. The most obvious interactions include direct transmission or absorption within the boundary, however more complicated reactions may occur in which the dislocations dissociate. The specific interaction depends on the type of dislocation (screw vs. non screw), magnitude and direction of the applied stress, as well as material parameters (stable and unstable γ_{sf} and twin boundary energy, γ_{tb}) [27-28]. Again, these studies predicted the nucleation of dislocations along the twin boundary as a result of transmission, as well as the formation of locks.

$\Sigma3\{112\}$ ITBs have also been the subject of computational investigations. Interestingly, ITBs may migrate under an applied stress due to activation of glide of the partial dislocations comprising the ITB [29]. This twin boundary migration process is important for nt metals. Since an ITB separates twin and matrix variants, its motion converts the variant in front of it into the other variant. Depending on the direction of motion, ITB migration may extend or remove a twin variant, a process known as detwinning. ITB migration may affect twin density, and therefore the mechanical properties of the metal. The driving force for such migration has been predicted as $2\gamma_t/t$, that is, thinner twins move more easily than thicker ones [29].

Simulation techniques were first noted in this section, as they are useful tools for probing dislocation/twin boundary interactions on the atomic scale. Other studies have probed twin boundary/dislocation interactions experimentally. Often this is done by post-deformation TEM studies [30-33]. However, some more recent *in situ* observations performed inside of the TEM have revealed the interactions of single dislocations with twin boundaries [34-38]. These various studies have elucidated the types of dislocation reactions that may occur during cross slip at twin boundaries.

I.2.2 Larger scale simulation results

Some simulations have sought to elucidate material behavior on a larger scale by considering interactions among multiple twin boundaries and grain boundaries. Some simulations are interesting in that some have predicted unusual phenomena in nt metals, while others have helped clarify what happens as nt metals are deformed. Simulations of polycrystalline nt metals predicted the unexpected nucleation of deformation twins in Al [39-40]. The mechanical behavior of various nt metals as a function of γ_{sf} has been investigated by computational means as well [41]. CTBs in Al are predicted to have lower shear strength than in Ag, Cu, or Pd. In simulations of nc Al, Cu, and Ni, the presence or absence of preexisting twins was predicted to influence the dominant deformation mechanisms, i.e. whether twin boundary migration might be active or not [42-43].

Some studies have suggested a softening effect at very fine twin spacing due to a switch from dislocation pile-up dominated behavior to dislocation nucleation dominated behavior [44]. This study suggested that the transition point from one deformation regime to the next is dependent upon the grain size as well as the twin spacing, with finer grain size needing thinner twins to initiate softening. Another study found that the stress response of twin boundaries is highly anisotropic depending on the orientation of the stress relative to the twin boundary [45]. Hence, in polycrystalline nt metals twin boundaries may contribute to strength by blocking dislocations when stress is more perpendicular to the boundary, while contributing to plasticity by more easily deforming in response to stress parallel to the boundary.

Other studies have investigated the effects of twin boundaries on novel nanostructured materials. Several studies have used MD simulations to simulate deformation of twinned nanowires under mechanical deformation [46-47]. Here, perfect dislocations deposited a glissile dislocation on the twin boundary during cross-slip, while a perfect dislocation was also emitted onto an unusual {100} plane. Nanopillars with nt microstructures were simulated as well, and showed that twin boundaries may reduce the serrated flow that often occurs in nanopillars, as well as provide strengthening by promoting the formation of Lomer-Cottrell locks [48]. Studies such as these show the interesting interactions between twin boundaries, grain boundaries, and free surfaces in structures with low dimensionality.

I.3 Nanotwinned metals

Face centered-cubic (fcc) metals with high densities of growth twins are now commonly known as nanotwinned (nt) metals. Several studies during the 1970s of sputtered Cu films might be considered the first investigations of what are now called nt metals [49-50]. These studies looked at the synthesis, structure, and mechanical properties of nt Cu. There was a substantial gap in time between these early studies and the more recent surge in interest of nt metals. This recent surge (from ~2004 to today) can be traced back to a few papers highlighting the mechanical and physical properties of Cu [30, 51] and stainless steels [24, 51]. In those studies, various characterization techniques have revealed a number of desirable properties afforded by the nt structures. Since then, a myriad of studies investigated different properties of nt metals.

I.3.1 Mechanical properties

Perhaps the most recognized aspects of nt metals is their mechanical strength. As previously discussed, nc metals often show very high mechanical strength. Twin boundaries block dislocation transmission with strength comparable to conventional low- and high-angle grain boundaries. Increasing densities of twin boundaries result in enhanced mechanical strength, similar to increasing grain boundary density. However, twin boundaries are highly coherent, and thus lack free volume near grain boundaries.

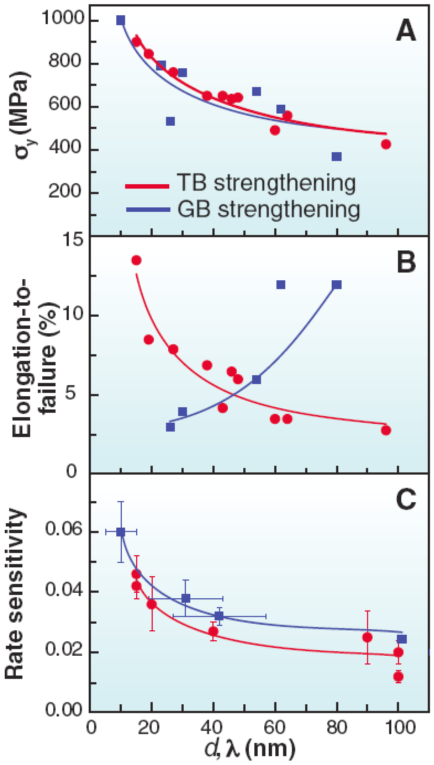

Figure 5: Plots comparing various properties of nc and nt pure Cu as a function of grain size, *d*, or twin thickness, λ. For both nc and nt Cu, trends in yield strength (a) and strain rate sensitivity (c) are similar, while an opposite trend in elongation to failure is shown in (b) [32].

In nt metals the typical twin thickness is on a similar length scale as the average grain boundary spacing in nc metals. As expected, such a fine feature size contributes to high strength in nt metals. Early studies showed high strength via indentation testing [24, 51] and tensile testing in thicker samples [30]. Some interesting mechanical properties of nt metals are shown in Figure 5. Here it is apparent that nt metals show the same high yield strength as nc metals.

Perhaps most interestingly, nt metals have combinations of properties that are not commonly associated with each other, and at times are seemingly paradoxical. For example, (as shown in Figure 5b) nc metals may show decreased ductility with decreasing grain size. This phenomenon is a result of small grain size inhibiting dislocation-mediated plasticity. However, it has been shown that nt Cu may exhibit both high strength and good ductility [32-33]. Figure 6 shows how strength and ductility vary with twin thickness; strength reaches a maximum when average twin thickness is 15 nm, but falls for thinner twins. These properties stem from the highly coherent structure of twin boundaries.

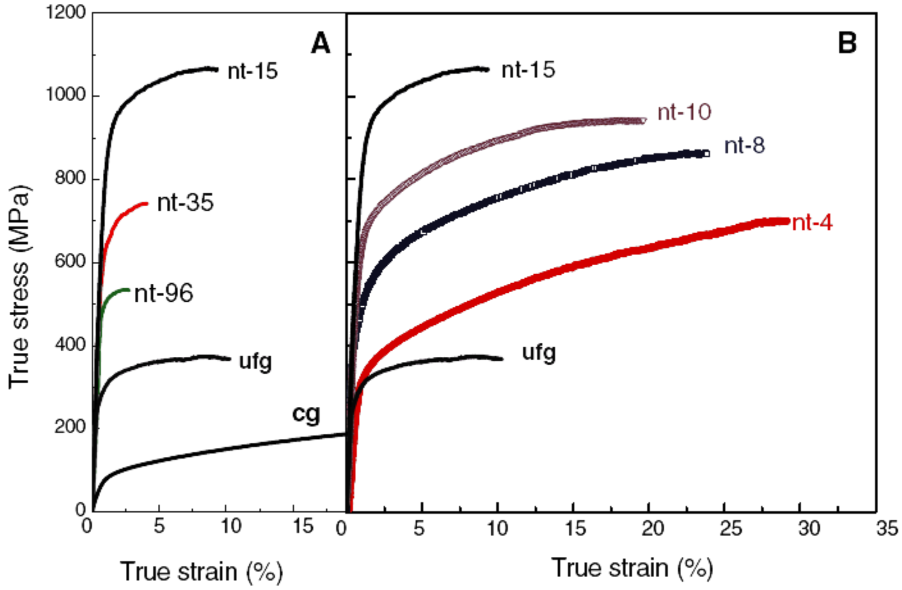

Figure 6: Tensile test stress-strain curves from Cu with ufg and coarse-grained microstructures, as well as nt Cu with average twin thickness varying from 4 to 96 nm. The box on the left shows both increasing strength and ductility with decreasing twin thickness, with a maximum strength achieved at 15 nm. On the right, twin thickness is decreased from 15 to 4 nm. Strength falls, but ductility increases at this length scale [33].

Twin boundaries play a significant role in dislocation blocking and generation, and thus are important to strengthening and work hardening. Furthermore, twin boundaries exhibit other interesting behavior under deformation. Incoherent twin boundaries may change in width depending on the applied stress. ITBs may also migrate under stress. Since thinner twins are easier to move, ITB migration often results in the elimination of thinner twins, leading to decreased twin density.

As previously mentioned, twin boundaries and dislocations undergo reactions during cross slip events, resulting in both the transmission and generation of new of dislocations. Twin boundaries appear to act as sinks for dislocations during high-strain deformation induced via rolling [52]. Other recent observations via *in situ* nanoindentation inside of a

TEM captured interactions between dislocations and CTBs that resulted in the generation of new dislocations and the translation of the twin boundary itself [37]. It was mentioned that ITBs may migrate as a result of stress. Another *in situ* TEM study revealed that transmission of a dislocation across an ITB left a residual dislocation on the ITB that inhibited further ITB migration [36]. These studies shed some light on the mechanisms by which twin boundaries may move and interact with dislocations during deformation, and help to explain the improved elongation to failure observed in nt Cu.

Twins also play a role in enhancing microstructure stability during cyclic deformation. In comparison to coarse grained Cu, nt Cu exhibits a much improved fatigue life, especially for large applied cyclic stresses [53]. Furthermore, the authors of that study note that nt Cu showed less stress-driven grain growth than nc Cu [54]. However, high stress concentrations may cause detwinning in nt Cu, which may eventually lead to crack nucleation [55].

The strain rate sensitivity, m, is a parameter that describes how quickly strain hardening will occur during plastic deformation. It is defined as [56]

$$m = \frac{\partial(\ln \sigma)}{\partial(\ln \dot{\varepsilon})}. \qquad \text{Equation 4}$$

where σ is applied stress and ε is strain. As might be expected from the previous discussion of dislocation generation during cross slip events, nt microstructures influence strain rate sensitivity. Nanoindentation experiments showed that strain rate sensitivity of nt Cu depends on the twin density, and that nt Cu has strain rate of up to 7 times that of nc Cu [57]. This is interesting because in twin-free Cu the rate sensitivity is much lower, and only shows a weak dependence on grain size. This behavior has been linked to dislocation slip transfer processes both by simulations [26], and by experiments testing a range of twin thicknesses and utilizing post-deformation TEM [57-58].

I.3.2 Thermal stability

Metals with nt structures exhibit enhanced thermal stability in comparison to their nc counterparts. Many nc metals show an onset of grain growth below the typical recrystallization temperatures reported for larger grained metals, and rapid grain growth thereafter. This growth results in the removal of high energy boundaries and an overall decreased boundary density decreases the internal energy. In nc Cu the onset of grain growth has been reported at 0.35-0.50 T_m (where T_m is the melting temperature) in nc Cu [59-60], at 0.27 T_m in nc Ni [60], or even at room temperature (0.17-0.25 T_m) in Cu, Pd, and Ag [61]. It is possible to find improved thermal stability in nt metals with similar feature size.

When considering the thermal stability of nt metals, the behavior of both ITBs and CTBs must be taken into account. The migration of ITBs is important to the thermal stability of nt metals. As previously mentioned, ITBs typically have much higher energy than CTBs, hence they will migrate more easily at elevated temperature. In nt Cu heated *in situ* inside of a TEM, ITB migration was observed to remove twin variants [62]. However, in spite of ITB migration, nt metals show improved thermal stability in comparison to nc metals [63]. Since twin boundaries have energies as much as an order of magnitude lower than their high- or low-angle counterparts, CTBs grow more slowly at elevated temperature. Polycrystalline nt Cu films have a lower incidence of ITBs, and instead have other grain boundaries joining adjacent domains [64]. When annealed to over 0.8 T_m, columnar grain boundaries increased in spacing by an order of magnitude (from 50 to 500 nm) while twin thickness only increased from 4 to 16 nm [64]. In nt 330 stainless steel films, grain boundary spacing increases slightly, but twin spacing remained essentially unchanged after annealing to ~0.46 T_m [65]. In both of these cases, nt metals retained small twin thickness during annealing, and strength is better preserved. In nt Cu hardness only fell from ~3.8 to 2.5 GPa despite heating over 0.8 T_m, while in nt 330 SS hardness actually increased as a result of increased compressive stress.

I.3.3 Other interesting properties

The coherent structure of twin boundaries influences more than mechanical properties. In nt Cu films relatively high conductivity is often observed [30, 66-67]. This is in contrast with nc Cu, where resistivity is substantially higher (see Figure 7). Although very fine (7 nm) twins increase resistivity, epitaxial nt Cu films with ~16 nm thickness show conductivity approaching that of bulk oxygen-free high conductivity Cu [67]. This high conductivity stems from less scattering from grain boundaries within the nt films. The combination of low resistivity and high strength that nt metals can provide is exciting, as this combination of properties is ideal for reducing the effects of electromigration.

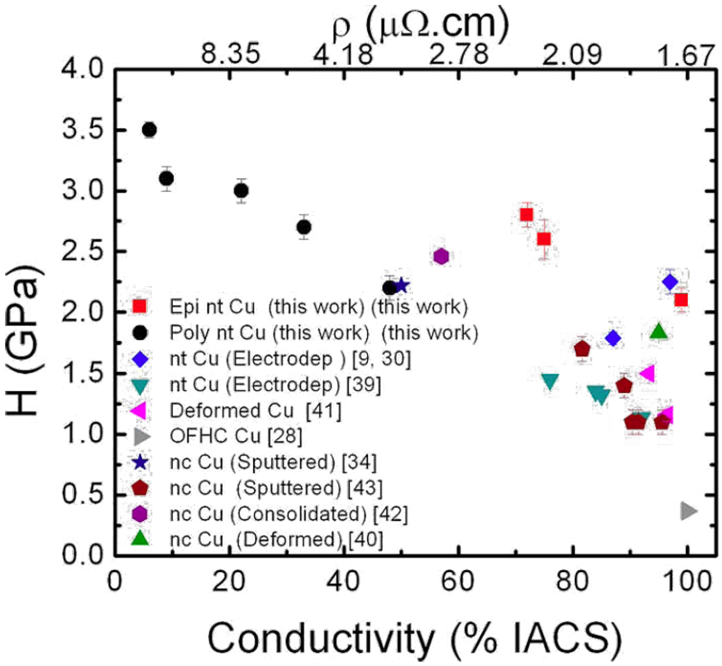

Figure 7: Plot showing hardness as a function of conductivity. Here conductivity is expressed as the percentage of the international annealed Cu standard (IACS), i.e. large grained pure Cu. Both nc and nt Cu show high strength, while a broad range of conductivity is observed. Epitaxial nt Cu arguably shows the best combination of both high strength and high conductivity [66].

Metals with nt structures exhibit varying behavior under ion irradiation. Initial studies of nt Cu irradiated with He ions at room temperature suggested that twin boundaries do not mitigate vacancy or interstitial cluster formation [68]. However, more recent work has revealed that twin boundaries may absorb dislocation loops formed during irradiation. More importantly, twin boundaries were first predicted [69], then observed [70] to eliminate stacking fault tetrahedrons formed during irradiation. These recent observations have prompted increased interest in the radiation tolerance of nt metals subjected to irradiation by different particles, and ongoing studies seek to clarify the details of interactions between twin boundaries and defects produced by irradiation.

I.3.4 Stacking fault energy considerations

Most studied nt metals have low γ_{sf}. As mentioned earlier, low γ_{sf} metals tend to form twin boundaries more easily than those with higher γ_{sf}. For example, Cu and Ag form abundant growth twin boundaries during electrodeposition or vapor deposition techniques. A thermodynamic model derived from nucleation theory predicts that the probability of forming a twinned nucleus depends on many factors, most importantly the γ_{sf} and deposition rate [51]. At low deposition rates, incoming atoms have ample time to diffuse to their ideal lattice sites. Increasing deposition rate results in the formation of more growth defects, as incoming atoms have less time to reach equilibrium lattice sites before more atoms pile on top of them. Hence, high deposition rate is preferable for twin formation. Indeed, higher deposition rate result in enhanced twin formation [32, 51]. Sputtered Cu films show increasing twin density with increasing deposition rate, and by increasing deposition rate it is possible to induce growth twin formation in Ni, a metal with moderately high γ_{sf}. However, for metals with high γ_{sf}, increasing deposition rate is not sufficient to induce growth twin formation.

The tendency of a metal to form twins has been referred to as its *twinning tendency*, *T* [71]. This property is related to the stacking fault energy (γ_{sf}), twin boundary energy (γ_t), and more importantly the ratio of unstable stacking (γ_{us}) to twinning energy (γ_{ut}) [71-73]. Generally these energies correlate to each other, hence fcc metals with low γ_t form twins most readily during nucleation or deformation. *T* is derived by considering the stress conditions at a crack tip leading to nucleation of full dislocations or deformation twin nucleation. It is defined as

$$T = \lambda_{crit}\sqrt{\frac{\gamma_{us}}{\gamma_{ut}}} \qquad \text{Equation 5}$$

where λ_{crit} is a normalized nucleation load dependent on γ_{sf}, γ_{ut}, ν, and several parameters defining the geometry of the crack [71]. It is noteworthy that Equation 5 casts T as a competition between twinning and full dislocation emission. The incidence of twinning increases as cross slip is inhibited in low γ_s metals, not because twinning becomes easier. T explains some seemingly paradoxical behavior, such as why Al rarely twins, while Pd, a metal with similar γ_{sf}, will show deformation twinning. Al and Pd have dissimilar γ_{us}/γ_{ut} ratios, which cause Pd to twin much more easily than Al.

Twinning is so difficult in Al that twins of any kind are rarely observed except in a few noteworthy cases. Molecular dynamics (MD) simulations first predicted deformation twinning in nc Al [39-40]. Deformation twins were produced in nanocrystalline Al in the highly strained areas around an indentation [74], and also at the tip of microcracks during tensile deformation [75]. Deformation twins appeared in fine Al powders subjected to high strain rate deformation via ball milling at liquid nitrogen temperatures [76-77]. Conventional slip of full dislocations was inhibited in these cases by small grain size, high stress concentration, high strain rates, and cryogenic temperatures. Hence, deformation twinning processes occurred to accommodate plastic deformation. The phenomenon of deformation twinning has been well documented by recent reviews [78-79]. It should be noted that these cited cases of twins in Al are all examples of *deformation* twins, not *growth* twins, which are the defining characteristic of nt metals.

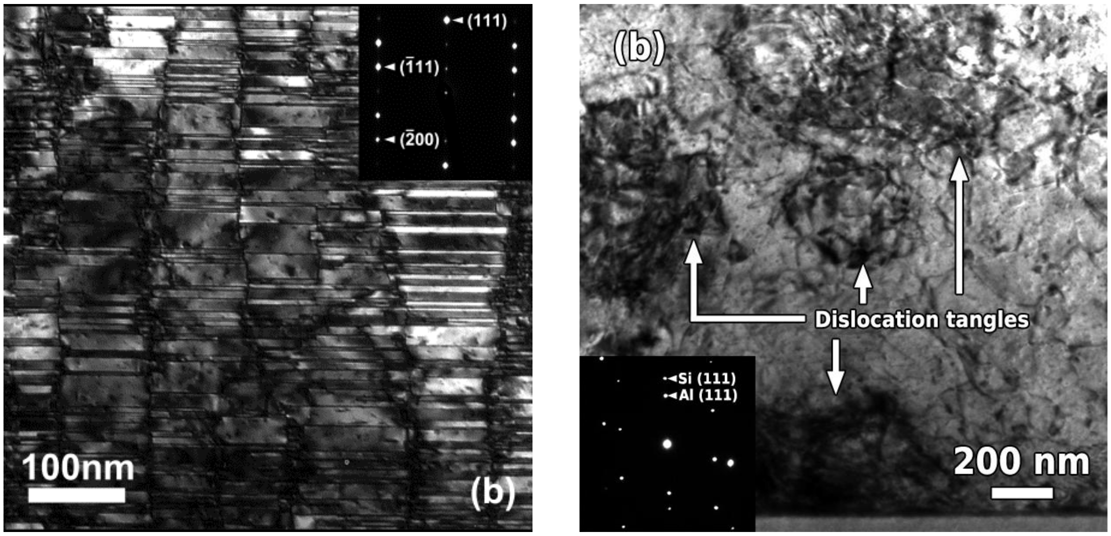

Figure 8: Cross-section view TEM micrographs from similar <110>-type zone axes showing (a) epitaxial Ag and (b) epitaxial Al deposited with similar deposition conditions [80].

Although an occasional small stacking fault or twin may appear in Al, there are no examples in the literature of dense *growth* twins in Al. The difficulty of generating growth twins in high γ_{tb} metals via sputtering techniques is highlighted in Figure 8 above. After room temperature deposition at a relatively high rate, Ag, a low γ_{tb} metal (Figure 8a) shows dense twins. Conversely, Al, a high γ_{tb} metal, deposited under similar conditions (Figure 8b) shows essentially no twins.

One method for overcoming this γ_{tb} barrier is to lower the energy of stacking faults in the metal. In some systems, alloying may lower γ_{sf} [81], sometimes even to the point that the faulted structure is lower energy than non-faulted fcc, e.g. an alloy with fcc structure initially may adopt the hcp structure if enough solute is dissolved. Indeed, stacking fault energy may be tailored by varying the amount and type of solute in a system. In low γ_{sf} alloys of Cu with small portions of Ge, only Shockley partial dislocations are found, and abundant twins and stacking faults appear after deformation by rolling [82]. In alloys of Cu-Zn and Cu-Ge, γ_{sf} decreases with increasing solute content, and a corresponding transition from full dislocation slip and shear band formation to deformation twinning occurs [83]. Interestingly, there have also been studies of nc Cu in which stacking fault energy was varied such that some compositions twinned much more easily than others [84-85]. Here, a combination of grain boundaries and twin boundaries improved both the strength and ductility of the specimens.

It should be noted that lowering γ_{sf} by alloying is a well-known method for increasing the tendency of a metal to twin. However, there are circumstances in which it may be undesirable to resort to alloying. Sometimes the properties of the pure metal might be adversely affected by alloying, e.g. in the case of electrical conductors. As we will see later in this thesis, other methods for inducing twins without varying the γ_{tb} will be attempted.

I.4 Multilayer films

Multilayer films have received attention for various reasons. One feature particularly interesting to the present conversation is the ability to tailor the individual layer thickness, h, and investigate the mechanical behavior of interfaces at varying length scales. At large h multilayer films tend to act as composites, with properties intermediate of the parent components. However, interesting properties develop with decreasing h. The properties of the layer interfaces become more and more important, as the volume affected by the interfaces grows to encompass larger and larger portions of the film. When h is small enough, the layer interfaces may become fully coherent. At this point metastable crystal structures may develop. Some systems with magnetic components exhibit giant magnetoresistance in this regime as well. Additionally, layer interfaces may act as sinks for irradiation-induced defects.

Layer interfaces also may block dislocation transmission, resulting in enhanced mechanical strength. The mechanical behavior of such films has been characterized in numerous systems having coherent or incoherent layer interfaces. Several dislocation-based models have been developed to explain strengthening mechanisms in multilayer films at various length scales, typically characterized by individual layer thickness, h [3, 86-87]. For larger h, dislocation pile-up at layer interfaces dominates deformation behavior, similar to classical grain boundary induced strengthening in polycrystalline metals (i.e. Equation 2). When h reaches tens of nanometers, dislocation pile-up becomes more difficult, and a single dislocation based Orowan bowing mechanism contributes to strengthen [3]. This mechanism is often referred to as confined layer slip (CLS), as dislocations are pinned at the layer interfaces. When h is only several nm, maximum strength is determined by dislocation source length [87], and by numerous factors that influence the interfaces' resistance to dislocation transmission. These factors include Koehler stress [88], coherency stress [89], misfit dislocations [90], stacking fault energy (also called "chemical") mismatch [91], and the ω interaction (slip system continuity across the interface) [89]. At this length scale layer interfaces may become fully coherent, at which point resistance to single dislocation transmission may fall, leading to softening behavior. However, some mechanisms, like the ω interaction and chemical mismatch do not depend on h, and thus contribute to strengthening even at very small h. One example of such strengthening is delayed softening in {111} textured Cu/Ni multilayer films with high-density growth twins as compared to twin-free {100} textured films of identical *h* [92].

I.5 Film deposition techniques

A variety of techniques are available to produce films from metal, ceramic, or polymer species. These include solution-based methods, electrodeposition, and vapor deposition techniques. Vapor techniques encompass two general categories, physical and chemical vapor deposition (PVD and CVD). PVD techniques involve vaporizing the desired species, then condensing it into a solid film. PVD techniques were used in this work, and hence will receive the most attention. CVD techniques differ substantially from PVD techniques in that carrier gasses leave deposited material behind via chemical reactions. No CVD methods were used in this work, so they will not be discussed here, however, the interested reader can find an overview of the topic in books by Freund and Suresh [93] and Ohring [94].

I.5.1 Physical vapor deposition techniques

PVD techniques may use different methods to vaporize the target material. This may be accomplished by thermal means, where the target material is heated enough that a vapor is released, after which it travels across the vacuum chamber to the substrate. Another technique is sputtering, where a plasma is induced near the surface of a target. A strong negative electrical bias is applied to the target, so that ionized atoms from the plasma are accelerated into the target. The violent collision causes ejection of a plume of material, which then travels to the substrate. Variations on this technique include magnetron sputtering, where magnets are arranged behind the target in such a way that the plasma is confined nearer to the target surface, enhancing deposition rate. Inert gasses are typically used for sputtering processes, as the ionized gas atoms will not form compounds with the target material. However, in some cases it may be desirable to introduce a fraction of more reactive gas, whereby the ionized gas atoms to combine with the ejected target atoms. This reactive sputtering technique may be used, for example, to produce aluminum nitride films from an Al target and N_2 gas.

Physical vapor deposition techniques may also be classified by the energy imparted to the film atoms. Thermally evaporated atoms have their energy limited by the evaporation temperature. Hence, they are known as equilibrium techniques. In contrast, sputtered or PLD atoms may have much greater kinetic energy, and are known as non-equilibrium techniques. The atoms' kinetic energy affects their ability to diffuse about the substrate, and plays an important role in determining the film structure.

I.5.2 Film growth and epitaxy

Depending on the interactions between the film and substrate species, film growth may proceed in several different ways. The three basic growth modes include island (Volmer-Weber), layer, (Frank-Van der Merwe) and an intermediate layer/island combination (Stranski-Krastanov) [94]. During island growth, the film atoms bond more strongly to themselves than the substrate, and nucleate in the form of small three-dimensional islands. This situation is analogous to water beading up on a hydrophobic surface like wax. In layer growth, film atoms bond more strongly to the substrate, and consequently nucleate in the form of two-dimensional sheets. This process is analogous to water spreading into a uniform sheet on a metal or glass surface. The combined layer/island growth mode occurs when islands nucleate, then spaces are filled between them, however, the smooth surface is less energetically favorable and more islands form, and the process is repeated.

Kinetic energy of the adatoms may influence the growth mode and structure. As previously mentioned, different deposition techniques impart different kinetic energies to the adatoms. This energy influences diffusion processes after the adatoms arrive at the substrate. Those with lower kinetic energy will migrate less after arriving, and will stop moving more quickly. Higher kinetic energy allows adatoms to diffuse more freely, making it more likely for them to fill in small voids, arrive at equilibrium lattice sites, and in general to create a microstructure with fewer defects.

On a related note, the adatom flux (or alternatively, deposition rate) influences microstructure evolution during growth. A high deposition rate may interfere with diffusion processes at the surface, as incoming atoms may pile up and stop an adatom before it has a chance to stop diffusing on its own. This results in a higher incidence of grown in defects. Lower deposition rates result in fewer grown in defects. It should be noted that in some techniques the deposition rate and power are closely related. For instance, in magnetron sputtering the deposition rate is typically controlled by varying deposition power, which also affects the kinetic energy of the adatoms. Hence, methods such as shadowing the gun or pulsing it on and off may be employed in an effort to achieve high kinetic energy but a low deposition rate.

Depending on adatom/substrate interactions, films may be polycrystalline, where the individual grains are oriented randomly with respect to the substrate, or epitaxial, where the film adopts the structure of the substrate. Epitaxial growth requires a reasonably close surface energy mismatch between the substrate and film species to promote wetting, but more importantly it requires a good size and geometric match between the two species. A perfect epitaxial scenario is growing a material on itself (homoepitaxy), as the lattice parameters and surface energy of the atoms is identical, and practically any geometry can be recreated. This is done in the semiconductor industry for manufacturing of some devices, however for research purposes it is often more useful to use dissimilar substrate and film species (heteroepitaxy). In the simplest case, one would again choose substrate and film species with identical lattice spacing, structure, and surface energy. However, this is often not possible, so it may be more convenient to try to match the substrate and film via a rotational relationship, or by domain matching epitaxy [95]. By exploiting these aspects of epitaxy, it is possible to grow many different epitaxial films with numerous orientations.

A full discussion of all aspects of film deposition parameters and their influence on microstructure is beyond the scope of this thesis. Excellent books by Freund and Suresh [93] and Ohring [94] provide thorough overviews of the subject. The factors most relevant to this work have been briefly discussed above, and are as follows:

- Adatom energy
- Adatom flux (deposition rate)
- Choice of substrate
- Temperature of substrate

In this work, depositions were performed with sputtering parameters such that adatoms had high kinetic energy and high deposition rate, and substrates that allowed both polycrystalline and epitaxial structures were used. Depositions were performed at room temperature, such that many defects in the form of twin boundaries and stacking faults were incorporated into the films.

I.6 Scope and goals

The scope of this thesis includes several aspects related to growth twin formation, and the resulting effects on the mechanical properties of films. We first consider the synthesis of epitaxial nt Ag films with different orientations. Previous studies of nt metals mainly focused on Cu, so the synthesis of nt Ag yields another system for comparative study. Epitaxial nt Ag films grown on differently oriented Si substrates have different textures and twin densities. These microstructure differences result in dramatically different nanoindentation hardness, as well as markedly different behavior during annealing. Additionally, the range of twin and domain boundary spacing produced by annealing allow for a better understanding of the mechanical strengthening induced by said boundaries.

Also, nt Al films are synthesized for the first time. Al has high γ_{sf}, and twins of any kind in Al are very rare. This γ_{sf} barrier is overcome by the use of Ag template layers. As mentioned previously, the Ag layers readily form twins. Because of a small lattice mismatch, Al and Ag may grow epitaxially on each other, resulting in the replication of defects from layer to layer. The process involved in growing the nt Al films is interesting in itself, and since it has never been synthesized before, we have the opportunity to be the first to test various properties of the films. Furthermore, this newly synthesized nt Al allows us to test hypotheses that previously were only testable by computational means. Finally, if nt Al were exhibit properties similar to other nt metals, it would have practical importance. Al films are employed in numerous applications, such as movable parts for MEMS devices [96], as a metallization material for integrated circuits and flat panel LCD monitors [97-98], as an optical reflector and in digital micromirror devices [99-100]. Therefore, Al with high strength from high-density twins is highly desired.

CHAPTER II

EXPERIMENTAL DETAILS

II.1 Magnetron sputtering

Depositions were performed using the magnetron sputtering system operated by the Zhang Film and Nanolayer Group at Texas A&M University. This is a custom-built sputtering system with four 3” sputtering guns (Kurt J. Lesker, Inc., Livermore, CA), and several DC and RF power supplies. Pumped by both turbomolecular and cryopumps, the chamber reached typical base pressures of ~ 5 to 9×10^{-8} torr prior to deposition. Ar gas was used for sputtering, and deposition pressures of ~3×10^{-3} torr were typically observed during deposition. Single-crystal silicon wafers with various orientations were used as substrates throughout this work. Some substrates were etched using HF prior to deposition in order to remove the native oxide layer in order to achieve epitaxial growth, while others were not etched to preserve the amorphous SiO_2 surface structure. Deposition rates were manipulated by controlling deposition power. Deposition power varied from approximately 50 to 400 W, which translates to a power density on the target of ~1- 9 W/cm^2. Deposition rates of up to ~25 Å/s were achieved for Ag depositions, while rates of ~10 Å/s were observed in Al.

II.2 X-ray diffraction

X-ray diffraction (XRD) is commonly employed to examine film quality. In this technique, a beam of x-rays is directed onto a sample, and it is diffracted by coherently ordered lattice planes as is passes through. Figure 9 illustrates the general geometry of the incident beam and atomic planes.

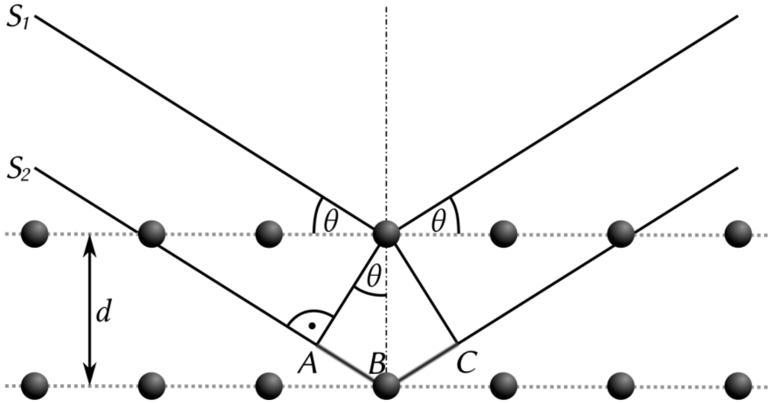

Figure 9: XRD schematic. The beam, represented by lines S_1 and S_2 is at an angle of incidence, θ, with the atomic planes of the sample. Those planes are separated by an interplanar spacing, d [101].

The beam is only diffracted when the following condition is met

$$n\lambda = 2d\sin\theta \qquad \text{Equation 6}$$

where n is an integer determined by the order of the observed peak, λ is the wavelength of the incident x-ray beam, and θ is the angle between the incident beam and atomic planes from which diffraction is occurring [102]. The interplanar spacing, d, is determined for a cubic system by

$$d = \frac{a}{\sqrt{h^2 + k^2 + l^2}} \qquad \text{Equation 7}$$

where *a* is the lattice parameter, and (hkl) correspond to the Miller indices of the lattice plane of interest. The Bragg equation (Equation 6) identifies by their spacing, allowing one to determine the crystallographic orientation of a sample.

Conventional 2θ scans were collected using a either a Bruker (Billerica, MA) AXS D8 Bragg-Brentano X-ray Diffractometer (located in the X-ray Diffraction Laboratory, Department of Chemistry, Texas A&M University) or PANalytical (Almelo, Netherlands) X'Pert PRO Materials Research Diffractometer (located at CINT, Los Alamos National Laboratory, Los Alamos, NM). Phi scans were performed using the PANalytical diffractometer. Both were operated using Cu Kα radiation (λ = 1.5418 Å).

II.3 Transmission electron microscopy

Transmission electron microscopy (TEM) is a microscopy technique in which an electron beam is passed through a specimen, and scattered by the atoms present. Depending on how the incident electrons are scattered or absorbed, the transmitted beam changes and reflects the microstructure. A schematic of the microscope components appears below in Figure 10.

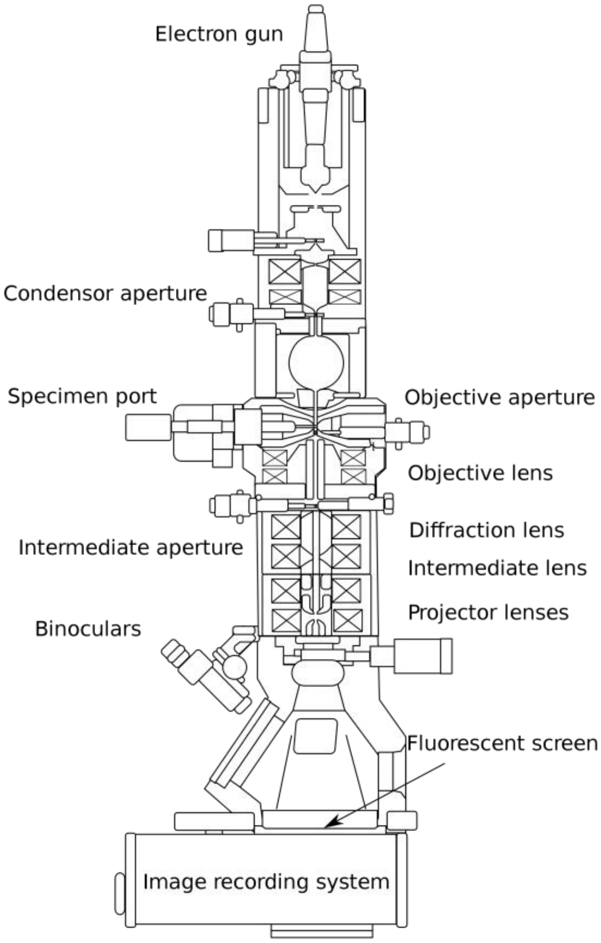

Figure 10: Electron microscope schematic showing a cross section view of the essential parts of the microscope. The microscope functions similarly to a slide projector. The electron beam is emitted from the electron gun at the top. The beam is shaped by apertures and electromagnetic lenses before reaching the specimen. After being deflected by interactions with the specimen, more lenses to magnify the beam, and the image is viewed on the screen or by the camera system [103].

The resolving power of a microscope (light or electron) is limited by the wavelength of the incident particles. In the case of visible light microscopes, the wavelength is on the order of hundreds of nm. In the case of TEM, electrons may be accelerated to hundreds of kV. This high energy imparts a de Broglie wavelength of a particle given by

$$\lambda = \frac{h}{m_0 v}\sqrt{1-\frac{v^2}{c^2}} \qquad \text{Equation 8}$$

where λ is wavelength, h is Planck's constant, m_0 is the rest mass of the electron, v is the electron's velocity, and c is the speed of light. Discounting relativistic effects, a useful approximation to Equation 8 is

$$\lambda = \frac{h}{mv} \approx \frac{1.23}{\sqrt{V}}\,. \qquad \text{Equation 9}$$

In the rightmost term, V is the accelerating voltage of the microscope. This approximation gives the wavelength in nm for a given accelerating voltage. For a 200kV microscope, as is commonly used in materials research, the wavelength is 0.00275 nm = 2.75 pm. The ultimate resolving power of the microscope is also limited by other factors, namely accumulated aberrations caused by the electron source and lenses, however, electron microscopes typically have much better resolving power than light microscopes. Accordingly, many commonly available TEMs can resolve features down to at least a few Å, while more advanced microscopes possess sub-angstrom resolution.

Bright field (BF) imaging is the most common imaging technique. Here the transmitted beam illuminates areas on the image and contrast is generated by discarding the scattered electrons. Dark field (DF) imaging is essentially an inverse of bright field imaging; illumination is provided by specifically choosing diffracted electrons to form the image, and other electrons are discarded. Selected area electron diffraction (SAD) may also be performed to obtain structural information.

Additionally, numerous analytical techniques can be performed by manipulating the beam and using different instruments for information collection. By rastering the beam across a sample and collecting only the scattered electrons (a technique called high angle annular dark field scanning TEM, or HAADF-STEM) compositional information can be collected. Electron energy loss spectroscopy (EELS) detectors use magnetic fields to sort electrons based on their voltage. Since electrons have a constant charge, their voltage is the energy. Interactions with different atomic species in the sample will result in different electron voltage, hence the EELS system sorts the electrons and gives information about the local composition of the sample.

Specialized holders may further enhance the TEM by providing the capability to alter the specimen or its environment during imaging. Studies using heating holders have allowed researchers to observe ITB migration in nt Cu films [62]. Tensile straining holders have been used to study dislocation nucleation in single crystal Al specimens [104], to create 3-dimensional reconstructions of dislocation/grain boundary interactions [105], and also to investigate interactions between single dislocations and twin boundaries [34]. Indentation holders have recently been used to investigate the mechanical properties irradiated Cu [106], as well as dislocation/twin boundary interactions in nt Cu [36-38]. This brief introductory section covers only the very basics of TEM theory and techniques. The reader is referred to an excellent textbook by Williams and Carter [107] for a detailed discussion of TEM operation and capabilities.

TEM imaging and analysis was performed using several microscopes through the course of this work. Most BF and DF imaging was performed on a Jeol (Tokyo, Japan) JEM-2010 or FEI (Hillsboro, OR) Tecnai G2 F20-ST microscopes, both operated at 200kV. High resolution imaging was performed on a Jeol 3000F microscope. High-angle annular dark field scanning transmission electron microscopy (HAADF-STEM) was performed using the Tecnai G2 F20-ST, as well as the TEAM 0.5 microscope, an FEI Titan electron microscope enhanced by an advanced STEM corrector, operated at 300kV. This microscope is noteworthy, as it is among the most advanced microscopes currently available. In STEM mode it is capable of resolving features at 0.5 Å resolution, giving local chemical composition of columns of atoms in a sample.

II.4 Nanoindentation

Indentation methods have been employed for decades for nondestructive testing of material properties. The general relationship for hardness is

$$H = P / A_r \qquad \text{Equation 10}$$

where H is hardness, P is load, and A_r is residual contact area, which is itself a function of the indenter tip shape and plastic response of the material. Historically, A_r was determined by applying a to the sample load through an indenter tip of known geometry, then measuring the size of the residual indent via microscopy. The area could then be computed by assuming the indent retained a shape similar to the indenter tip geometry. The size and shape of an indent is dependent on the load, indenter shape, and elastic and plastic response of the sample. The geometry of an indent is shown schematically below in Figure 11:

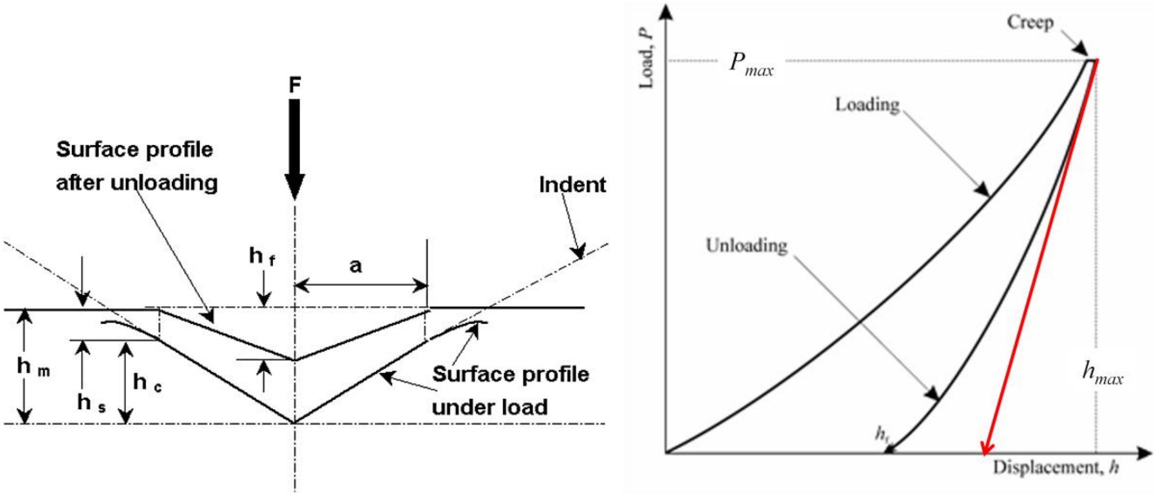

Figure 11: Contact area and loading/unloading curve schematics [108-109].

Here, h_m is the maximum displacement, h_c is the contact depth, and h_f is the final depth. One can see that there is some elastic recovery of the sample after loading. Traditional indentation methods pose some problems for materials with low dimensionality, such as films. Of primary concern is the load. Common loads used for bulk materials may penetrate straight through a film.

Nanoindentation methods utilizing the Oliver-Pharr method are most common. For this method a load is applied to the sample, then removed. During this process the force and position information from the indenter is recorded. From the force-displacement curve, the unloading stiffness,

$$S = \left\lfloor \frac{dP}{dh} \right\rfloor, \qquad \text{Equation 11}$$

can be determined. This value reflects the response from both the tested material and indenter tip. From the unloading stiffness the reduced modulus,

$$E_r = \frac{\sqrt{\pi}}{2}\frac{S}{\sqrt{A_p(h_c)}}, \qquad \text{Equation 12}$$

can be determined. E_r is related to the material parameters of the tested material and indenter by the following relation;

$$\frac{1}{E_r} = \frac{1-\nu_m{}^2}{E_m} + \frac{1-\nu_i^2}{E_i}, \qquad \text{Equation 13}$$

where the subscripts *m* and *i* refer to the tested material and indenter, respectively. By simple algebra, the Young's modulus of the tested material can be determined:

$$E_m = \frac{1-\nu^2}{\frac{1}{E_r} + \frac{\nu_i^2 - 1}{E_i}}. \qquad \text{Equation 14}$$

In order to determine the indentation hardness of the sample, the projected area at the given contact depth must be determined. This relationship is dependent upon the geometry of the indenter tip, and can be approximated by

$$A_p(h_c) = C_0 h_c^2 + C_1 h_c^1 + C_2 h_c^{1/2} + C_3 h_c^{1/4} + ... \qquad \text{Equation 15}$$

For a Berkovich indenter, the first constant, C_0, is 24.5, while for a cube corner (i.e. Vickers) indenter tip it is 2.598. Thus, a common approximation for the area function for a Berkovich indenter is

$$A_p(h_c) \approx 24.5 h_c^2. \qquad \text{Equation 16}$$

Contact depth can be estimated from the measured displacement, load, and calculated stiffness by the relation

$$h_c = h_{\max} - \varepsilon \frac{P_{\max}}{S}, \qquad \text{Equation 17}$$

where ε is a geometrical constant (0.75 for a Berkovich indenter). Finally, nanoindentation hardness, H_{IT}, can be determined by

$$H_{IT} = \frac{P_{\max}}{A(h_{c,\max})} \qquad \text{Equation 18}$$

where $h_{c,max}$ is the calculated maximum contact depth. Note that H_{IT} is essentially equivalent to the H determined by Equation 10, with the exception that the load was measured continuously, and the projected area is computed as a function of contact depth. Depending on the elastic and plastic response of the material, the size and shape of indentations may be investigated via optical, SEM, or AFM. The actual residual indentation geometry may be investigated. Other interesting aspects of the indent (such as pileup of material at the edges) may also be observed.

For the study of films, nanoindentation methods are essential tools, as often other methods (e.g. tensile tests) are problematic to perform due to the difficulty of removing a thin foil from a substrate without damaging it. Furthermore, tensile tests of relatively thin foils often show rapid onset of shear localization, which may cloud the usefulness of such results. The increasing availability of FIBs, and the development of novel machining and *in situ* testing methods have somewhat addressed these issues, but such methods were unavailable for this work. Hence, nanoindentation results are still very important.

Film hardness was determined by instrumented nanoindentation experiments, performed using a Fischerscope (Fischer Technology, Sofia, Bulgaria) HM2000XYp indenter with a Vickers indenter tip. This indenter was operated using the Oliver-Pharr method. Typically, at least 9 good indentations were performed for each sample to ensure reliability of the data.

CHAPTER III

SYNTHESIS AND MECHANICAL PROPERTIES OF NANOTWINNED SILVER FILMS[*]

III.1 Overview

Epitaxial silver films with (111) and (110) orientations were deposited by magnetron sputtering onto silicon (111) and (110) substrates, respectively. High-density growth twins with an average spacing of a few nanometers are observed in the (111) oriented films, with twin boundaries oriented normal to the growth direction. Twins are observed in the (110) oriented films with a much lower twin density, and the twin boundaries are oriented 60° from the growth direction. The epitaxial nanotwinned Ag (111) and (110) films have respective indentation hardness values of ~ 2 and ~ 1 GPa. The influences of deposition parameters, stacking fault energy, and orientation of {111} planes on the formation of nanotwins are discussed.

---

[*] This chapter reprinted with permission from "High Strength, Epitaxial Nanotwinned Ag Films" by D. Bufford, H. Wang, and X. Zhang, 2011. *Acta Materialia*, Volume 59, pp 93–101, Copyright 2011 by Elsevier.

III.2 Introduction

Nanotwinned (nt) structures have been reported in face-centered-cubic (fcc) metals, and these highly twinned structures lead to unique electrical [66-67, 110], thermal [62, 64-65] and mechanical properties [24, 30, 32-33, 51, 64-66, 111]. In comparison to high angle grain boundaries in nanocrystalline metals, coherent Σ 3 {111} twin boundaries in nt metals have much lower energy, and hence nanotwins are much more stable at higher temperatures. The average twin spacing in sputtered nt Cu only increases from 4 to 16 nm after annealing at $0.8T_{melt}$, while grain size increases by an order of magnitude [64]. Meanwhile the electron scattering coefficient of coherent twin boundaries (CTBs) is measured to be an order of magnitude lower than that of high angle grain boundaries [66]. The most extensively studied aspects of nt metals are their mechanical properties. Nanotwins induce a substantial increase in mechanical strength. Experimental observations and molecular dynamics (MD) simulations [24-28, 46, 48, 112-113] have shown that twin boundaries act as strong barriers to the transmission of dislocations, leading to increased mechanical strength. A recent study has shown that a negative Hall-Petch relation, occasionally observed in nanocrystalline metals, may also exist in electrodeposited nt Cu [33]. A similar phenomenon has been observed in large scale MD simulations [44]. Besides high strength, certain nt metals also possess significant ductility as revealed by large strain in tension and under rolling [30, 32-33, 111]. High densities of trapped dislocations are observed at twin boundaries after deformation [114], and the density of mobile dislocations appears greater in nt metals with smaller twin spacing. Our recent studies have shown that twin boundaries can be mobile under stress; detwinning phenomena in sputtered nt Cu have been examined *in situ* inside a transmission electron microscope (TEM), and detwinning mechanisms were further revealed by MD simulations [75, 115]. The detwinning mechanisms can explain the annihilation of very fine twins (1-2 nm spacing) in rolled polycrystalline nanotwinned Cu [52], and also account for the "softening" (negative Hall-Petch relation) observed in electrodeposited nt Cu.

The formation of twin boundaries and stacking faults during growth of sputtered nt metal is a less well understood subject. Our thermodynamic model has predicted that twin formation depends strongly on the deposition rate and twin boundary energy (or stacking fault energy, as it tends to correlate with twin boundary energy) [51, 116]. Another intriguing phenomenon is the orientation of growth twins. In sputter-deposited polycrystalline Cu and 330 stainless steel films, twin boundaries are oriented predominantly perpendicular to the growth direction [24, 111], whereas twin boundaries are often randomly oriented in thick films fabricated by pulsed electrodeposition [110].

In comparison to nt Cu, twins in Ag have received little attention. Silver has the lowest twin boundary energy among all the elemental fcc metals, and hence it might form even higher densities of twins than Cu during sputtering. Although some cross-sectional TEM work has previously been completed on epitaxial Ag films, the goal of the study was to examine the Ag-Si interface [117]. Hence, the formation of growth twins in Ag films and their effects on mechanical strength have not yet been studied. It is of interest to compare twin-induced hardening in nt Ag films with compiled mechanical property data from various types of Ag structures, including single crystals [118], bulk nanocrystals [119], and polycrystalline Ag films with fewer twins [120-121]. Furthermore, Ag has the highest room-temperature electrical conductivity and thermal conductivity among all elemental metals, but it is very soft, and hence its use in microelectronics applications is limited. These attributes make Ag an attractive model system for the study of twin boundary formation and twin-induced strengthening mechanisms, and these studies could have direct effects on the application of Ag in electronics industry.

In this paper we demonstrate that high density nanotwins can be formed in epitaxial Ag films on both Si (111) and Si (110) substrates, and we examine the possible formation mechanisms of nanotwins. By controlling the Ag epitaxial orientation, it is possible to control the orientation and density of growth twins, and consequently affect the film strength significantly.

III.3 Experimental

Ag films ~ 2 μm in thickness were deposited by magnetron sputtering onto HF etched single crystal silicon (111) and (110) substrates. The deposition chamber was evacuated to a base pressure of approximately 8.0×10^{-8} Torr, and Argon pressure during deposition was ~2 mTorr. X-ray diffraction (Bruker-AXS D8 Bragg-Brentano X-ray Diffractometer, Cu Kα radiation) was used to analyze the texture in the deposited films. Cross-section and plane-view specimens for TEM studies were prepared by mechanical grinding and polishing followed by low energy ion milling. These specimens were analyzed by a JEOL 2010 transmission electron microscope with 200kV accelerating voltage. High resolution TEM (HRTEM) imaging was performed with a JEOL 3000F microscope operated at 300 kV. Film hardness was determined by instrumented nanoindentation experiments, performed by a Fischerscope HM2000XYp indenter with a Vickers indenter tip.

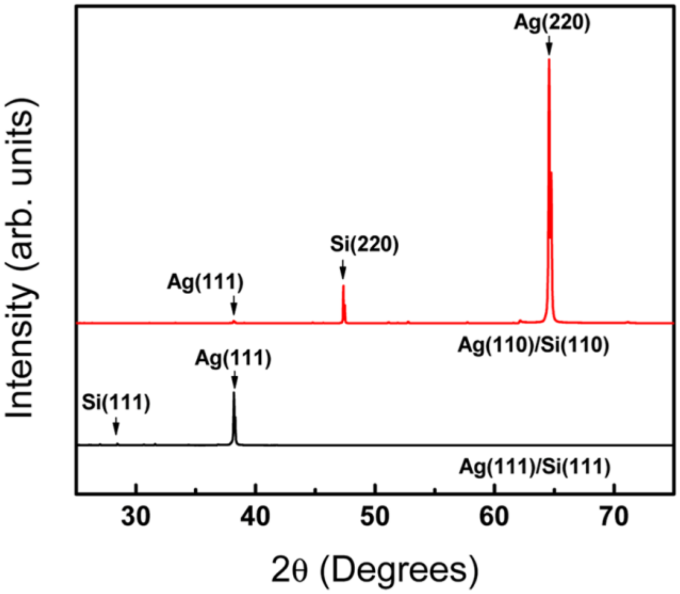

Figure 12: XRD spectra: The absence of other peaks in the XRD spectrum for the Ag (111) film on the Si (111) substrate suggests the formation of an epitaxial film. A highly textured Ag (110) film forms on Si (110) substrate with orders of magnitude lower Ag (111) diffraction peak.

III.4 Results

The normal θ~2θ XRD scans for the Ag films grown on Si (111) and (110) substrates are plotted in Figure 12. The absence of all other Ag peaks in the XRD spectrum of the Ag film on Si (111) suggests the formation of a highly textured Ag film along the (111) orientation. The XRD spectrum for the Ag film on Si (110) shows a primary Ag (220) peak with very weak (111) and (200) Ag peaks, which suggest that the film is predominantly textured in the Ag (220) orientation.

Plan-view TEM micrographs of the Ag (111) films (Figure 13a) show numerous nearly hexagonal domains. The boundaries between domains appear less well-defined than those for a typical polycrystalline grain structure. The SAD pattern (Figure 13a, inset), collected with a large aperture to include numerous domains, shows a structure characteristic of a single crystal viewed along a [111] zone axis. Cross-section TEM specimens of the Ag (111) films were examined along orthogonal $[01\bar{1}]$ and $[2\bar{1}\bar{1}]$ zone axes to reveal the microstructure and epitaxial relationships between the film and the substrate.

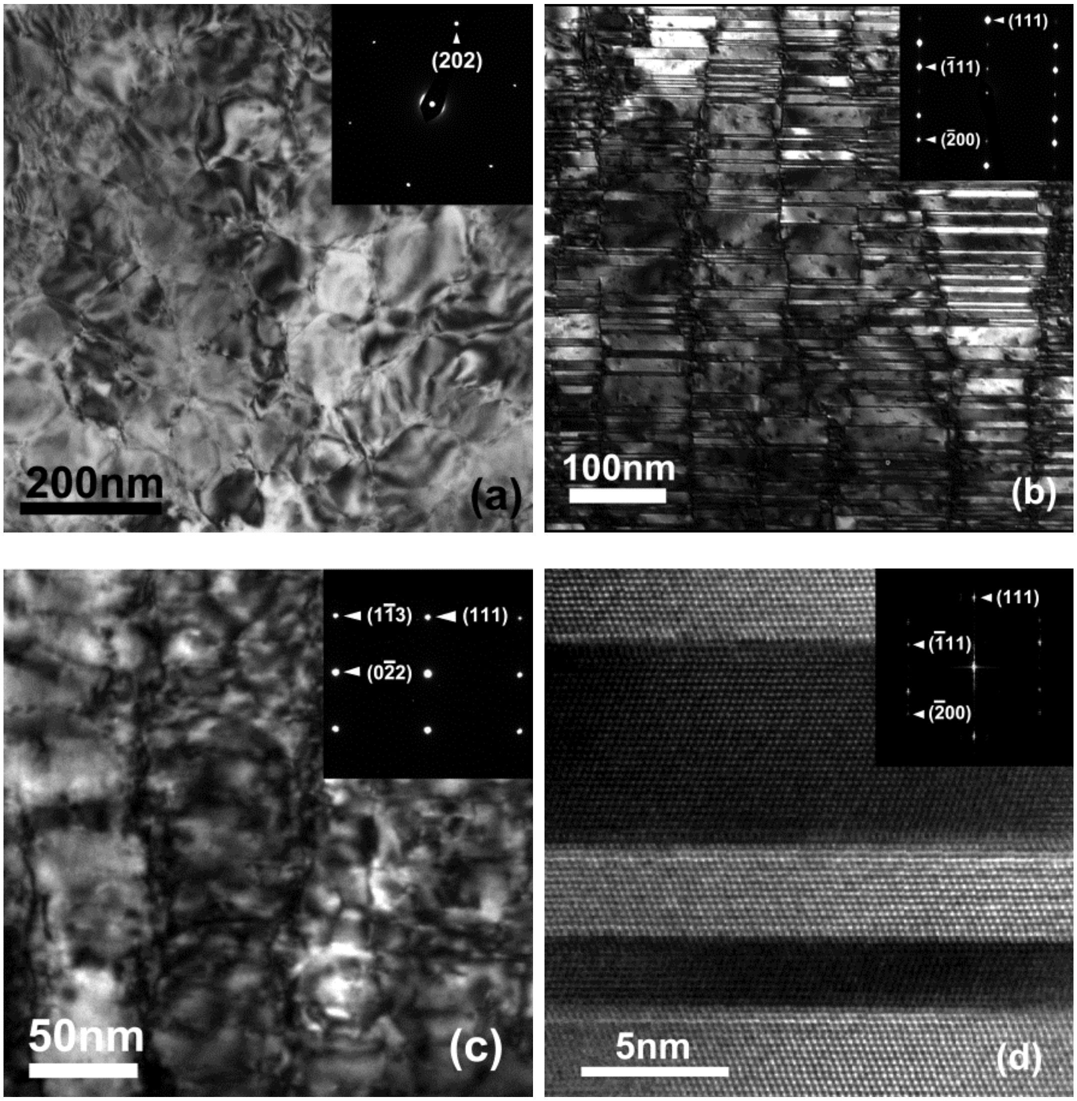

Figure 13: (a) Plane-view TEM micrograph from the Ag (111) film on the Si (111) substrate showing numerous nearly hexagonal domains with an average size of ~120 nm. The inset SAD pattern clearly shows single crystal like diffraction along the Ag [111] zone axis. (b) Cross-section view from the $[\mathbf{01\bar{1}}]$ zone axis reveals high density growth twins with twin boundaries normal to the growth direction. (c) Cross-section view examined from the $[\mathbf{2\bar{1}\bar{1}}]$ zone axis shows no sign of twins. (d) HRTEM micrograph and the inset FFT show the formation of coherent $\Sigma 3$ {111} twin boundaries.

When viewed from the $[01\bar{1}]$ zone axis (Figure 13b), both the columnar domain structure and twin boundaries are easily discerned. The twin boundaries appear every few nanometers oriented normal to the growth direction, and are so closely spaced that it is impractical to differentiate between the matrix and twins. The SAD pattern (Figure 13b, inset) shows clear evidence of (111) twins, as well as a single-crystal-like pattern with distinguished diffraction dots. When examined from the orthogonal $[2\bar{1}\bar{1}]$ zone axis (Figure 13c), columnar domain boundaries are still visible. However, the twin boundaries are invisible, as this direction does not look edge-on at the twin boundaries. When examining the twin boundary by HRTEM along the $[01\bar{1}]$ zone axis, the zigzag structure of adjacent twin variants is apparent (Figure 13d). The inset fast Fourier transform (FFT) in the micrograph confirms the presence of Σ3 {111} coherent twin boundaries.

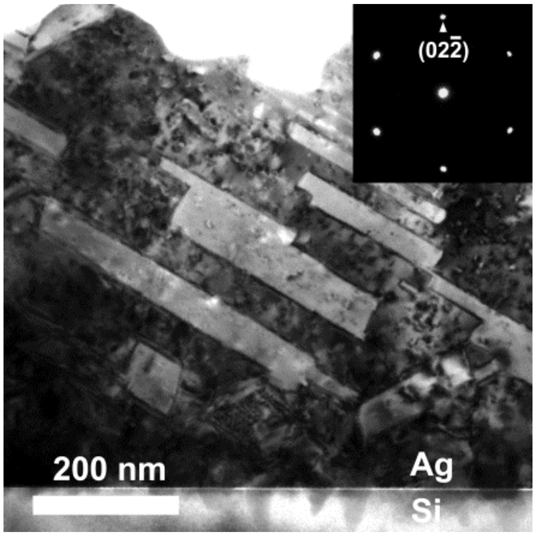

Figure 14: Cross-section view TEM micrographs collected from the [111] zone axis of the Ag (110) film on the Si (110) substrate reveal an interesting structure. Twin boundaries appear tilted ~ 60° from the growth direction when examined along this orientation. The single crystal-like epitaxial character of the film is evident in the SAD pattern (inset).

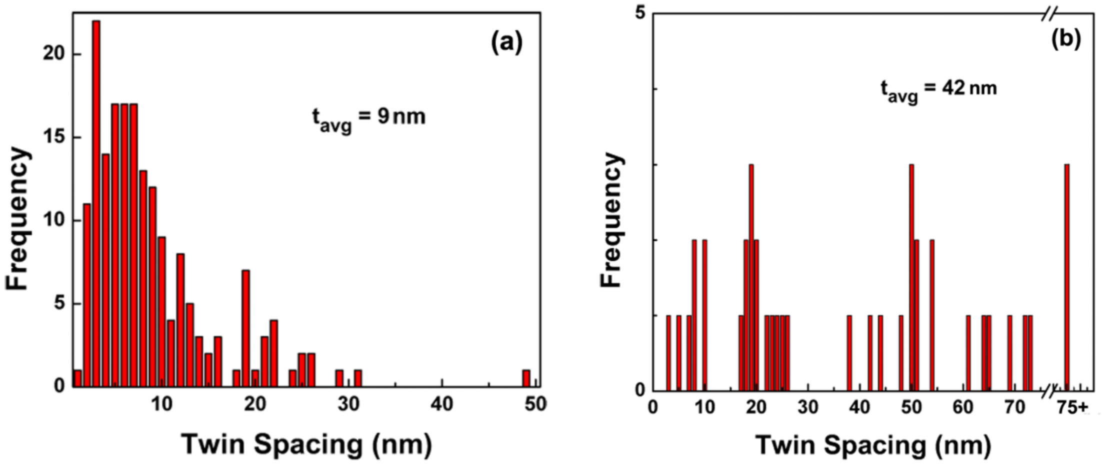

Figure 15: The average twin spacing in the (a) Ag (111) film is below 10 nm, and in the (b) Ag (110) film it is ~ 42 nm.

The film deposited on the Si (110) substrate, when examined from the [111] zone axis, shows a different microstructure from the Ag (111) film. It shows a much lower density of twin boundaries, and the twins are oriented 60° from the growth direction (Figure 14). The average twin spacing in Ag (111) film is ~ 9 nm, as shown in Figure 4a, whereas the average columnar domain size (not shown here) is ~ 120 nm. The average twin spacing in the Ag (110) films is ~ 42 nm as shown in Figure 15b. Plan-view TEM examination of the Ag (110) film reveals only large domains with many thickness contours and few grain boundaries, indicating that the average domain size is on the order of a few microns.

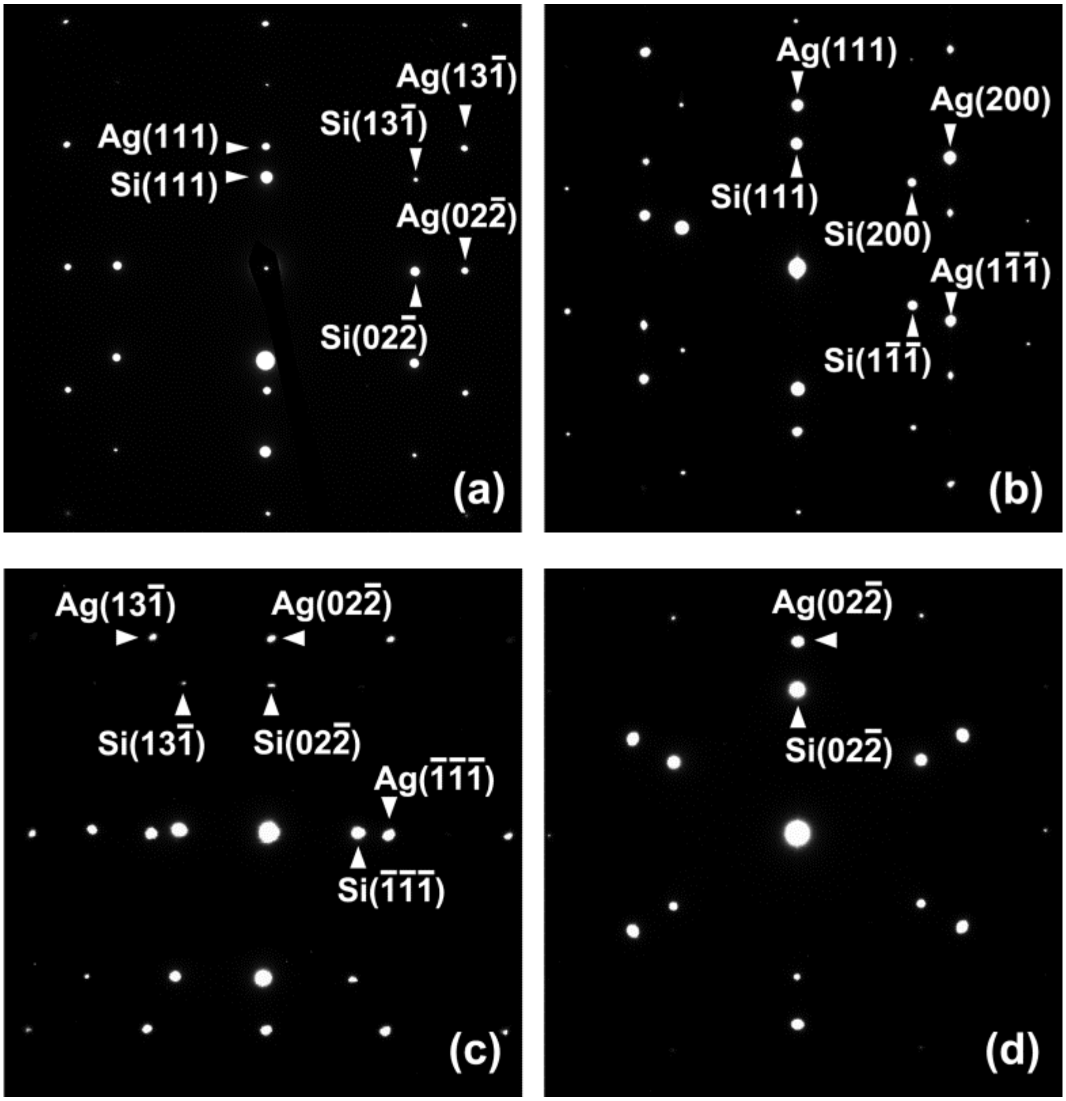

Figure 16: SAD patterns collected at the Ag-Si interface reveal the orientation relation between the substrates and films. The patterns from (a) and (c) the $[2\bar{1}\bar{1}]$ zone axis in Ag (111) and Ag (110) films, (b) the orthogonal $[01\bar{1}]$ zone axis in Ag (111), and (d) the orthogonal [111] zone axis in the Ag (110) films, reveal that identical indices in the film and substrate are parallel to each other.

The cross-section SAD patterns in Figure 16a-d show the in-plane epitaxial orientation relation between the Ag films and Si substrates. For the Ag (111) film it is evident that Ag <112> // Si <112> and Ag <110> // Si <110>, while for the Ag (110) film, the orientation relationships are Ag <112> // Si <112> and Ag <111> // Si <111>; zone axes of identical indices are parallel to each other within the film plane, and also along the growth direction. The substrate-film orientation relationships are summarized schematically in Figure 17a,b. In epitaxial Ag (111) films there are two twin variants: Ag(111)//Si(111) with Ag[$0\bar{1}1$]//Si[$0\bar{1}1$], and Ag(111)//Si(111) with Ag[$01\bar{1}$]//Si[$01\bar{1}$] [122-123]. These variants correspond to a 180° rotation about the [111] axis.

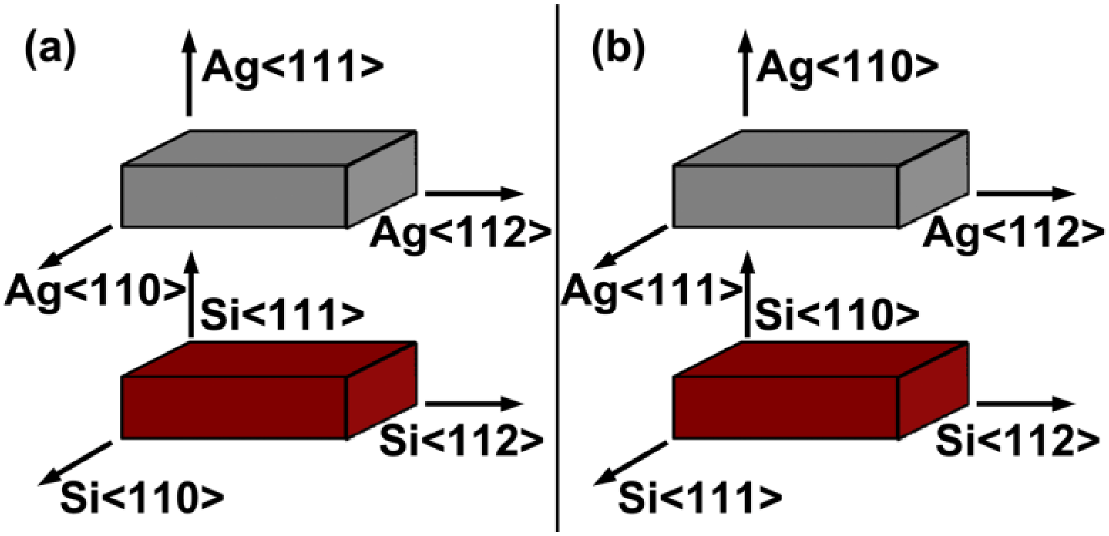

Figure 17: Film-substrate orientation relation schematics for (a) Ag (111) / Si (111) and (b) Ag (110) / Si (110). The films were examined by TEM along the in-plane zone axes illustrated here.

A hardness versus indentation depth profile was compiled for indentation depths of 100-300 nm. Maximum indentation depth was limited to 15% of the total film thickness to avoid substrate effects, and at least nine indents were performed at each indentation depth to determine the average hardness and standard deviations. A plateau of hardness vs. indentation depth is achieved, as shown in Figure 18. At an indentation depth of 300 nm the

Ag (111) and Ag (110) films show respective indentation hardness values of ~ 2 ± 0.04 and ~1 ± 0.04 GPa.

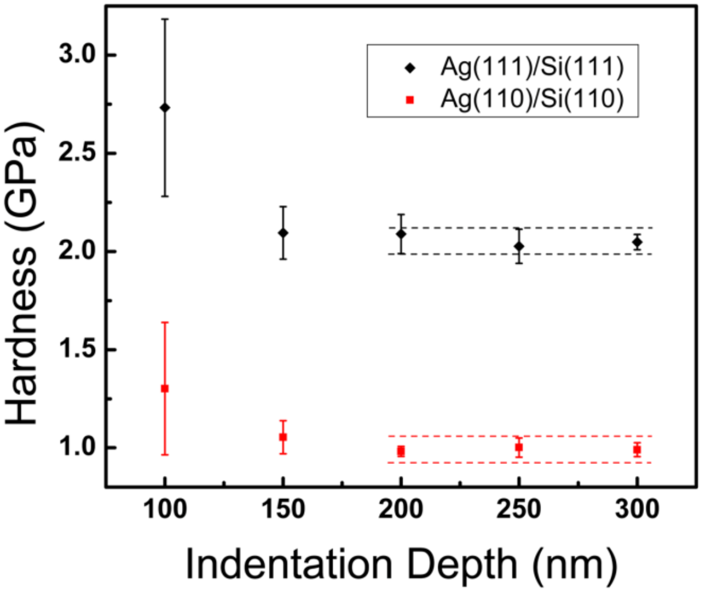

Figure 18: Indentation hardness is plotted as a function of indentation depth. The Ag (111) films show significantly greater indentation hardness than the Ag (110) films. The error decreases with increasing depth, and hardness typically reaches a plateau by ~ 200 nm.

III.5 Discussion

III.5.1 Epitaxial growth via domain matching epitaxy

A 2-micron thick Ag film was calculated to absorb over 95% of the x-ray beam as it passes through to the substrate and then reflects back out of the film. Thus, the single crystal Si (111) and (220) substrate peaks are weak in comparison to the corresponding peaks in Ag. The XRD spectrum for the Ag (110) film shows that a small fraction of (111) and (100) oriented domains are present within the film, but the majority of the film has (110) orientation. The single-crystal like SAD patterns from the plane-view Ag (111) TEM micrographs confirm the abundance of (111) crystallographic planes as seen in the XRD spectrum. Furthermore, the SAD patterns indicate that the domains align coherently in-plane. The cross-section and plan-view SAD patterns together indicate that both films retain the single-crystal-like epitaxial structure from the interface and throughout the whole film thickness. Although the XRD spectrum for the Ag (110) film indicates that some misoriented domains are present, the domains are presumably small, as the XRD peaks are several orders of magnitude weaker in comparison to the Ag (220) peak. No differently oriented domains were found in SAD patterns collected from different parts of the TEM specimens, indicating that the whole film is epitaxial. The epitaxial quality of the Ag (110) film is slightly lower than that of the Ag (111) film, but the domain size is greater in the former case. Ag preferentially grows in the close-packed (111) direction to minimize surface energy, and it has been previously reported that it is easier to achieve Ag (111) // Si (111) epitaxial growth than it is to achieve the Ag (110) // Si (110) relationship [124]. The film quality observed in this study is consistent with the previous observations. The large mismatch between the Ag and Si lattices is evident in the SAD patterns (Figure 16a-d). Ag and Si have a large lattice parameter mismatch (a_{Ag} = 4.09 and a_{Si} = 5.43 Å), with a mismatch strain, ε_m, of ~33%, calculated by using [93]:

$$\varepsilon_m = \frac{a_s - a_f}{a_f} \qquad \text{Equation 19}$$

where a_s and a_f are the lattice parameter of substrate and film. Based on such a large mismatch strain, 1-to-1 epitaxial growth is impossible. However, epitaxial growth of Ag on various low-index Si substrates has been achieved using various PVD techniques, and characterized by numerous analytical techniques [117, 124-129]. Epitaxial growth is achieved through domain matching epitaxy with a 3 Si-to-4 Ag domain match. Taking *n* and *m* as the number of respective substrate and film planes involved in the matching, the mismatch strain with domain matching epitaxy, ε_{dme}, is only -0.43%, estimated by using

$$\varepsilon_{dme} = \frac{na_s - ma_f}{ma_f} \qquad \text{Equation 20}$$

which is an adapted form of the equation used by Narayan and Larson [95] to estimate strain in domain matching epitaxy. The domain matching mechanism operates for both the Ag (111) // Si (111) and Ag (110) // Si (110) oriented films [117, 124].

III.5.2 The formation of high density growth twins

Cross-section TEM micrographs reveal a high density of twin boundaries oriented perpendicularly to the growth direction in the Ag (111) films. Similarly structured nanotwins have been observed in other fcc metal films, notably Cu and stainless steels [24, 64, 111]. The inclined twins observed in the Ag (110) film form an unusual structure, and it is likely that the formation mechanism during growth is somewhat different for these twin boundaries. While twins are observed regularly in micrographs of Ag films and bulk materials, the twins observed in this study differ significantly in the high frequency that they appear, and in their coherent orientation throughout the films. In the literature, most microscopy studies performed on Ag films focus on epitaxial growth, and hence steps were taken to minimize defect nucleation, such as using substrate heating and equilibrium deposition techniques like thermal evaporation or molecular beam epitaxy. Suppressing the formation of growth defects will also reduce the rate of twin formation. Twin density in such Ag films is typically much lower [122-123], with the twin variant only accounting for a volume fraction well below the ~ 50% seen in the current nanotwinned Ag (111) films.

Numerous factors lead to the formation of nanotwins in sputtered Ag films. First, Ag has a low stacking fault energy (γ_{sf}) of ~17 mJ/m^2 [23], which allows the formation of wider stable stacking faults than in metals with higher γ_{sf}. Thus a twin boundary, which is itself a stacking fault, can remain stable for longer lengths in Ag than in other metals. Low γ_{sf} also typically correlates with low twin boundary energy. Second, it has been shown from a thermodynamic model that twin boundary energy affects the formation of twin boundaries during film deposition by determining the difference in critical nucleation radius between defect free and twinned nuclei [51]. From the aforementioned model, the two respective critical nucleation radii, $r^*_{perfect}$ and r^*_{twin} are described by the following expressions:

$$r^*_{perfect} = \frac{\gamma}{\left(\frac{kT}{\Omega}\ln\left[\frac{J\sqrt{2\pi mkT}}{P_s}\right]\right)} \qquad \text{Equation 21}$$

$$r^*_{twin} = \frac{\gamma}{\left(\frac{kT}{\Omega}\ln\left[\frac{J\sqrt{2\pi mkT}}{P_s}\right]-\frac{\gamma_t}{h}\right)} \qquad \text{Equation 22}$$

where γ is the surface energy, k is the Boltzmann constant, T is the substrate temperature, Ω is the atomic volume, J is the deposition flux, m is the atomic mass of the film species, P_s is the vapor pressure above the target, γ_t is the twin boundary energy, and h is the height of the nucleus (taken in this case to be the {111} interplanar spacing). It is evident from the equation that a low twin boundary energy will facilitate the formation of nanotwins by reducing the critical radius for twin nuclei. Third, higher deposition rates facilitate the nucleation of twins as derived from the same thermodynamic model by further reducing the critical nucleation radius for twin formation to a value comparable to the critical radius for defect-free nucleation [51]. Figure 19 shows the relative difference between perfect and twin nuclei radius, $(r^*_{twin} - r^*_{perfect}) / r^*_{perfect}$, versus deposition rate for three monolithic metals, Ag, Cu and Al, with low to high twin boundary energy. For Ag films at a deposition rate of ~ 0.2 nm/sec, the relative radius difference is only 5%, which is considered sufficient for forming significant numbers of twin boundaries. The deposition rate used in this experiment for both films is ~29 Å/sec, and corresponds to a critical nucleation radius difference of only ~2.5%. The formation of dense twin boundaries in Cu has been observed at deposition rates of 20 to 40 Å/sec [64, 67] whereas growth twins are rarely observed in Al films.

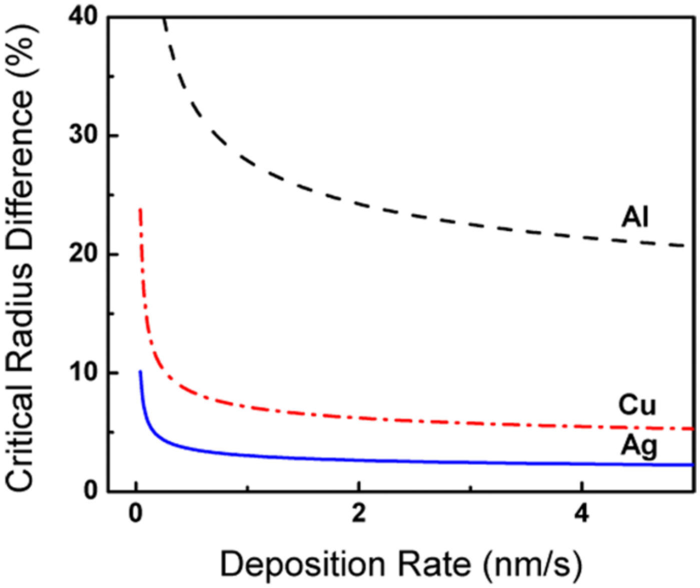

Figure 19: Plot of the relative difference between perfect and twin nuclei radius, $(r^*_{twin} - r^*_{perfect}) / r^*_{perfect}$, as a function of deposition rate. Curves computed for materials with high (Al) , moderate (Cu), and low twin boundary energy (Ag) show that the difference between the critical nucleation radius drops significantly with increasing deposition rate, and that Ag has a particularly small difference.

This thermodynamic model appears to accurately explain the formation of {111} high density growth twins in the Ag (111) films since the nucleation probability of twinned and perfect nuclei are close to equal. However, at the same deposition rate, the average spacing in Ag (110) films is drastically greater, ~ 42 nm, with a broad distribution (Figure 15b). The creation of any {111} coherent twin boundary requires the introduction of a Shockley partial dislocation, 1/6 <112>, in the close-packed {111} plane. In the Ag (111) films only in-plane coordinated movement of one atomic layer (via introduction of a Shockley partial) during growth is needed to form a twin boundary. For the thermodynamic model, the thickness of twinned nuclei is assumed to be the interplanar spacing of one {111} atomic plane, so the model is in agreement with the twin formation mechanism. However in Ag (110) films, as shown schematically in Figure 20, the introduction of a Shockley partial dislocation in the (111) plane will require the out-of-plane movement (partially along the growth direction) of at least 2-3 atomic layers.

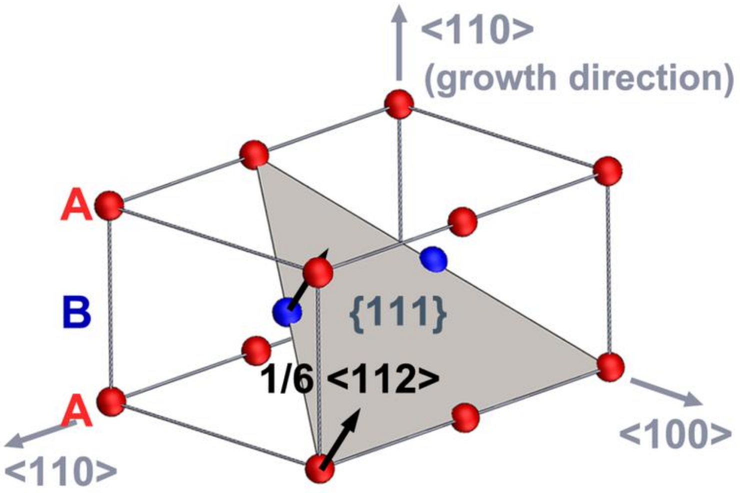

Figure 20: Schematics of the twin formation mechanism for the Ag (110) film. During growth the creation of a twin boundary on the inclined {111} plane by the introduction of a Shockley partial dislocation, 1/6 <112>, requires out-of-plane displacement of 2-3 atomic layers partially in the growth direction. In contrast, for the Ag (111) film, the nucleation of a twin boundary is created by displacing atoms by 1/6 <112> in-plane within one atomic plane normal to the growth direction, i.e. the movement of fewer atomic layers.

Hence, the probability for the nucleation of (111) twins is significantly reduced. Such analysis is qualitative in nature, but it indicates that the orientation of the close packed planes relative to the growth direction is another major parameter that can significantly affect the formation of growth twins.

It should be noted that in contrast to evaporation techniques, magnetron sputtering is a non-equilibrium process where adatoms have greater kinetic energy which allows them to diffuse across the substrate surface to preferentially fill voids and make a denser film surface. The relatively low Ar pressure used during the deposition also enhances this tendency towards fully dense (111) and (110) planes [130]. The Ag (111) epitaxial nanotwinned structure is quite unique as the defect density (i.e. (111) twin boundaries) is high, but the defects are coherently oriented throughout the film thickness.

At low magnification the boundaries between adjacent columnar domains in the Ag (111) films appear to be abrupt (Figure 13a-c). However, when examined more closely it is seen that the boundary is less clearly defined, and a significant number of twins do not actually terminate at the domain boundary. This coherency of twin variants across the domain boundary is highlighted in Figure 21. The two images compare the same area in bright field and dark field mode, and the black and white areas indicate two different twin variants. Many black and white twin variants extend across two or more vertical domain boundaries. Variants that terminate at the boundary show diffuse $\Sigma3\{112\}$ incoherent twin boundaries (ITB's), instead of the distinct high or low-angle grain boundaries seen in polycrystalline nanotwinned films. There is also evidence of the ITB's in the SAD pattern in the form of two extra spots between the zero-order and (111) spots (Figure 13b, inset). Similar ITB's have also been observed in Au and epitaxial nanotwinned Cu films [13, 20].

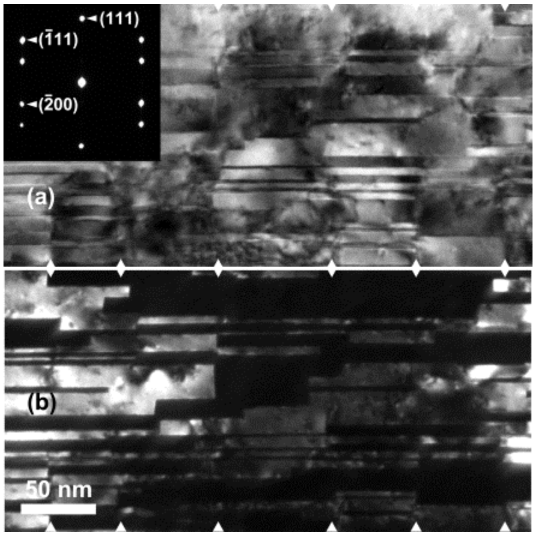

Figure 21: Cross-sectional TEM micrograph of twin boundaries in Ag (111) films examined along the Ag $[\mathbf{01\bar{1}}]$ zone axis in centered bright field (BF) and dark field (DF) mode. (a) In BF mode, the columnar domain boundaries (marked by the white triangles) appear as distinct barriers between the domains. (b) In DF mode the twin variants often extend through several apparent columnar domain boundaries.

III.5.3 The influence of twin boundaries on indentation hardness

There are some difficulties in comparing hardness values from different nanostructured Ag materials due to differences in measurement techniques. Bulk nanocrystalline specimens are typically analyzed by macro- and micro-hardness Vickers measurements [131-133], and it is difficult to directly compare nanoindentation experiments to such measurements. Hence we will only compare our nanoindentation results to other nanoindentation studies, even though the data available are limited. Indentation hardness results from this study and the literature (including bulk nanocrystalline, single crystals and other Ag films) are compared in a compiled Hall-Petch type plot in Figure 22 [118, 120-121, 134-136]. The horizontal axis in this plot is the size of the dominant microstructure feature that influences the transmission of dislocations, and hence the hardness. In most cases it is the grain size, but for the films in this study it is the average twin spacing. The slope is fitted for the values gathered from the literature. The indentation hardness from the Ag (111) film is lower than that predicted by the Hall-Petch slope for larger grains, but the film is ultimately harder than most other films reported in the literature. It has been shown [86] that in the region when dislocation pileup governs the hardening behavior of metal multilayers the critical resolved shear stress to pass a dislocation through the interface is expressed by

$$\tau_{HP} = \tau_0 + \left(\frac{Gb\tau^*}{(1-\nu)\pi h'} \right)^{1/2} \qquad \text{Equation 23}$$

where G is the elastic shear modulus, b is the Burger's vector magnitude, τ^* is the "barrier stress" of the layer boundary, ν is Poisson's ratio, and h' is the distance between obstacles. Based on Equation 23, τ^* is related to the slope of the Hall-Petch plot via

$$\tau^* = \left(\frac{\mathrm{k}_{\mathrm{HP}}^2 \pi (1-\nu)}{\mathrm{Gb}} \right) \qquad \text{Equation 24}$$

where k_{HP} is the slope of a Hall-Petch plot showing flow stress, σ, as a function of $d^{-0.5}$. To apply this relation, we assume that horizontal twin boundaries act similarly to layer interfaces as barriers to dislocation transmission. If we estimate $H \approx 3\sigma$ by the Tabor relation [137-138] and $\sigma \approx 3\tau^*$ using a Taylor factor of 3, then k_{HP} can be estimated by dividing the slope in Figure 22 by 8.1. We then apply Equation 24 with G = 30 GPa, b = 0.289 nm, and $\nu = 0.37$, to find $\tau^* \approx$ 0.532 GPa. Hence the peak hardness estimated using similar factors will be ~ 4.3 GPa. The Ag (111) films in this study achieve nearly 50% of this estimated peak hardness.

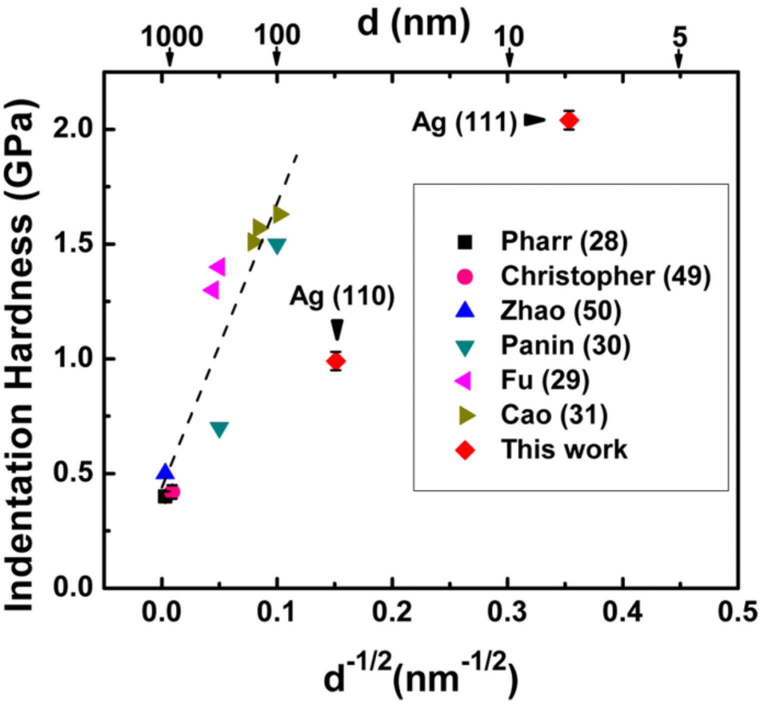

Figure 22: Nanoindentation hardness data from different Ag materials is compiled from different sources for comparison in a Hall-Petch type of plot. The results from bulk, bulk nanocrystalline, and other Ag films follow a clear linear relation as indicated by the dashed line. The Ag (111) films in this study deviate from the slope, and are among the highest reported indentation hardness results. The hardness of the twinned Ag (110) films deviates from the general trend, and the details are discussed in text.

Twin boundaries have been shown to increase the strength in other fcc metals by acting as barriers to the transmission of dislocations [24, 65, 78, 139]. However, the Ag (110) indentation hardness falls far short of the value predicted by the Hall-Petch slope in Figure 22 for an average twin spacing of 42 nm. During indentation normal to the twin boundaries in the Ag (111) films, there is very little shear stress resolved onto the twin planes, and hence twin boundary migration is less likely. In this case the hardness is dominated by dislocation activities confined between twin boundaries, which act as strong barriers to the transmission of dislocations. During normal indentation of the Ag (110) films with inclined twin boundaries, much more of the stress is resolved onto the twinned planes. This shear stress can be large enough to activate a large number of Shockley partial dislocations and hence lead to deformation by dislocation glide along the twin boundary, and twin boundary migration is more likely. The migration of twin boundaries has been observed by *in situ* nanoindentation studies in nt Cu, and in parallel by MD simulations [115]. The deformation associated with inclined {111} twin boundaries may lead to the much lower strength (softening) observed in Ag (110) films. Further work is under way to investigate this phenomenon. The indentation hardness values seen in the Ag (110) films are greater than those seen for most other Ag films [120-121]. It is probable that the lower deposition rate (~5 Å/sec) used by Cao, *et al*, [121] resulted in a lower twin density than in this study. The twin densities in the Ag films deposited by Panin, *et al,* [120] are not available, but likely are lower as well.

III.6 Conclusions

Epitaxial nanotwinned Ag (111) and Ag (110) films were grown successfully on Si (111) and Si (110) substrates by magnetron sputtering. The microstructures of these two types of films differ in the density and orientation of twin boundaries. Both films show greatly enhanced hardness in comparison to bulk Ag. Besides the deposition rate and stacking fault energy, we have rationalized that the orientation of close-packed {111} planes can play a significant role in varying twin density. The strengthening effect can be attributed to high densities of growth twins that resist the transmission of single dislocations, and the different orientation and density of twin boundaries in the Ag (111) and (110) films lead to quite different indentation hardness values. High density twins significantly improve the mechanical strength of the Ag films, which might make Ag more attractive for various industrial applications such as in microelectronics.

CHAPTER IV

THERMAL STABILITY OF TWINS AND STRENGTHENING MECHANISMS IN DIFFERENTLY ORIENTED EPITAXIAL NANOTWINNED SILVER FILMS[*]

IV.1 Overview

Sputter-deposited epitaxial (111) and (110) Ag films have high-density nanotwins with respective twin boundary orientations perpendicular and angled to the growth direction. Twin density in as-deposited (111) Ag films is much greater than in (110) films, leading to higher hardness in the (111) films. Annealing up to 800 °C (homologous temperature of 0.85 T_m) leads to increased twin thickness, although average twin thickness remains less than 100 nm in both systems. Twinned volume fraction falls dramatically in annealed (110) films, but remains constant at ~ 50% in (111) films. The mechanisms leading to the elimination of nanotwins in (110) films and their remarkable stability in the (111) films at elevated temperatures is discussed. Coarsening and elimination of twins result in hardness reduction after annealing. The variety of microstructures achieved via annealing allow for the introduction of a strengthening model considering both twin and grain boundaries.

---

[*] This chapter reprinted with permission from "Thermal Stability of Twins and Strengthening Mechanisms in Differently Oriented Epitaxial Nanotwinned Ag Films" by D. Bufford, H. Wang, and X. Zhang, 2013. *Journal of Materials Research*, Volume 28, Issue 13, pp 1729-39, Copyright 2013 by Cambridge University Press.

IV.2 Introduction

Nanotwinned (nt) face-centered cubic (fcc) metals have gained intense interest recently due to their unique assortment of desirable properties, including low electrical resistivity, high strain rate sensitivity [57, 140-141], improved mechanical stability under cyclic loading [55, 142], and increased mechanical strength [30, 32-33, 57, 65-67]. Different nt materials fabricated by pulsed electrodeposition [33] and magnetron sputtering [24, 80] have various twinned microstructures, including randomly oriented polycrystalline grains filled with dense twin boundaries and, in certain cases, single-crystal-like epitaxial structures (in sputtered Cu and Ag) with extremely high densities of twin boundaries exclusively oriented normal to the growth direction [24, 51, 67]. The contributions of nanotwins to high mechanical strength have garnered special attention [33]. Numerous studies demonstrated that twin boundaries act similarly to grain boundaries when blocking transmission of dislocations, and nt metals exhibit strength similar to their nanocrystalline (nc) counterparts [57, 141]. However, given that twin and grain boundaries in most cases are significantly different in length scale, various microstructures must be carefully incorporated into strengthening models. Gu, *et al*, proposed a strengthening model that considered simultaneously the influence of twin boundaries and grain boundaries [143]. Meanwhile, twin boundaries also contribute to enhanced ductility and work hardening, properties usually lacking in nc metals [144]. Twin boundaries store dislocations during rolling [52] and tensile tests [140], and twin boundary/dislocation interactions produce sessile dislocations that may lead to enhanced work hardening [37, 92].

Metals with nc microstructures store large amounts of energy within abundant grain boundaries, such that nc microstructures are often not at thermodynamic equilibrium [12]. Grain coarsening provides a pathway to reduce this energy, so nc metals typically show poor thermal stability, and the resulting grain growth quickly leads to significant softening. However, the Σ3 <111> coherent twin boundary (CTB) typically has an order of magnitude lower energy than high angle grain boundaries, making CTBs inherently more thermally stable. For instance in Cu, coherent twin boundary energy and high angle grain boundary energy are 24-39 and 625-710 mJ/m^2, respectively [22-23]. Hence, twin boundaries in sputtered polycrystalline nt Cu grow more slowly than grain boundaries, allowing the metal to retain dense twins (and thus significant strength) even after annealing to 80% of the melting temperature, T_m [63-64]. The Σ3 <112> incoherent twin boundary (ITB) has been observed in nt Cu [13, 67, 145], with calculated energies of 590 to 714 mJ/m^2 [13], comparable to energies of low- and high-angle grain boundaries. Recent *in situ* studies and computational investigations of nt metals have revealed the importance of ITBs in mechanical deformation and twin boundary migration/detwinning under stress or heating [29, 38, 62, 146].

Recently we showed that epitaxial (111) Ag films have twin boundaries parallel to the film surface and average twin thickness, t_{twin}, is ~ 10 nm, whereas epitaxial (110) Ag films have inclined twins (at ~30° to the film surface) with t_{twin} of ~ 42 nm [80]. Zhang and Misra proposed that twin orientation may affect thermal stability [63]. Thus, the two epitaxial nt Ag systems are ideal to validate the foregoing hypothesis. In this study, we show that twin orientation can indeed result in dramatically different thermal stability of twin boundaries.

Furthermore, the influences of grain boundaries and twin boundaries on strengthening are discussed by introducing a new parameter, effective dimension, which reconciles the large discrepancy in size dependent strengthening should grain size or twin spacing be used alone.

IV.3 Experimental

Ag films, 2 μm in thickness, were deposited onto HF-etched single crystal silicon substrates with (111) and (110) orientation. Base pressure prior to deposition was ~ 6×10^{-8} torr, and argon pressure during sputtering was ~ 2×10^{-3} torr. X-ray diffraction (Bruker-AXS D8 Bragg-Brentano X-ray Diffractometer, Cu Kα radiation) was used to check for epitaxial film quality. Prior to annealing the tube furnace was evacuated and purged with ultra-high purity Ar gas (99.99 %) three times. The furnace reached 400 °C in approximately 10 minutes and 800 °C in 25 minutes. Isothermal annealing was performed for one hour at 200 - 800 °C with constant Ar gas flow. Before being retracted, films were allowed to cool in the furnace to approximately 60 °C, a process that took up to ~4 hours from 800 °C. Film surfaces were shiny, free of discoloration, and showed no signs of de-lamination from the substrates after annealing. Cross-section transmission electron microscopy (XTEM) specimens were prepared via mechanical grinding and polishing, followed by low-angle ion milling, then examined along perpendicular zone axes with a JEOL 2010 microscope with 200kV accelerating voltage. Hardness was measured via an instrumented nanoindentation method performed using a Fischerscope HM2000XYp micro-/nano-indenter with a Vickers indenter tip. Hardness vs. depth analysis was performed to choose an appropriate depth to avoid problems associated with both small indentation size and substrate effects. A minimum of 9-12 good indentations were performed at each indentation depth.

IV.4 Results

IV.4.1 Annealing effects on the microstructure of epitaxial nt (111) Ag films

Microstructure evolution of (111) Ag films at various annealing temperatures is shown in Figure 23. Several characteristics are noteworthy. First, as-deposited films had twin boundaries essentially parallel to the substrate (or film surface), and the two variants (twin and matrix) had relatively low dislocation density. Second, the inset selected area diffraction (SAD) patterns show that all films remained epitaxial. ITBs have a unique repeating microstructure, that is they consist of groups of 3 atomic layers with a Shockley partial dislocation on each consecutive (111) plane, and the summation of Burgers vectors within each triplet is zero [147]. Hence, the strong extra diffraction spots in as-deposited films arose from ITBs. However, ITB diffraction spots became faint by 400 °C, and nearly disappeared at higher annealing temperatures. Third, columnar domain size and twin thickness both increased at higher annealing temperatures. Columnar domain size was initially 94 nm, and it increased to 134 nm at 200 °C, and to nearly 350 nm by 400 °C (Figure 23 a-c). At 600 and 800 °C well-defined columnar domain boundaries were rarely seen; instead each twin variant extended beyond hundreds of nanometers to microns parallel to the substrate (Figure 23 d,e).

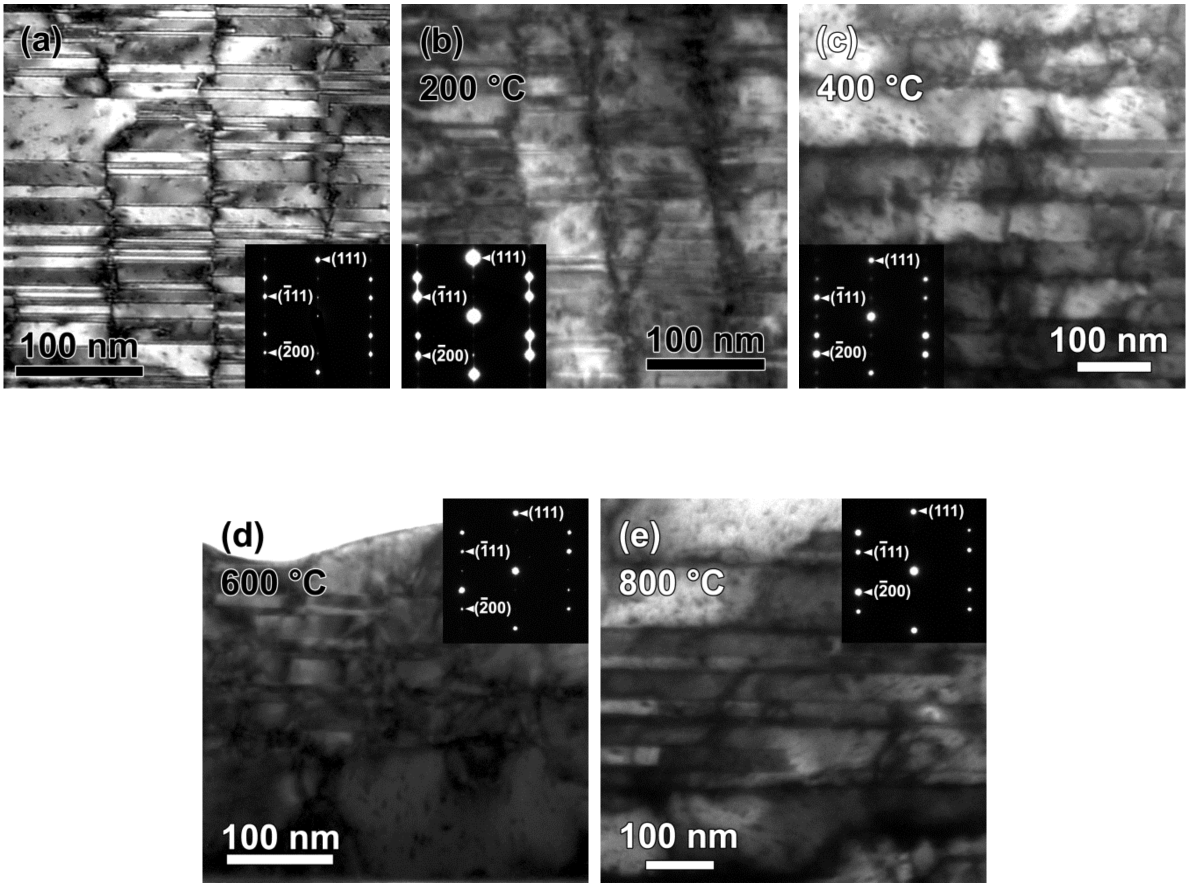

Figure 23: Cross-section TEM (XTEM) micrographs (<011> zone axis) of (111) Ag films. Micrograph (a) corresponds to the as-deposited films, while b-e correspond to samples annealed at 200, 400, 600, and 800 °C. While only a small increase in columnar width appeared in (b), the width increased dramatically in (c). The corresponding inset SAD patterns provide evidence of epitaxial nt microstructures. Extra spots arose from ITBs in (a). In (d) and (e) columnar boundaries no longer appeared, and extra ITB spots were absent from the inset SAD patterns. Twin thickness gradually increased across the range of annealing temperatures.

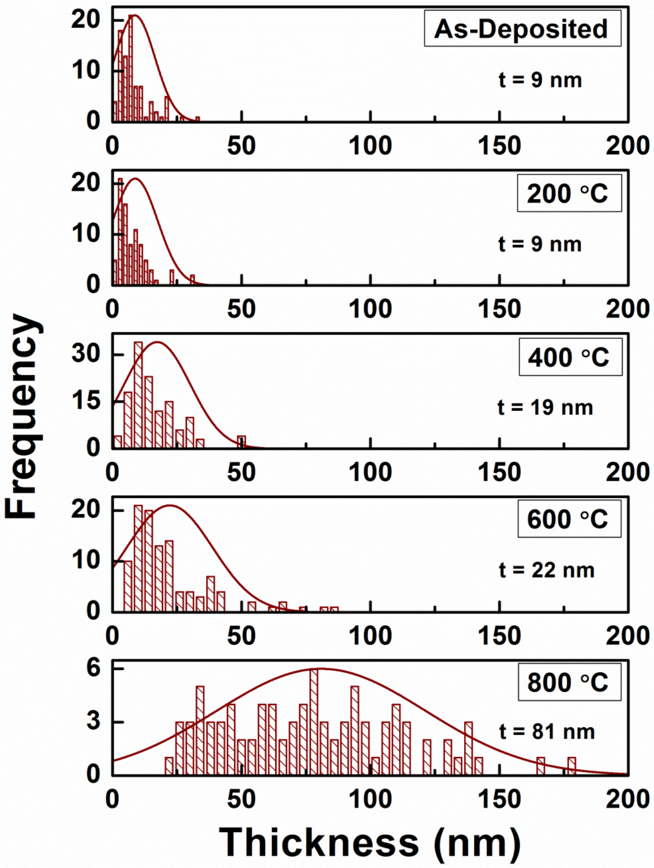

Figure 24: Twin lamella thickness histograms for (111) Ag films annealed at various temperatures. While annealing at 200 °C produced little change in the twin thickness, annealing at 400 and 600 °C causes a gradual increase in average twin thickness, as well as a broadening of the distribution. A dramatic spread of the distribution accompanies the sharp increase in average twin thickness at 800 °C. Still the structure remains heavily twinned, despite being heated to nearly 90% of the melting temperature. Due to the dense twins and essentially equal volumes of twin and matrix variants, twin and matrix lamellae are included together in these histograms.

Figure 24 shows a narrow size distribution of twins in as-deposited (111) Ag films, which was essentially unchanged after annealing at 200 °C, remained narrow through 600 °C, but at 800 °C became much broader. Up to 200 °C, t_{twin} remained unchanged, ~ 9 nm, and then gradually grew to 22 nm by 600 °C. However, at 800 °C t_{twin} increased rapidly to 81 nm. Despite the twin thickness evolution, twin and matrix volume fractions in (111) Ag films remained unchanged (Figure 25), both ~ 50% throughout the range of annealing temperatures, so a distinction between the two variants is arbitrary.

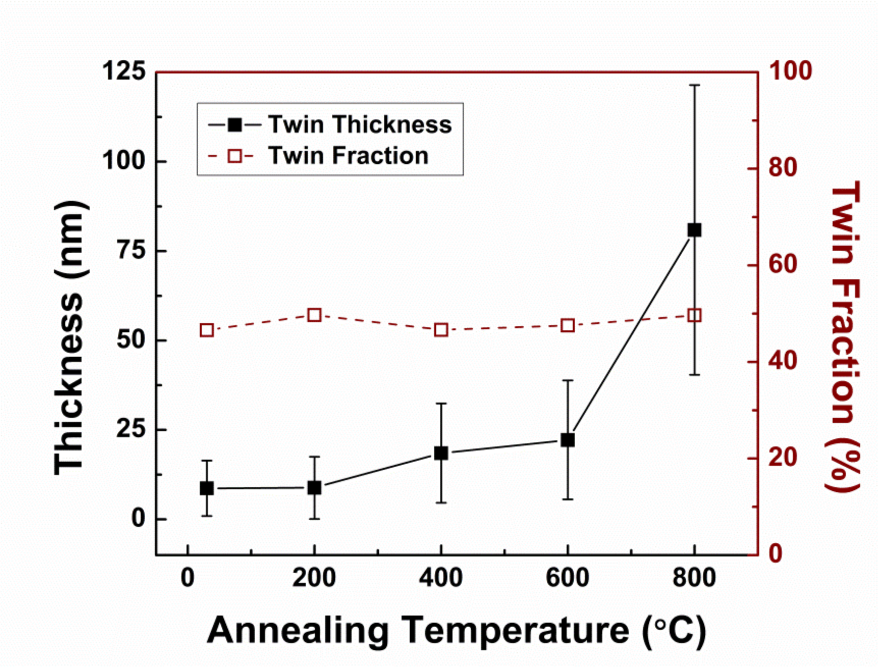

Figure 25: Average twin thickness in (111) Ag films increased with annealing temperature. The twin thickness increased only moderately up to 600 °C, growing by less than a factor of 2.5. After annealing to 800 °C twin thickness increased rapidly by a factor of ~ 10. Throughout the range of annealing temperatures the twin and matrix volume fractions remained essentially constant at ~50% each.

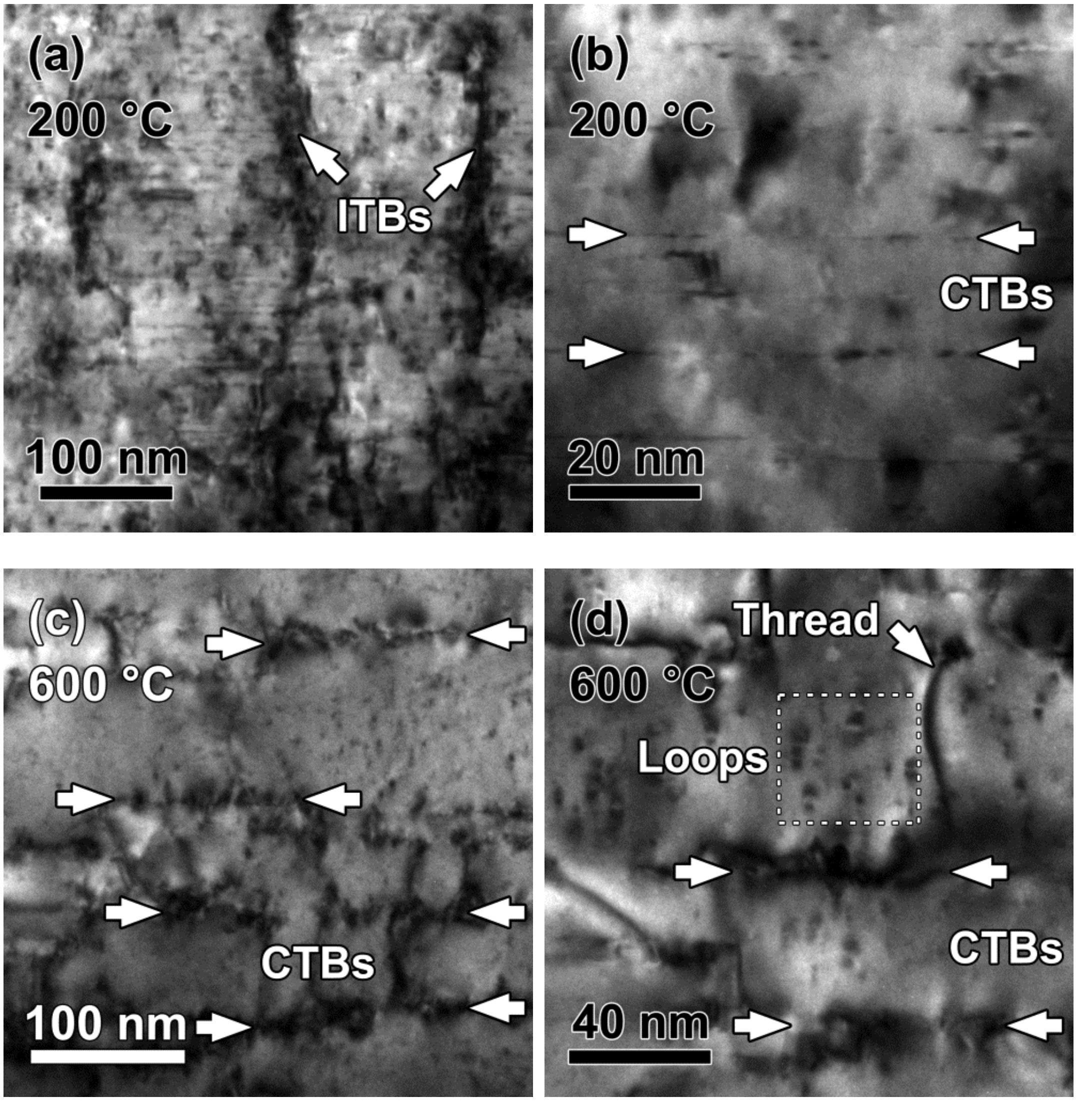

Figure 26: XTEM micrographs of (111) Ag films examined along the <112> zone axis. After annealing to 200 °C, at low magnification (a) ITBs (marked by arrows) are the main visible features, while at higher magnification (b) a few straight CTBs appear as horizontal dotted lines due to dislocations pinned to the boundaries. After annealing to 600 °C, at low magnification (c) more dislocations were pinned along CTBs (between the arrows), and ITBs no longer appear. A micrograph taken at higher magnification (d) reveals long threading dislocations and dislocation loops (inside the dotted box) in the annealed films. The defect density along the CTBs increased such that the CTBs were distorted and no longer smooth.

When (111) Ag films were examined from the <112> Ag zone axis, columnar domain boundaries were easily identified within as-deposited and 200 °C annealed films, whereas CTBs appear as faint dotted lines due to a few dislocations pinned along the boundaries as shown in Figure 26a,b. At higher annealing temperatures an increasing number of dislocations are pinned to twin boundaries, so twin boundaries were more readily identifiable from the <112> zone axis (Figure 26c-d). In (111) films annealed at 600 °C, tangles of dislocations appeared at the twin boundaries, along with numerous dislocations threading through the thickness of twins. Dislocation loop density also increased slightly after annealing.

IV.4.2 Annealing effects on the microstructure of epitaxial nt Ag (110) films

In these films the matrix variant was more prevalent in the as-deposited case, so a distinction between matrix and twin variants is appropriate (Figure 27a). Inclined twin boundaries in the (110) films behaved differently after annealing from those within (111) films. Again, t_{twin} increased, but twinned volume fraction also decreased (Figure 27b-e) due to a reduction of twin density and significant increase in matrix thickness. As in the (111) Ag films, a small increase in dislocation loop density appeared throughout the films as annealing temperature increased. SAD patterns reveal that the films maintain epitaxial character through the annealing temperature range. As shown in Figure 28, annealing at 200 °C produced essentially no difference in average twin thickness in the (110) films. The twin thickness distribution remained relatively narrow throughout annealing, compared to a much broader distribution of matrix thickness.

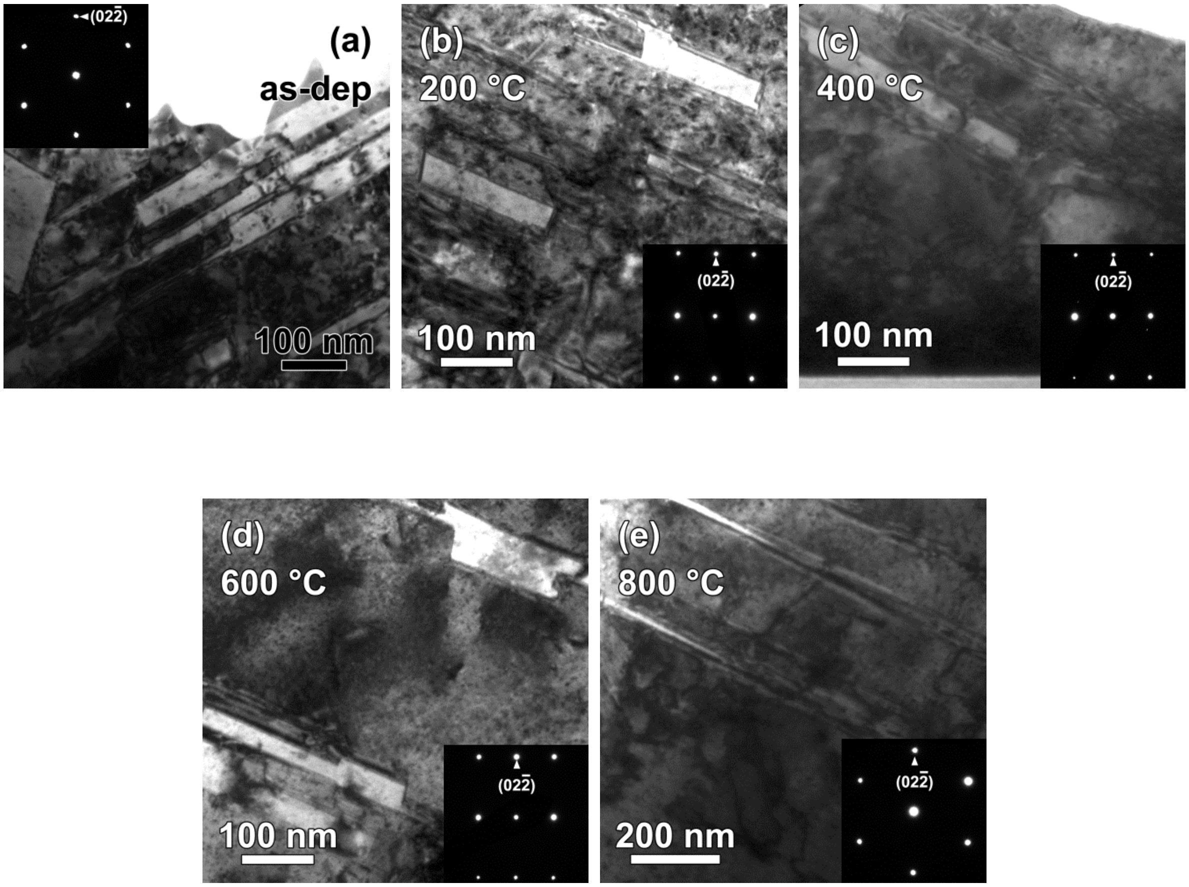

Figure 27: XTEM micrographs (110) Ag films examined along <111> (Figure 5a and 5e) or <112> zone axis. Micrograph (a) corresponds to the as-deposited films, while b-e correspond to samples annealed at 200- 800 °C. Annealing induced a dramatic drop in the twinned volume fraction. A large volume of twins of different orientations dominated in (a), but after annealing to 200 °C (b), the twinned fraction already began to decrease. The decrease continued through 800 °C (e), where the volume fraction of twins is merely ~1%.

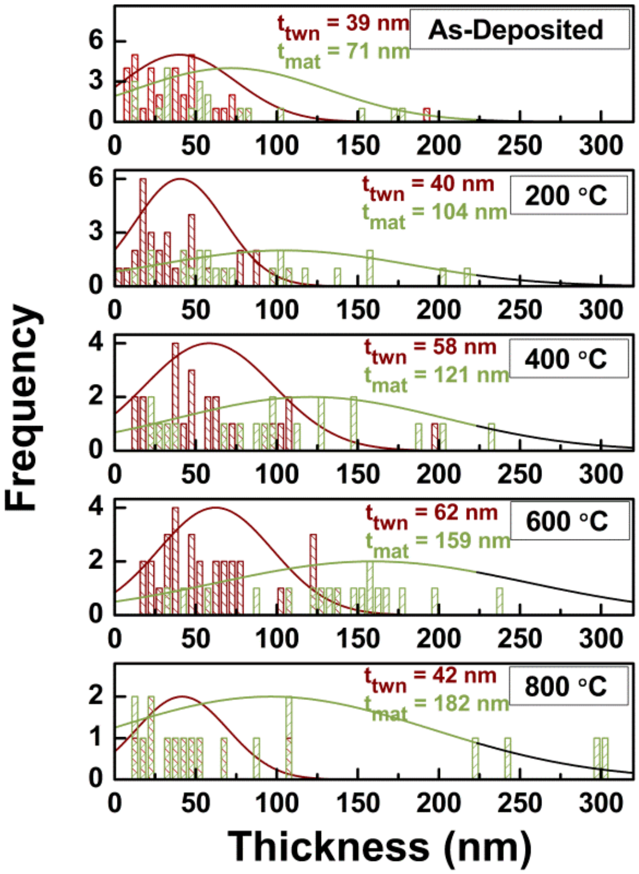

Figure 28: Twin and matrix lamella thickness histograms of (110) Ag films at various annealing temperatures. Matrix thickness increased rapidly with increasing annealing temperature, and the distribution broadens as well. Annealing at up to 600 °C caused a slight increase in average twin thickness, followed by a reduction at 800 °C.

With increasing temperature, t_{twin} increased moderately from 39 nm to a peak value (~ 60 nm) at 600 °C, and then decreased thereafter at 800 °C. Average matrix thickness increased continuously with higher annealing temperature from 71 to ~ 180 nm. In contrast to (111) textured Ag films, the twinned volume fraction decreased markedly from 25% in as-deposited films to only 1% at 800 °C (Figure 29).

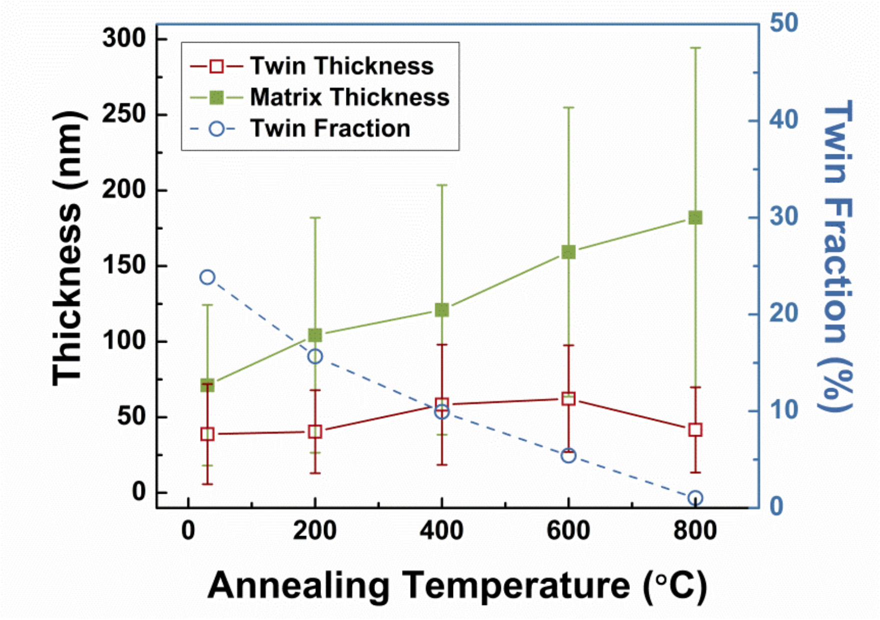

Figure 29: Evolution of average twin and matrix lamella thickness and volume fraction of twins with annealing temperature in (110) Ag films. Matrix thickness grew steadily with increasing annealing temperature. Meanwhile the volume fraction of twinned variants decreased from ~25% to ~1%. The average twin thickness increased moderately during annealing and eventually decreased at 800 °C.

IV.5 Discussion

IV.5.1 Phase stability and elimination of intermixing

Diffusion of Ag into Si is much less dramatic than Cu into Si [148]. Ag has low solubility in Si (1 ppm at 1100 °C, and falling quickly as temperature decreases [149]), and it forms no stable silicide. The Ag-Si binary system undergoes a eutectic reaction at 836 °C [150], however, all annealing temperatures were below this threshold. According to studies performed by Weber [149], solubility of Si in Ag at 400 °C and below is negligible. Solubility rises to 0.1% by 600 °C and 0.7% by 800 °C. Overall, the microstructures were homogeneous, with no noticeable differences near the substrate, indicating that any Si contamination within the film was negligible.

IV.5.2 ITB migration in the (111) films

ITB migration is an important phenomenon directly related to both mechanical and thermal stability of twins [29, 38, 146].

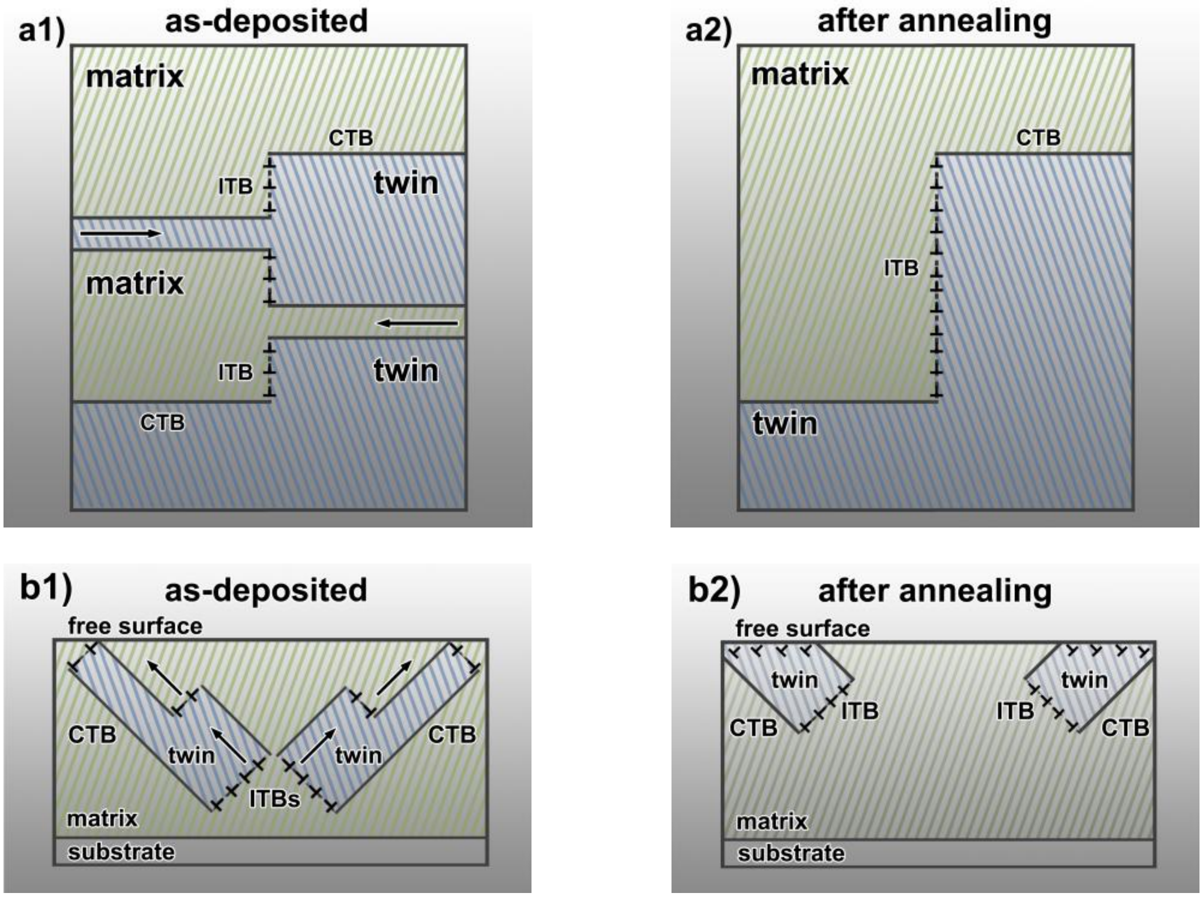

Figure 30: Schematic representations of annealing induced twin evolution in (111) films (a1-a2) and in (110) films (b1-b2). In panel (a1), the twin and matrix occupy equal volumes, and average twin thickness is small due to the inclusion of small twins. Elevated temperature can cause an ITB to move (with equal probability) either left or right along (111) planes parallel to the substrate, indicated by the arrows. The driving force for ITB migration is larger for thinner twins, so the thinner twins begin to move first. After propagating (a2) the twinned fractions remain the same, but average thickness has increased substantially. In the (110) films (b1) none of the (111) planes are parallel to the substrate. Image forces from the free surface draw dislocations towards the surface, where they exit the film. This process allows the matrix to grow at the expense of the twinned variants (b2).

Partials comprising ITBs reside on successive (111) planes, and they migrated along their native {111} planes parallel to the substrate surface (and hence CTBs). Since no external forces acted on the film during annealing, there was little shear stress resolved onto other slip systems inclined to CTBs. Consequently, ITBs migrated in directions parallel to CTBs. Depending on the direction of movement, ITBs may either retract or extend the twin variant as they propagate, as shown in Figure 30a1-a2. The increase of t_{twin} with temperature suggests the preferential removal of thinner twin variants. The driving force for detwinning is the reduction of overall system energy, and the driving force for ITB migration is estimated as $2\ \gamma_t/t$, where γ_t is twin boundary energy and t is twin thickness [29]. Thus, migration velocity of thinner twins is greater than that of the coarser twins. Consequently, average twin spacing increased as finer twins were eliminated. Volume fractions of twin and matrix remained 50% after annealing as thin variants of twins or matrix have equal probability of removal during annealing (Figure 30a1-a2). Migration of ITBs in (111) Ag films was noticeable even at 200 °C, as domain size increased from ~ 95 to 135 nm. By 400 °C twin spacing doubled, and ITBs had moved substantially, as evidenced by an increase of domain size to ~350 nm. By 600 °C it was apparent that ITBs were nearly exhausted, hence the film had a lamellar structure consisting mostly of wide twin variants, with widths up to microns.

With few ITBs left after annealing at high temperatures (above 400 °C), the primary partial dislocation source for detwinning was significantly depleted. Thus, further removal of twin boundaries had to occur by dislocation climb. Climb is a non-conservative, thermally activated process. Based on isotope diffusion experiments, the self-diffusion coefficient in Ag has been measured to increase rapidly from 3×10^{-18} cm^{2}s^{-1} at 300 °C to 5×10^{-10} cm^{2}s^{-1}

at 800 °C, indicating that self-diffusion (and thus the rate of dislocation climb) increases dramatically at higher annealing temperatures [151-153]. Hence, twin thickness only increased slightly by ~ 4 nm from 400 to 600 °C (Figure 3a), while the abrupt increase in twin spacing at 800 °C can be attributed to increased activation of these diffusion processes. The temperature-dependent increase in twin thickness was largely similar to behavior seen in polycrystalline nt Cu [64], wherein t_{twin} increased by a factor of 2 at 600 °C, and doubled again at 800 °C, while columnar grain size in Ag increased even more rapidly. Cu has a higher melting temperature than Ag (1085 °C vs. 962 °C), so the magnitude of the increase in t_{twin} at 800 °C in Cu is less than that in nt Ag. Additionally, Fe impurities in polycrystalline nt Cu films may have enhanced resistance to the propagation of grain and twin boundaries. Curved twin boundaries in (111) Ag films annealed at 400 °C and above (Figure 23d-e) actually consist of mixed steps of CTBs and ITBs. Glide of partial dislocations along {111} planes could generate these steps, and thus form what looks like a bent or curved twin boundary.

IV.5.3 ITB migration in the (110) films

Within the (110) Ag films many twin and matrix variants extended up to hundreds of nm even in the as-deposited state, and ITBs bound the ends of each variant. In (110) films all 12 slip systems are oriented at angles to the substrate. Since Shockley partials have very high migration speed on {111} planes, ITBs can migrate over large distances and thus may frequently encounter the film surface or film-substrate interface. Partial dislocations (comprising ITBs) are drawn toward free surfaces due to the dislocation image force, and conversely repelled by rigid surfaces like the Ag-Si interface. Thus, a majority of partials may exit the film via the free surface as illustrated in Figure 30b1-b2. The image force on a dislocation is given by

$$F_x = -\frac{\mu b^2}{4\pi k x}, \qquad \text{Equation 25}$$

where μ is shear modulus, b is Burgers vector, x is distance between the dislocation and the surface along the film normal (x) direction, $k = 1$ for screw dislocations, $k = (1-v)$ for edge dislocations, and v is Poisson's ratio [154]. Image forces are significant when dislocations are close to free surfaces or interfaces. Most {111} planes in (110) films intercept the free surface, so image forces may establish a biased migration of partial dislocations, which continuously drives dislocations towards the free surface, where they will be eliminated. The combination of detwinning caused by ITB motion and ejection of dislocations at the free surface caused the twin fraction in (110) films to fall rapidly to 1% by 800 °C, in stark contrast to the case of the (111) films, where the twinned fraction remained ~ 50% over the entire annealing range.

IV.5.4 Effects of the mismatch stress on microstructure evolution

The difference in coefficient of thermal expansion between film and substrate may also affect microstructure evolution. Although Ag and Si have a substantial difference in lattice parameters (4.09 Å in Ag and 5.43 Å in Si), epitaxial Ag films on Si assume a 3 Si - to - 4 Ag domain match, resulting in an in-plane mismatch strain of only 0.43%. Hence, the Ag film experiences a compressive in-plane strain at the interface at room temperature. Ag expands more rapidly than Si, so the strain rises to 1.7% at 800 °C. We compute a corresponding elastic compressive stress in Ag varying from 360 to 1400 MPa with increasing temperature. Resolved shear stress arising from this compressive stress may drive partials on inclined twin boundaries to propagate rapidly in the (110) films. In (111) nt Ag, however, the same compressive stress generates little resolved shear stress on partials residing on the (111) planes parallel to the substrate. Furthermore, during cooling considerable tensile stresses can develop within the films, may lead to dislocation loop formation. Loops may also form directly as a result of annealing, and may be stabilized by rapid quenching [155]. However, the slow cooling rates used in this study may not lead to a significant increase in loop density after cooling.

IV.5.5 Annealing effects on the evolution of mechanical properties

At 200 °C, hardness of the (111) films barely changed (Figure 31), however, moderate softening occurred in (110) films. At higher temperatures, the hardness of (111) films fell rapidly by 1.1 GPa, compared with a gradual softening of 0.3 GPa in (110) Ag. Respective hardness values of the (111) and (110) films dropped by ~ 55% and ~ 40%, similar to the percentage drop seen in polycrystalline nt Cu over a similar annealing temperature range [64]. Hardness values for the two films converged by 800 °C, with the (111) films having slightly higher hardness (~ 100 MPa). Interestingly, the hardness of both films remained quite high in comparison to coarse-grained bulk Ag (~ 0.4 GPa) despite heating to ~ 87% of the melting temperature [118, 134]. The orientation of the applied load with respect to twin boundaries has been shown to affect deformation behavior in nearly single-crystal nt Cu nanopillars deformed under uniaxial tension [156]. However, the effect seems to be much smaller in samples tested via indentation, where the orientation of indentation with respect to twin boundaries can lead to a hardness difference of ~10% in the extreme case [55].

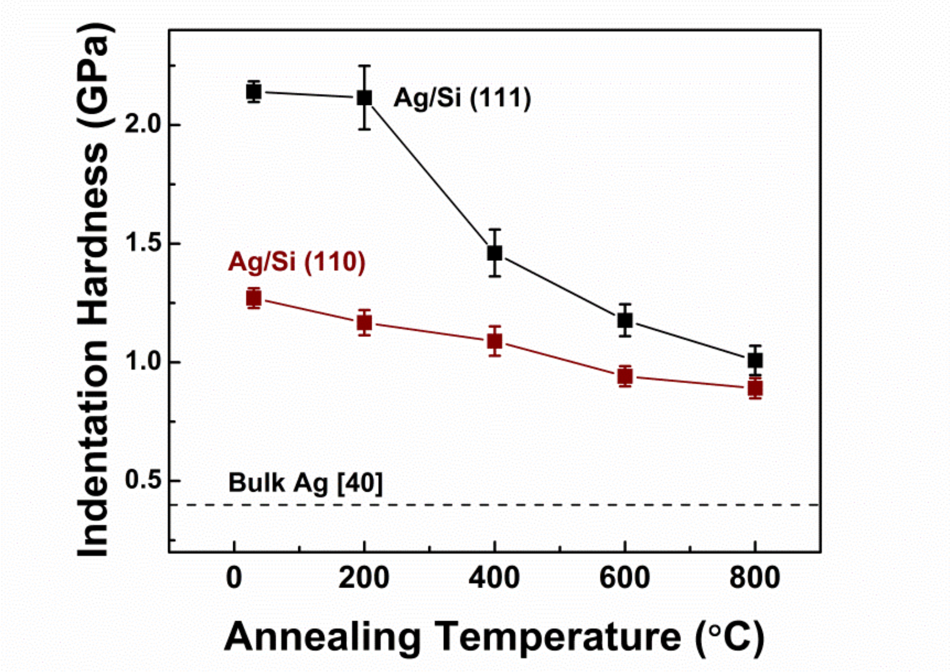

Figure 31: Evolution of film hardness as a function of annealing temperature. In the (111) films, hardness remained constant after annealing to 200 °C, but drops rapidly thereafter to ~ 1 GPa. In the (110) films the hardness steadily decreased through the temperature range.

High density dislocation loops may explain the hardness retained (relative to bulk) in annealed (111) and (110) Ag films. Hardening caused by dislocation loops can be calculated by a dispersed barrier model,

$$\Delta\tau = \alpha' \mu b \sqrt{N d_{loop}}\,, \qquad \text{Equation 26}$$

where τ is critical shear stress, α' is a parameter that depends on average barrier strength of the loops, N is loop density, and d_{loop} is loop size [157]. The TEM foil thickness was measured by using a convergent-beam electron diffraction technique [107], and dislocation loop density was determined by counting loops in areas of measured film thickness. We choose parameters for Ag as follows: $\alpha \approx 0.16$ to .3 [158-159], $\mu = 30$ GPa, and $b = 0.289$ nm. We take $\sigma_{\mathrm{flow}} \approx 3\tau$ (by using a Taylor factor of 3) and approximate indentation hardness by the Tabor relation $H_{\mathrm{IT}} \approx 2.7\sigma_{\mathrm{flow}}$ [137-138]. For both cases, d_{loop} was measured to be ~ 3 nm. For the (111) and (110) Ag annealed at 800 °C, loop density was ~ 1.2×10^{23} and 7.6×10^{22} m^{-3}, respectively, thus leading to expected hardness increases of 270 and 200 MPa over loop-free Ag.

IV.5.6 Strengthening due to both grain boundaries and twin boundaries

Often t_{twin} (which is typically much smaller than average grain size) is used as the dominant feature size to explain size dependent strengthening in nt fcc metals [64]. As seen in Figure 32, if t_{twin}, alone is used as the primary feature size (open squares in Figure 32), the fitted line has a slope far below the fitted line from the literature data (from other experimental investigations of polycrystalline Ag) wherein grain size is the dominant feature size [118-121, 134-135]. The Hall-Petch slope is an indicator of barrier resistance to dislocation transmission. Hence, a drastic difference in slope leads to the illusion that grain boundaries are far more effective dislocation barriers than TBs. Hence, t_{twin} alone does not fully explain size dependent strengthening in annealed nt Ag.

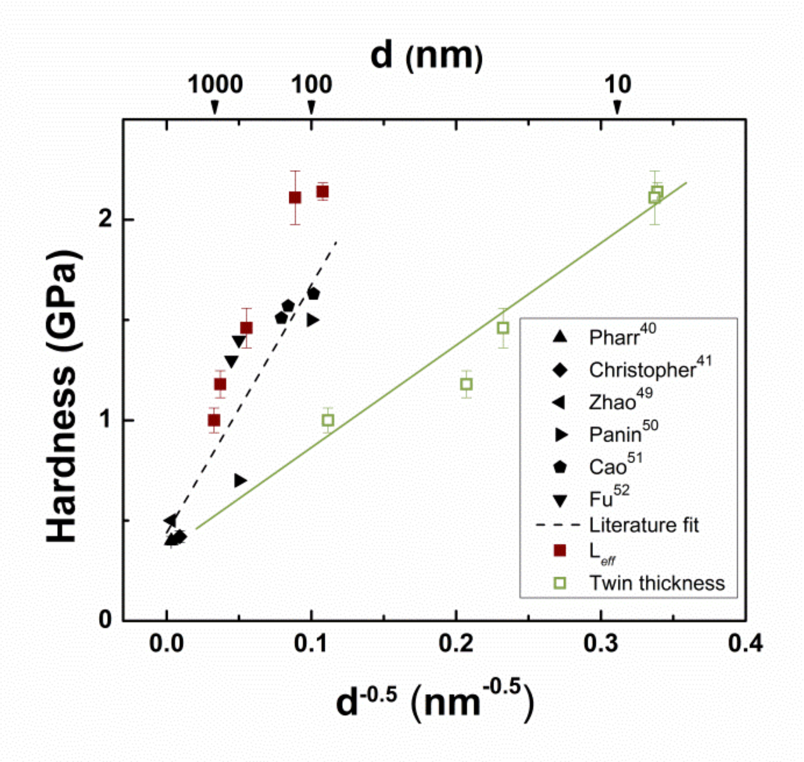

Figure 32: Evolution of indentation hardness of (111) Ag films with $d^{-0.5}$ or $t^{-0.5}$, where *d* and *t* represent grain size and twin spacing respectively. The linear fit of literature values is used as a reference. When the hardness of nt Ag is plotted as a function of average twin thickness alone, the linear fit leads to a slope much lower than the literature curve. However, the effective domain size, L_{eff}, as defined in the text gives values close to literature data.

Gu, *et al*, developed the non-uniform partial dislocation model by considering the influence of both twin boundaries and grain boundaries on flow stress [143, 160-161]. In that model, flow stress for propagation of partial dislocations is considered to be the average of flow stresses required to move partials towards and parallel to twin boundaries. Although both grain size and twin spacing are used to describe flow stress, a unified length scale that determines size dependent strengthening mechanism has not been identified. An effective barrier spacing, L_{eff}, if derived, may better describe size dependent strengthening in nt Ag, and such a feature size would be useful practically to compare the strength of polycrystalline nt metals to their counterparts free from twins. For microstructures with anisotropic grain structures (like the lamellar domain and twin boundaries in this study), L_{eff} must reflect an average intercept distance based on the length and width of the grains [162], which can be accomplished by considering dislocation pile-up against both types of boundaries.

For sputtered Cu with columnar grains filled with twin boundaries, Dahlgren and Merz geometrically determined an overall mean intercept distance, $\bar{l}$, for hexagonal columnar grains that considered both t_{twin} and columnar grain diameter, d [50]:

$$\bar{l} = 2\left(\frac{1}{t_{twin}} + \frac{2.31}{d}\right)^{-1}. \qquad \text{Equation 27}$$

Unfortunately, using this mean intercept in the revised Hall-Petch plot (not shown here) still leads to substantially lower H-P slope than that for polycrystalline Ag.

In an attempt to quantify relative strengthening contributions from twins and domains, we consider a modified form of the Hall-Petch relation for size-dependent strengthening. In polycrystalline metals, the number of dislocations N_d piling up against a grain boundary can be described as

$$N_d = \frac{\pi(1-\nu)d(\tau-\tau_0)}{Gb}. \qquad \text{Equation 28}$$

where τ is applied shear stress, and τ_0 is lattice friction stress [3]. The stress at which the leading dislocation slips across a grain boundary, τ^*, is given by the following relation [3]:

$$N_d(\tau-\tau_0) = \tau^* \qquad \text{Equation 29}$$

Combination of Equations 28 and 29 leads to a formulation of the Hall-Petch relation [3]:

$$\tau = \tau_0 + \left(\frac{Gb\tau^*}{\pi(1-\nu)d} \right)^{1/2} . \qquad \text{Equation 30}$$

When dislocations are likely to pile up against both grain and twin boundaries with disparate spacing, L_{eff} replaces *d*. In this case Equation 29 can be redefined as

$$P_d N_d (\tau - \tau_0) + P_t N_t (\tau - \tau_0) = \tau^* , \qquad \text{Equation 31}$$

where P_d and P_t are respective probabilities of dislocation pile-up against grain and twin boundaries, and can be approximated as (1-*t/d*) and *t/d* respectively. Numerous MD simulations have shown, however, that TBs are comparable to grain boundaries in terms of resistance to dislocation transmission [24-25, 66, 143]. Meanwhile, assuming that dislocation separation distance is similar when piling-up against grain and twin boundaries, then N_t, the number of dislocations piling-up against twin boundaries, can be estimated as $N_d t/d$. By combining Equations 30 and 31, one arrives at

$$\tau = \tau_0 + \left\{ \frac{Gb\tau^*}{\pi(1-\nu)d\left[1 - \frac{t}{d} + \left(\frac{t}{d}\right)^2\right]} \right\}^{1/2} . \qquad \text{Equation 32}$$

Comparing Equations 30 and 32 shows that

$$L_{eff} = d\left[1 - \frac{t}{d} + \left(\frac{t}{d}\right)^2\right] . \qquad \text{Equation 33}$$

Notice if twin boundaries are absent or when $t = d$, L_{eff} reduces to *d*, and the traditional Hall-Petch relation is recovered. Also, this equation applies when the twin volume fraction is identical or at least comparable to that of matrix. Figure 33 shows that by using L_{eff}, hardness of annealed nt Ag follows literature data (where d is the dominating dimension) very well.

The (110) Ag films have been analyzed differently from the (111) films, due to their different microstructure. The microstructure is more isotropic than in (111) films because twin boundaries and slip planes are more evenly distributed throughout the film. Hence, the structure is more similar to a polycrystalline metal than the lamellar structure of the (111) nt Ag films, and measured twin thickness more accurately reflects true average barrier spacing. Figure 33 is a Hall-Petch type plot for the (110) films, and feature size used here is a volume-weighted average of the twin and matrix spacing. With these parameters, hardness falls much closer to what is expected given the literature data, but still somewhat softer than expected value. A recent study shows that material response is affected by not only mean grain size, but also by grain size distribution [163]. In nc Ni with similar mean grain size of ~20 nm, increasing variance in the grain size distribution resulted in a drop in ultimate tensile strength exceeding 20%. Twin and matrix thickness were both broadly distributed in the (110) Ag (Figure 28), suggesting that strength may fall substantially below what is predicted by t_{twin}.

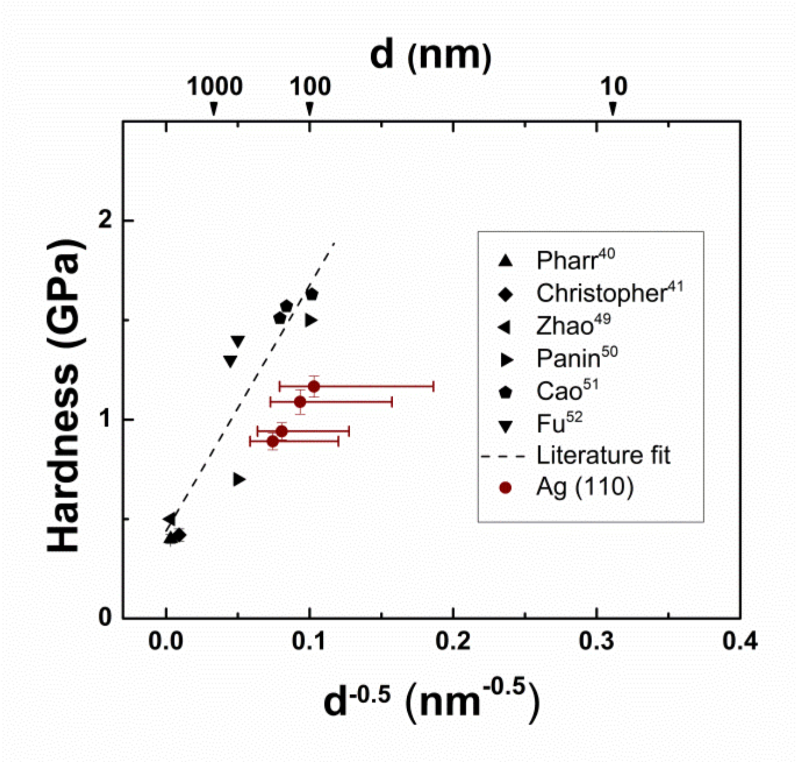

Figure 33: Hall-Petch plot using indentation hardness of (110) Ag films using the volume weighted average of the twin thickness. The hardness values of all films fall close to the fitted line from the literature.

When these are considered, the data falls close to the fitted literature Hall-Petch slope. This suggests that the broad distribution associated with the mean thickness causes large domains to dominate strengthening behavior.

IV.6 Conclusions

Microstructures of epitaxial nt (111) and (110) Ag films show significantly different thermal stability during annealing. Twin thickness increased very slowly in (111) films until thermal diffusion processes were activated, and even then average twin thickness remained below 100 nm. Additionally, in (111) Ag films the twinned volume fraction remained unchanged, at ~ 50%, while in (110) films twins were quickly removed during annealing.

This orientation dependence provides an important mechanism for preserving nanotwins at high temperature. Indentation hardness fell in both films, but more dramatically in (111) films. Both films showed similar hardness after annealing to 800 °C. Large domains in (111) films had a strong effect on hardness, and an effective feature size accurately returns the data to the Hall-Petch slope. The (110) films have a less regular structure, and hardness can be returned to the Hall-Petch slope by considering a volume-weighted average of twin and matrix thicknesses, as well as larger domain sizes.

CHAPTER V

FORMATION MECHANISMS OF HIGH-DENSITY GROWTH TWINS IN ALUMINUM WITH HIGH STACKING FAULT ENERGY[*]

V.1 Overview

Nanotwins readily form in numerous fcc metals with low stacking fault energy (γ_{sf}). However, growth twins rarely form in Al due to its high γ_{sf}, ~120 - 165 mJ/m^2. Here, by using thin inter- or buffer layers of a low γ_{sf} fcc metal (Ag), we overcome the γ_{sf} barrier and successfully grow high-density coherent and incoherent twin boundaries into Al. We identify three mechanisms that enable growth twin formation in Al, and demonstrate enhanced mechanical strength in twinned Al. This study reveals an effective means that may be generalized to control growth twin formation in fcc metals with high γ_{sf}.

---

[*] This chapter is reprinted with permission from "Formation Mechanisms of High-Density Growth Twins in Aluminum with High Stacking Fault Energy" by D. Bufford, Y. Liu, Y. Zhu, Z. Bi, Q.X. Jia, H. Wang, and X. Zhang, 2013. *Materials Research Letters*, Volume 1, Issue 1, pp 51-60, Copyright 2013 by D. Bufford, Y. Liu, Y. Zhu, Z. Bi, Q. X. Jia, H. Wang and X. Zhang.

V.2 Introduction

Since the initial synthesis of high-density growth twins in Cu [30, 164] and 330 stainless steel films [24, 51], extensive studies have investigated the mechanical and physical properties of nanotwinned (nt) face-centered-cubic (fcc) metals. The Σ3 {111} coherent twin boundary (CTB) in nt metals provides resistance to dislocation transmission similar to high-angle grain boundaries [25-26, 48], and dense twins lead to high strength, higher strain rate sensitivity [26, 57], and enhanced work hardening rate [164-167] in comparison to their bulk non-twinned counterparts. CTBs have a symmetrical structure and low energy configuration [13], so nt metals have better fatigue resistance [55, 142], thermal stability, electrical conductivity, and ductility than nanocrystalline (nc) metals with similar strength [32-33, 57, 64, 67].

Most previously studied nt metals have low γ_{sf}, and hence readily form growth twins during synthesis [30, 33, 51, 80, 168]. We recently characterized magnetron sputtered Ag films on Si (111) substrates via cross sectional and plan-view TEM [80]. Ag has the lowest γ_{sf} among monolithic fcc metals, so during deposition the films formed epitaxial nt microstructures with high-density CTBs oriented perpendicular to the growth direction. However, the probability of twin formation during deposition rapidly diminishes with increasing γ_{sf}, as twin boundaries become more and more unstable energetically [51]. High γ_{sf} thus becomes a fundamental barrier to the formation of high-density growth twins in numerous fcc metals.

Al is one such metal in which twins rarely form due to its high γ_{sf}, hence twins in Al are associated only with specific conditions. Molecular dynamics simulations predicted deformation twinning and twin boundary migration in nc Al [39-40, 42]. Deformation twins appeared in highly strained regions at the tip of an indented area and in nc Al powders subjected to high strain rate cryomilling [74, 76]. Additionally, the stress concentration near a crack tip can lead to deformation twinning in Al, and these twins reverse as the stress relaxes [75]. Under these extreme conditions (large stress concentration, high strain rate, and low temperature), deformation twins occasionally form in Al to assist dislocation slip and accommodate plastic deformation. Various models have been developed to explain the generation of partial dislocations and twins in nc Al [39-40, 42, 169-171], and recent reviews provide detailed information about deformation twinning processes in various metals [78-79]. In spite of the generation of *deformation* twins in Al, the introduction of high-density *growth* twins into Al remains a major scientific challenge.

In this paper, we demonstrate growth of high-density twins and stacking faults in Al films for the first time by using a template method. Methods employing template or buffer layers have been known for some time in the study of epitaxial semiconductor thin films [95, 172], but have not been used for fabricating nt metals. Here we incorporate thin inter-layers or a buffer layer of a low γ_{sf} fcc metal (Ag), so that coherent Ag/Al interfaces allow replication of twins and stacking faults from Ag into Al. We present three mechanisms through which twins may form in Al, and show enhanced mechanical strength in these nt Al films. This template approach may be generalized to form high-density twins in numerous other fcc metals with high γ_{sf}.

V.3. Experimental

All films were deposited at room temperature using DC magnetron sputtering. Single crystal silicon substrates with (111) orientation were etched with HF prior to deposition to remove the native oxide layer. The base pressure prior to deposition was typically 5-9 × 10^{-8} torr, and Ar gas (99.99%) pressure during sputtering was ~3.6 × 10^{-3} torr. Pure Al (99.99% or better) and Ag (99.99%) targets were used. Single layer Al films were deposited directly onto etched Si substrates to a thickness of 2 μm. For all Ag/Al multilayer films a 100 nm Ag seed layer was deposited first to ensure epitaxial growth. Next, alternating Ag and Al layers of different individual layer thickness, h, were deposited. Films with $h_{Ag}=h_{Al}=100$ nm, $h_{Ag}=h_{Al}=10$ nm, $h_{Ag}=5$ nm and $h_{Al}=100$ nm, and pure 1 μm Al, were grown on seed layers to a total film thickness of 1.5 μm. X-ray diffraction (XRD, PANalytical X'Pert PRO Materials Research Diffractometer, Cu Kα radiation) was used to examine film quality. Both out-of-plane θ-2θ and in-plane phi scans were conducted. XRD and transmission electron microscopy (TEM) experiments were performed immediately after deposition. Cross-section TEM specimens were prepared by mechanical grinding and polishing, followed by low energy ion milling, taking cautions to avoid heating during preparation. Specimens were examined along Al [011] zone axes with an FEI Tecnai F20 ST electron microscope operated at 200kV. Additional high-angle annular dark field scanning transmission electron microscopy (HAADF-STEM) was performed at the National Center for Electron Microscopy (Lawrence Berkeley National Laboratory) using the aberration corrected TEAM 0.5 microscope, an FEI Titan electron microscope enhanced by an advanced STEM corrector. Operating at 300kV, the microscope can form electron probes as small as 0.5 Å, yielding directly interpretable information about the local chemistry of columns of atoms in the sample [173]. Hardness was measured via an instrumented nanoindentation method performed using a Fischerscope HM2000XYp micro-/nano-indenter with a Vickers indenter tip. Hardness vs. depth analysis was performed, and a hardness plateau (i.e. proper depth to avoid erroneous hardening influences of both small indentation size and substrate effects) was typically observed. A minimum of 9-12 good indentations were performed at each indentation depth.

V.4 Results

The single layer Al films grown directly on Si (111) substrates at a relatively high deposition rate were epitaxial with {111} orientation, and developed only a miniscule amount of twinned variant, as evidenced by the XRD phi-scan from the film {111} planes (Figure 34a). Multilayer Ag/Al films on Si (111) substrates, however, behaved much differently. The phi-scan from the Ag 5nm / Al 100nm epitaxial multilayer film clearly reveals two sets of peaks, each with three-fold symmetry, corresponding to respective matrix and twin variants. The phi-scan from the 1μm thick epitaxial Al film on a 100 nm Ag seed layer (referred to as Al 1000 nm / Ag seed layer hereafter) also shows two sets of peaks, arising from the matrix and twin variants. As seen in XRD θ-2θ profiles (Figure 34b), the single layer and multilayer samples were all epitaxial {111} textured films on Si (111), hence matrix and twin variants comprise the entirety of the films.

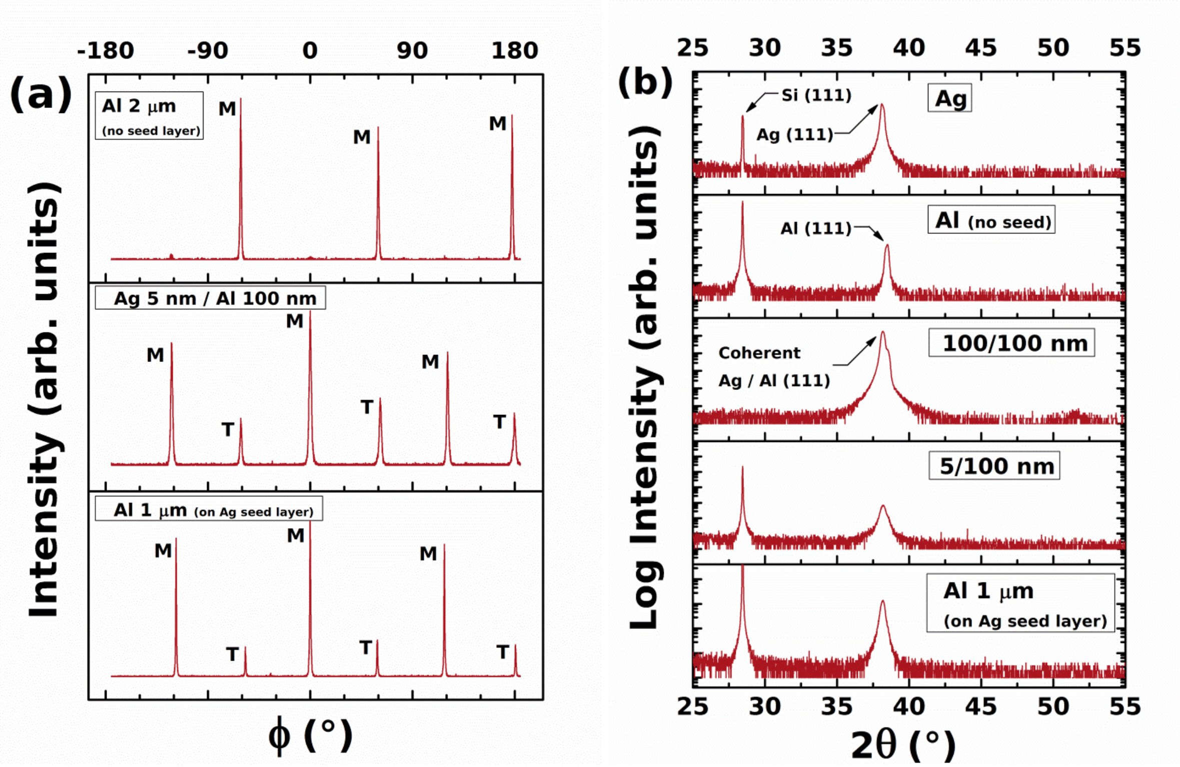

Figure 34: (a) XRD {111} phi-scan profiles of epitaxial films. In the pure epitaxial Al film (no Ag seed layer), a single matrix variant (denoted M) with three-fold symmetry dominates. In the Ag 5 nm / Al 100nm epitaxial multilayer specimen, three twin peaks (denoted T) arise from the greatly increased volume fraction of twin variant, and coexist with the three matrix peaks. In the epitaxial Al 1 μm / Ag seed film, the twin variant peaks are smaller than in the multilayer sample, but still indicate a significant twinned fraction. (b) Conventional 2θ XRD profiles plotted with log intensity to enhance any small peaks. The only peaks present correspond to the Si substrate or Ag and Al (111) planes, indicating epitaxial film structure.

There is no evidence of AgAl intermetallic compounds in the XRD profiles. HAADF-STEM micrographs collected from Ag 10 nm / Al 10 nm multilayer film specimens (Figure 35a) revealed minimal intermixing even at such small *h*. (Note that the Al layer is dark, as contrast is proportional to $Z^{1.7}$ (where Z is atomic number) [174]. The remainder of this paper focuses on Al films with much larger *h*, where any contribution of intermixing to twin formation diminishes even further.

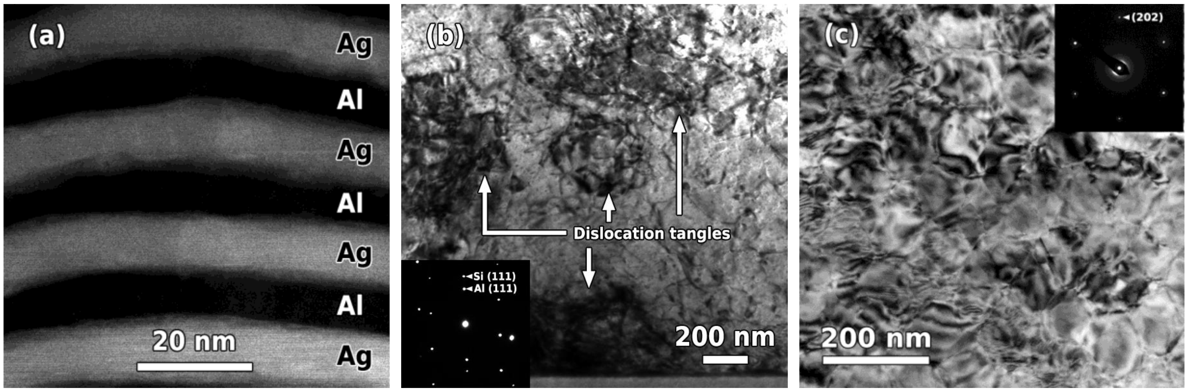

Figure 35: (a) A cross-sectional HAADF-STEM micrograph of an epitaxial Ag 10 nm / Al 10 nm film shows lack of intermixing. (b) Bright-field cross-sectional TEM micrograph ([011] Al zone axis) showing the epitaxial Al (111) film grown directly on the Si (111) substrate (without Ag seed layer). The inset SAD pattern was taken with a large aperture, and shows only the Si substrate and a single epitaxial Al variant. Large clusters of dislocation tangles dominate the microstructure. (c) Plan-view TEM micrograph of an epitaxial nt pure Ag film on Si (111) showing domain structure. The inset SAD pattern confirms the epitaxial structure.

TEM examinations of single layer epitaxial Al films on Si (without Ag seed layer, Figure 35b) revealed an epitaxial structure with dense dislocation tangles. As suggested by XRD profiles, essentially all of the Al film consisted of a single crystal-like epitaxial variant, i.e., nearly no twins formed. We observed a few small stacking faults on various {111} planes, and a scarcity of small twin variants appeared at the film-substrate interface. These variants were exceedingly rare, and extended just a few nm into the film. TEM examination of epitaxial Ag/Al multilayer films revealed high-density twins and stacking faults within Ag layers, as expected. In epitaxial Ag 100 nm / Al 100 nm films (Figure 36a), layers appeared wavy due to island growth mechanisms and residual growth stresses. Strikingly, many ITBs stretched nearly vertically across several Ag and Al layers. The inset selected area diffraction (SAD) pattern taken from a large area confirms an epitaxial multilayer film structure with high-density CTBs and abundant ITBs.

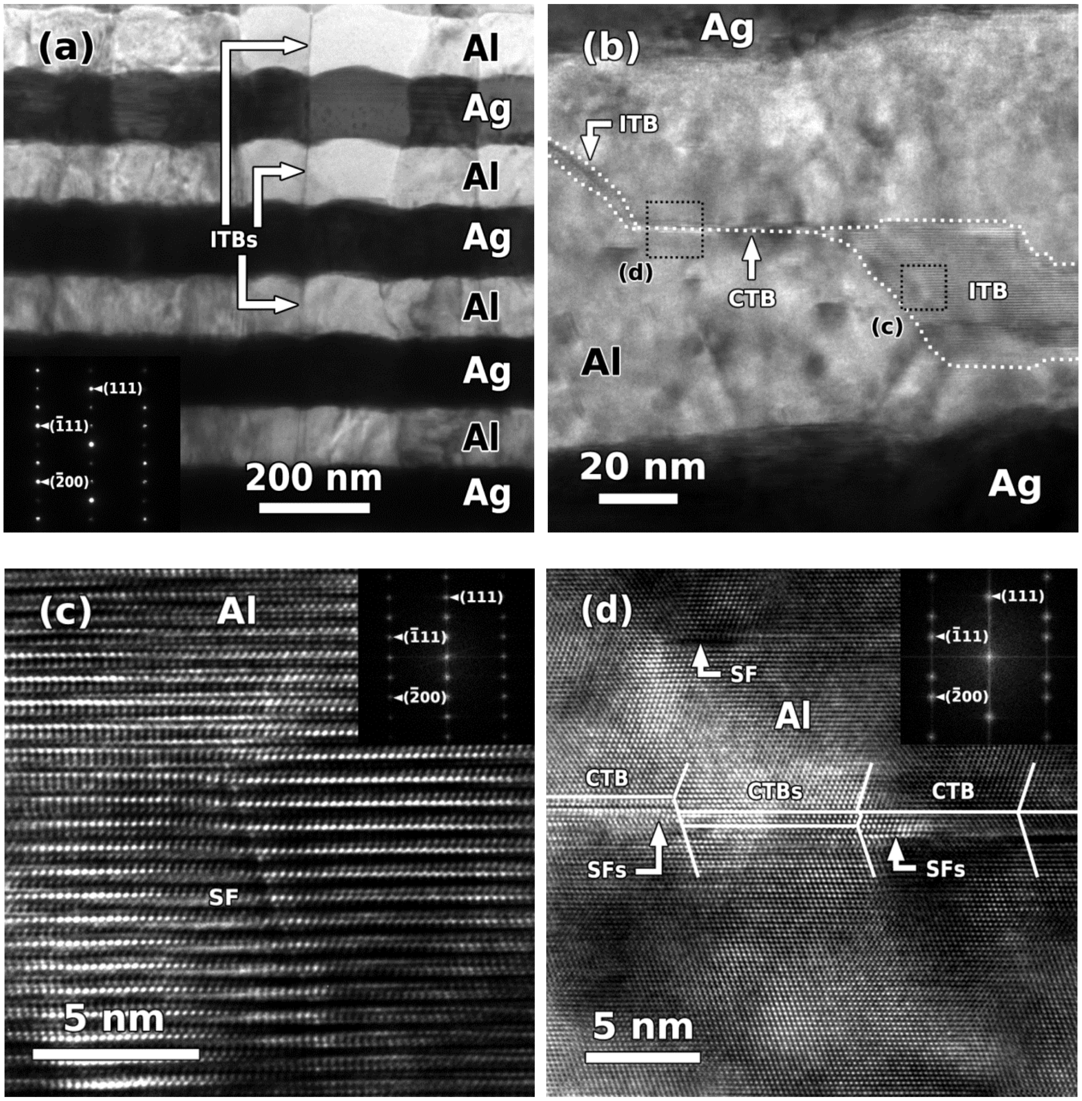

Figure 36: Bright-field cross-sectional TEM micrographs (Al [011] zone axis) from the Ag 100 nm / Al 100 nm epitaxial multilayer film. (a) At low magnification, ITBs can be seen passing through several layers, and the SAD pattern from the film alone reveals evidence of both ITBs and CTBs. (b) A higher magnification view shows a twin boundary with mixed ITB and CTB components in Al. (c) The HRTEM micrograph shows a magnified view of box (c) in Figure 36b. Here, a large ITB has a stacking fault inside, and the inset FFT confirms the ITB structure. (d) A magnified view of box (d) shows stacking faults leading to a number of atomic steps along a CTB. The inset FFT confirms the formation of CTB structure.

Figure 36b shows a typical example wherein groups of ITBs in Al connect CTBs with lengths of over tens of nm. Some ITBs also have widths exceeding 100 nm (Figure 36b). The high resolution TEM (HRTEM) micrograph in Figure 36c shows a wide ITB (confirmed by the inset fast Fourier transform (FFT)), the structure of which can also be considered as a 9R phase, similar to those observed previously in low γ_{sf} metals, such as Cu, Ag, and Au [14-15, 19]. ITBs in epitaxial nt Cu and Ag typically align vertically (parallel to the growth direction) [67, 80]. However, many ITBs in Al form a twin boundary structure in which CTB and ITB units combine to form meandering boundaries, a structure previously observed in Au and termed the chain unit model [21]. Meanwhile, many longer CTB segments were not confined to a single {111} plane. Closer examination (Figure 36d) revealed that CTBs are comprised of atomic steps due to numerous adjacent stacking faults.

These observations show that 100 nm thick Ag layers sufficed to induce abundant twins in Al. To investigate whether thinner Ag layers might produce a similar microstructure, we examined epitaxial Ag 5 nm / Al 100 nm multilayer films. As shown in Figure 37a, indeed, thinner Ag layers still induced twins in Al, with structures similar to those observed in Ag 100 nm / Al 100 nm films. Again, many ITBs extended through multiple Ag and Al layers. The inset SAD pattern confirms the formation of high-density twins, and shows no components other than the matrix and twins. Figure 37b shows a typical ITB nucleating at the Ag/Al interface and propagating into the Al layer. The ITB extended through the Al layer by intermingled CTB and ITB segments, and eventually terminated at the upper Ag/Al interface. The HRTEM micrograph in Figure 37c presents an atomic-resolution view of a

CTB decorated by an adjacent SF, and a mixed TB consisting of zigzag steps of CTBs and ITBs.

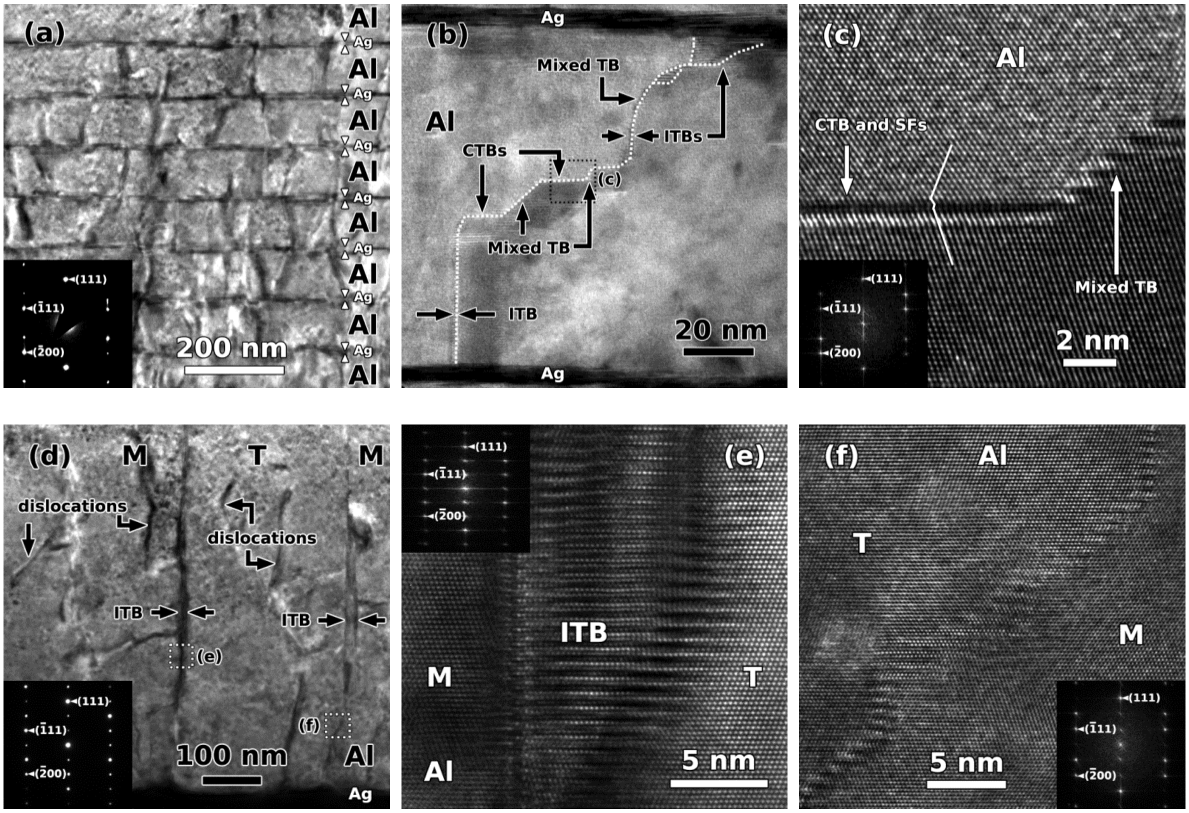

Figure 37: Bright-field cross-sectional TEM micrographs (Al [011] zone axis). (a) In the Ag 5 nm / Al 100 nm epitaxial multilayer film at low magnification, a relatively smooth layer structure is evident, and the SAD pattern from the film alone reveals evidence of twinning. (b) A higher magnification view shows a single meandering twin boundary consisting of ITB and CTB segments nucleated at the lower Ag/Al layer interface and extending through the Al layer. (c) An HRTEM micrograph of box (c) in 4b shows a CTB joined to a mixed twin boundary, which contains zigzag steps of ITBs and CTBs. The inset FFT confirms the twinned structure. (d) At low magnification in the epitaxial Al 1000 nm / Ag seed film, the domain structure defined by the ITBs is evident, with the twin and matrix variants denoted T and M. Several long threading dislocations are visible, and the inset SAD pattern from the Al film alone reveals evidence of prominent ITBs. The boxes (e) and (f) correspond to the magnified views of (e) a thick vertical ITB segment and (f) a narrower meandering twin boundary.

In both multilayer films, the majority of twins extended all the way through the Al layers, and propagated horizontally by ~50 nm. Since only one twin boundary usually extended through one layer in a given area, the average twin thickness in Al layers was approximately *h*/2. Twins that did not extend through the entire Al layer typically terminated within 10-20 nm of the interface.

The epitaxial Al 1000 nm / Ag seed layer film revealed how far twin boundaries might grow into Al. While high-density twins still formed, the microstructure differed substantially from the aforementioned multilayer films. Adjacent twin variants extended hundreds of nanometers into Al along the growth direction, resulting in a columnar structure with long ITBs separating adjacent domains (Figure 37d). Average columnar width was ~200 nm. ITBs of various widths were predominant in these films (Figure 37e), although some mixed ITB/CTB segments were still present, as shown by the HRTEM micrograph in Figure 37f.

V.5 Discussion

V.5.1 Twin boundary formation mechanisms in Al

Controlled formation of stable growth twins and stacking faults has not been previously accomplished in Al. A thermodynamic model predicts that twin formation probability during vapor deposition depends on the difference in critical radius of formation between a defect-free and twinned nucleus [51], which in turn depends on numerous parameters, most notably deposition flux and γ_{sf}. Increasing deposition rate effectively 'freezes' defects in place by piling up more material before atoms can diffuse to their ideal crystallographic sites, and hence introduces more growth defects, such as twins.

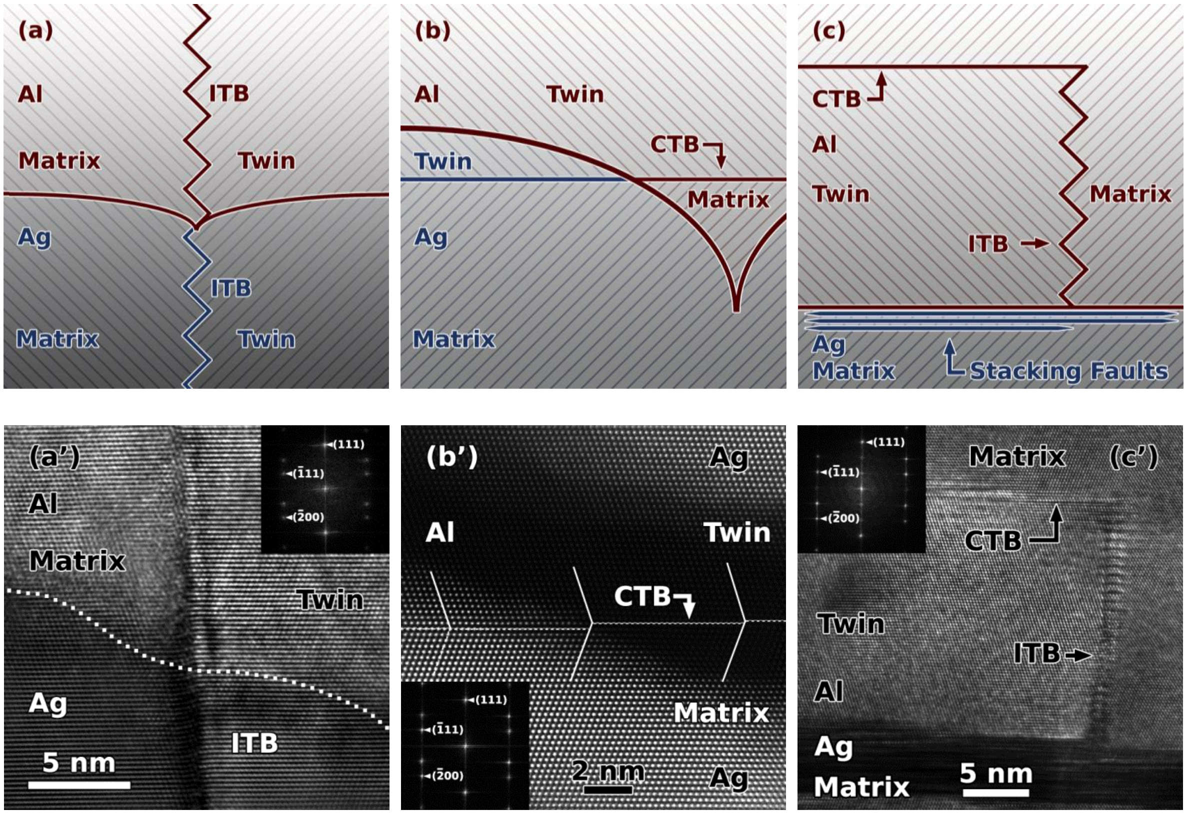

Figure 38: Illustrations of observed twin replication mechanisms at the Ag/Al interface. (a) Epitaxial growth forces Al to replicate the microstructure of twinned Ag, causing an ITB to propagate vertically through Al. The corresponding HRTEM micrograph (a') confirms the formation of twins in Al via this mechanism, with the dotted line delineating the coherent interface. (b) Coherent interfaces allow a CTB in Ag to extend laterally into Al. (b') The HAADF-STEM micrograph (from the Ag 10 nm / Al 10 nm multilayer film) shows lateral propagation of a CTB from Ag into Al. In this micrograph Al appears darker as contrast is proportional to atomic number. The same micrograph also shows that Ag contamination is essentially nonexistent around the CTB, hence intermixing does not play a role in the twin formation and stabilization processes in Al. The schematic (c) and corresponding HRTEM micrograph (c') illustrate ITBs nucleating from high density SFs at the Ag/Al interface. Note that the ITB deviates leftward after propagating ~ 20 nm, forming a CTB.

However, for metals like Al, γ_{sf} is so high that increasing deposition rate alone is insufficient to nucleate twins within the film during growth. The scarce few twins observed at the Al/Si interface in single layer epitaxial Al films on Si (without Ag seed layer) suggested that growth twins may form in Al near interfaces. Ag was chosen for inter- and buffer layers because it grows coherently with Al due to a small lattice mismatch (<1%). Furthermore, our previous studies, including plan-view and cross-sectional TEM show that nt Ag can grow epitaxially on Si, while readily forming high-density growth twins [80]. Hence, Ag layers act as templates, whereby twins nucleate in Ag or at the interface, and then extend into Al.

We identified three mechanisms by which twin boundaries form in Al. Schematics in Figure 38a-c illustrate these mechanisms, and the corresponding TEM micrographs, Figure 38a'-c', provide experimentally observed evidence for each mechanism. In mechanism (1), shown schematically in Figure 38a, domains in epitaxial Ag layers assume only two possible orientations, twin or matrix, between which ITBs form. Al grows epitaxially on Ag, and thus the orientations of Ag domains and ITBs are replicated by the Al layer, as observed in the HRTEM micrograph in Figure 38a'. Therefore, mechanism (1) enables formation of abundant vertical ITBs in Al. The waviness seen in the layers may be related to the formation of adjacent domains. Waviness was most notable in the Ag 100nm/Al 100nm films (Figure 36a), and a significant number of vertical ITBs emanated from the valley of such waves. In some areas nearly ~50% of the valleys had corresponding ITBs, while other areas had only ~15%. Additionally, once a vertically propagating ITB formed, it often extended through many Al and Ag layers (Figure 36a). However, vertically propagating ITBs appeared elsewhere away from the valleys, and the same propagation mechanism appeared to be active in the Ag 5 nm / Al 100 nm films, where little waviness was observed (Figure 37a).

In mechanism (2), CTBs are replicated laterally from Ag into Al, as illustrated in Figure 38b. Should CTBs terminate at the layer interface, ITBs would have to nucleate inside Al to join the variants, consequently increasing the total system energy. Hence, propagation of CTBs across the layer interface into Al is more energetically favorable than termination. The HAADF-STEM micrograph in Figure 38b' provides an example of this mechanism.

Mechanism (3) shows that twin variants may form in Al even if the underlying Ag consists of a single variant, as shown in Figure 38c. The HRTEM micrograph in Figure 38c' reveals a narrow ITB nucleated from dense stacking faults at the Ag/Al interface. In this mechanism, jumbles of stacking faults in Ag result in similar jumbles in Al near the interface, and ITBs may nucleate from these high-density stacking faults. This mechanism requires only a few atomic layers of stacking faults to initiate ITB nucleation in Al. Coherency is probably necessary here as it allows Al to replicate the microstructure of stacking faults in Ag, and eventually trigger the nucleation of ITBs that propagate vertically into Al. Each of these mechanisms was observed experimentally, however, there still may be other as-yet unidentified mechanisms through which a template (buffer) layer enables twin formation in Al. The preferred propagation mechanism appears to be influenced by the local stress state. For instance, in some areas, the three mechanisms appeared with essentially equal frequency, while in others a single mechanism, typically (1), accounted for nearly 100% of twins in Al. The XRD phi-scans (Figure 34a) indicate a greater prevalence of the matrix variant than the twin variant; approximately 2/3 of the film is matrix in the multilayer films, while 3/4 is matrix in the Al 1000 nm / Ag seed films.

We note that the Ag/Al system is ideal for defect propagation from layer to layer. The lattice mismatch of < 1% ensures that each Ag/Al interface is a nearly perfect Σ1 boundary; identical crystallographic indices are parallel in both under- and overlayers, and there is no need for misfit dislocations, domain matching, or a change in crystallographic orientation to allow epitaxial growth. Hence, Al overlayers replicate Ag underlayers almost exactly, including both twin variant orientation and twin boundaries. This relationship is clearly highlighted in HRTEM micrographs in Figures 38a' and 38b', where atomic planes are continuous across layer interfaces, and the inset SAD patterns indicate bicrystal structures (due to twins) without any tilt, rotation, or misorientation between the layers. Given a [111] growth direction, the matrix and twin variants are related by a 180° rotation about the growth axis, so that the (111) plane is the twinning plane. While theoretically twins may form on other {111} planes, we did not observe such twins, which is similar to our previous observations of twins in pure Ag films [80]. There is no evidence of variants other than the single matrix and twin variants described here.

While mechanisms (1) and (2) are conceptually straightforward, the formation of stacking faults and twins in case (3) requires further explanation. During island growth an interface traction arises between the island and the substrate. This traction is a shear stress whose magnitude depends on the distance from the island edge. We consider the growth of an island with z parallel to the growth direction and x perpendicular (Figure 39), so the shear stress, $\tau(x)$, can be expressed as [93]

$$\tau(x) \sim \sigma_m \sqrt{\frac{kh_f}{2\pi x}} . \qquad \text{Equation 34}$$

asymptotically as $x/h_f \to 0^+$.

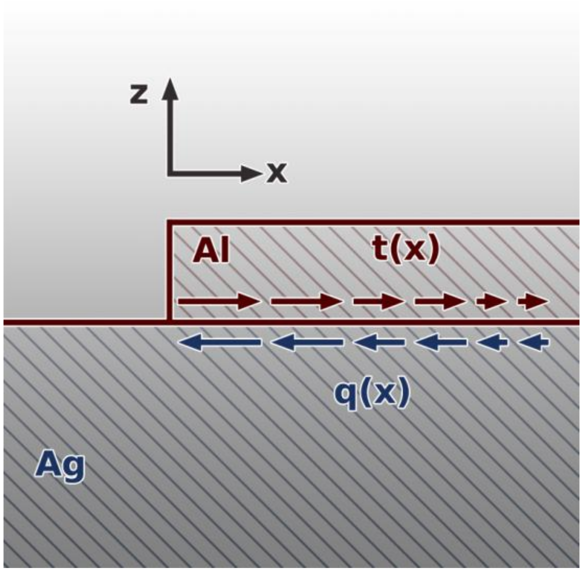

Figure 39: Schematic of shear stress development at the edge of an Al island grown on Ag during deposition. Stress transfer occurs via shear stress between Ag and Al near the free edge. Original concept developed by Freund, L. B. & Suresh, S. [93].

Here σ_m is biaxial mismatch stress between the film and substrate (defined as $\sigma_m = \varepsilon_{\max} E_f /(1-\nu_f)$), ε_{max} is mismatch strain between Ag and Al, h_f is film thickness, and x = 0 at the free edge of the island. Also, k is the plane strain elastic modulus ratio between substrate and film, computed by

$$k = \frac{\dfrac{E_s}{1-\nu_s^2}}{\dfrac{E_f}{1-\nu_f^2}}, \qquad \text{Equation 35}$$

where E_s, ν_s, E_f, and ν_f are elastic modulus and Poisson's ratios of the substrate and film, respectively. The magnitude of $\tau(x)$ increases with proximity to the free edge, or with increasing film thickness. Considering an Al film and Ag substrate, $k \approx 1.2$. Mismatch stress is approximately 1.1 GPa, as mismatch strain, ε_{max}, between Al and Ag is ~1%. Therefore, we estimate $\tau(x)$ of 470-1140 MPa when h_f/x is 1-6, i.e., near the island edge.

The growing Al layer must somehow accommodate these significant stresses. The shear stresses needed to nucleate full and partial dislocations, as well as those needed to either erase or extend the leading partial depend on grain size. By comparing these critical stresses, it has been determined that for Al twinning is favored when grain size, d, is ~ 6 nm or smaller [175-176], which is consistent with the size of islands nucleated during growth. This analysis gives a critical shear stress, τ_c, of ~ 0.9 GPa required for partial nucleation, while ≤ 0.5 GPa is sufficient to enlarge an existing twin [175]. Other models and simulations [177-178] yielded comparable values for τ_c. Hence, the traction near the Al island edge provides sufficient stress to nucleate Shockley partial dislocations at the interface during deposition. We also note that mechanisms (1) and (3) only result in the formation of adjacent twin variants separated by ITBs. CTBs may form directly by mechanism (2), or serve as horizontal junctions between ITBs, as seen in Figure 38c'. Usually mixed ITB and CTB segments comprised most boundaries, resulting in meandering TB paths throughout Al, [19] as illustrated in Figures 36 - 37.

V.5.2 Stabilization of twin boundaries

Twin boundaries in high γ_{sf} metals can be stabilized in two ways: by reducing twin boundary energy or constraining the system such that the twinned state has the lowest possible energy. Numerous previous studies demonstrate that alloying can decrease γ_{sf}, thereby enhancing energetic stability of twin boundaries and stacking faults [81]. However, the mechanisms at work in our study differ from this well-established method.

An alternative way to stabilize twin boundaries is to use the epitaxial structure to ensure that only twin and matrix variants may exist. Epitaxial growth of Ag on Si results in the formation of one of only two possible variants, and epitaxial growth of Al on Ag causes the Al layer to take the same structure. Hence, only ITBs and CTBs separate domains in Al instead of more conventional high- or low-angle grain boundaries. Our study of the Cu/Ni system examined both incoherent and coherent multilayer films, and revealed that twins penetrated into Ni layers only when layer interfaces were coherent [92].

The relative abundance of ITBs in comparison to CTBs in Al may be related to the total grain boundary energy within the system. ITB energy in Al varies [19, 179] from 223-357 mJ/m^2, while the energy of its CTBs is ~75 mJ/m^2 [22]. In comparison, Cu has an ITB energy of ~550-714 mJ/m^2 and CTB energy of ~24-39 mJ/m^2, while Ag has corresponding energies of ~126 mJ/m^2 and ~8 mJ/m^2 [13, 22-23, 62]. The ITB/CTB energy ratios in Al, Ag, and Cu are ~3.5, ~16, and ~22, respectively. The smaller ratio in Al helps to explain the relative abundance of ITBs to CTBs in Al, whereas in Ag and Cu CTBs are predominant. ITBs in Al can be described equivalently by dislocation theory [20] or as a volume of 9R phase. Although the presence of ITBs (and hence at least some volume of 9R phase) is certain, as seen in Figures 36b-c and 37d-e, the actual volume of 9R phase is unclear. While some ITBs appear to have a very large volume (Figure 36b), there is a possibility that this is an artifact caused by a meandering boundary with a component running parallel to the foil plane. When projected onto a 2-dimensional surface, such a boundary may appear much wider than it actually is. One can postulate that some distortion of the projected image might occur under such conditions, which may explain the distorted appearance of the ITB in Figure 37e. However, some sizable boundaries (Figure 36c) do not appear to have such distortion, and may indeed be thicker slabs of 9R Al. Local stresses affect ITB width, and may cause the ITB to dissociate into a greater width [17, 145, 180], however, the typical width of a dissociated ITB is much smaller than the seemingly huge ITBs observed in this study. Future HRTEM analysis will reveal whether the ITBs observed in this study are the result of projecting typical ITBs onto a flat surface, or if the samples actually do contain large volumes of 9R phase.

V.5.3 Limits and applicability of the methodology for fabrication of bulk nt metals

In the Al 1000nm / Ag seed layer film, meandering ITB/CTB segments propagated through the entire film thickness, as seen in Figure 37d. We have synthesized other nt Al films, a few μm in thickness, where TBs formed via similar mechanisms. It is likely that the ITB/CTB segments could propagate through a film tens of μm in thickness. For multilayer films, new twins nucleate in each Ag layer, so the structure might be repeated essentially indefinitely. The mechanisms discussed here should be immediately applicable for fabrication of a variety of nt metals with high γ_{sf} in the form of coatings. However, sputtering techniques are limited to relatively thin (< 1 mm) coatings. Adaptation of the mechanisms discussed in this paper to other techniques may help to fabricate bulk nt metals for structural applications.

V.5.4 High strength Al enabled by twin boundaries

Nanoscale twins often contribute to improved mechanical strength, and strengthening indeed occurred in these nt Al films. Figure 40 shows indentation hardness data compiled from the literature [181-187], and includes only monolithic Al in the form of films and bulk specimens.

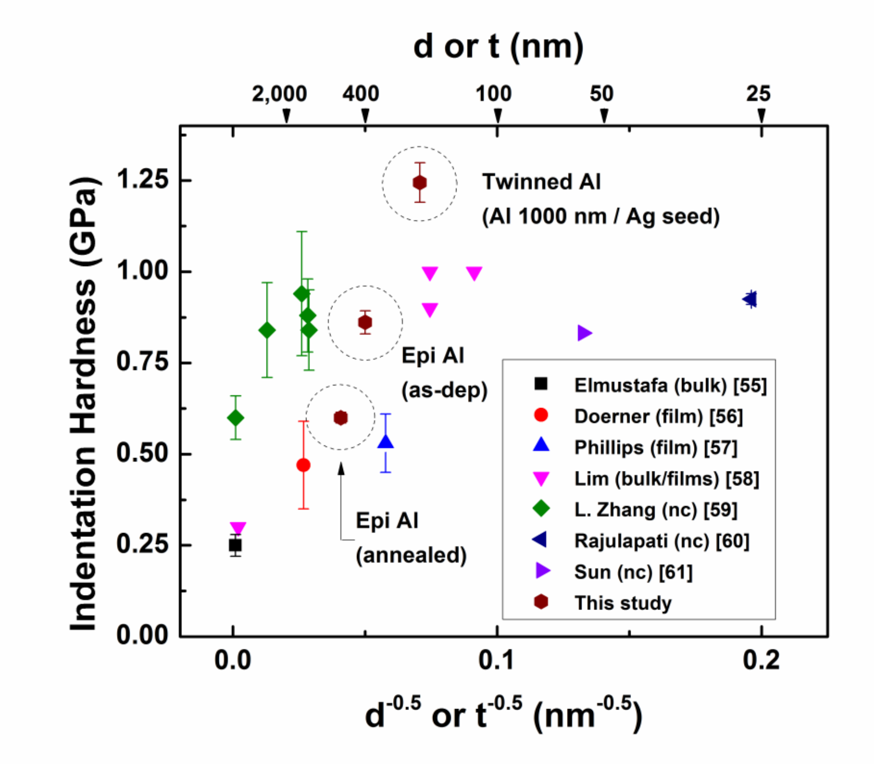

Figure 40: Nanoindentation hardness as a function of $d^{-0.5}$ or $t^{-0.5}$ (grain size and twin spacing, respectively) for Al from this study and other investigations of monolithic Al bulk and films, all with 99.99% or better purity. Our epitaxial (un-twinned) Al films fall, as expected, close to other Al materials with similar feature size, whereas twinned Al films fall among samples with the highest hardness. Error bars correspond to standard deviation arising from numerous hardness measurements.

Hardness of the as-deposited and annealed un-twinned single layer Al films falls in the expected range given by other studies (~0.6-0.8 GPa), whereas hardness of twinned epitaxial Al films reaches ~1.2 GPa. The nt Al films are approximately 50-100% harder than untwined Al films, and harder than nc Al with an average grain size of 20-50 nm [186-187]. Average spacing between ITBs in epitaxial nt Al films is ~200 nm, greater than the columnar grain size of Al films reported previously by Lim, *et al* [184], but the hardness is also greater. Increased strength in nt Al films likely reflects contributions from both ITBs and CTBs, as well as grown-in dislocations (Figure 37d), resulting in an effective barrier spacing smaller than the ~200 nm columns defined by the ITBs. A recent mechanistic model formulated to rationalize feature size-dependent strengthening caused by both grain and twin boundaries shows that contributions from both types of boundaries are important, especially if they are of similar length scales [143]. Furthermore, a substantial volume fraction of 9R phase (broad ITBs) may also enhance the strength of the Al films. Hardness of Ag 5 nm / Al 100 nm multilayer films approaches 2 GPa. However, in multilayer films ITBs, CTBs, and layer interfaces influence strength, and a full discussion of these mechanisms is beyond the scope of this paper [89, 188].

V.6 Conclusions

We show that high-density growth twins can be introduced into metals with high γ_{sf}, such as Al, with the assistance of coherent layer interfaces. Twins may extend from Ag into Al via three experimentally observed mechanisms. However, this is not meant to be an exhaustive collection of mechanisms by which twins may enter Al with the assistance of a seed layer. Coherent interfaces force epitaxial growth of Al into one of only two possible twin variants defined by the Ag underlayer. The template methods described here may provide a critical forward step towards creating nt structures in other high γ_{sf} metals. Abundant twins and stacking faults have exciting implications for improving mechanical properties in Al and many other metals with high γ_{sf}.

CHAPTER VI

NANOTWINS AND STACKING FAULT IN HIGH-STRENGTH EPITAXIAL SILVER/ALUMINUM MULTILAYER FILMS*

VI.1 Overview

Epitaxial Ag/Al multilayer films have high hardness (up to 5.5 GPa) in comparison to monolithic Ag and Al films (2 and 1 GPa). High-density nanotwins and stacking faults appear in both Ag and Al layers, and stacking fault density in Al increases sharply with decreasing individual layer thickness, h. Hardness increases monotonically with decreasing h, with no softening. In comparison, epitaxial Cu/Ni multilayers reach similar peak hardness when $h \approx 5$ nm, but soften at smaller h. High strength in Ag/Al films is primarily a result of layer interfaces, nanotwins, and stacking faults, which are strong barriers to dislocation transmission.

---

[*] This chapter reprinted with permission from "Nanotwins and Stacking Faults in High-Strength Epitaxial Ag/Al Multilayer Films" by D. Bufford, Z. Bi, Q.X. Jia, H. Wang, and X. Zhang, 2012. *Applied Physics Letters*, Volume 101, Issue 22, pp 223112-1 – 223112-5, Copyright 2012 by the American Institute of Physics.

VI.2 Introduction

Metallic multilayer films have received substantial attention for their high strength. The mechanical behavior of such films has been characterized in numerous systems with coherent or incoherent layer interfaces. Several dislocation-based models have been used to explain strengthening mechanisms in multilayer films, where the primary deformation mechanisms depend on individual layer thickness, h [3, 86-87]. For larger h (> 50 nm), dislocation pile-up at layer interfaces dominates deformation behavior, similar to classical grain boundary induced strengthening in polycrystalline metals. When h decreases to tens of nanometers, pile-up of dislocations becomes increasingly difficult, and a single dislocation based Orowan bowing model is frequently applied to describe strengthening. Since layer interfaces confine propagating dislocations at this length scale, this strengthening mechanism is often called the "confined layer slip" (CLS) mechanism. Further reducing h to several nm, multilayer films often achieve a maximum strength determined by dislocation source length [87], and by numerous factors that influence barrier strength of the interfaces, including Koehler stress [88], coherency stress [89], misfit dislocations [90], stacking fault energy (chemical) mismatch [91], and the ω interaction (related to slip system continuity) [89]. Softening may occur in fully coherent multilayer films at this length scale, as fully coherent layer interfaces may allow easier transmission of single dislocations than incoherent interfaces. However, other microstructure features may inhibit softening. For example, {111} textured Cu/Ni multilayer films with high-density growth twins show less softening than twin-free {100} textured films with similar h [92].

Nanotwinned (nt) microstructures have recently garnered significant attention due to their impressive contributions to mechanical strength [41]. Twin boundaries (TBs) act similarly to high-angle grain boundaries in terms of impeding dislocation transmission, allowing nt metals to reach strengths comparable to nanocrystalline (nc) metals with similar feature size [30]. Due to the highly coherent nature of twin boundaries, nt metals often show superior thermal stability and electrical conductivity in comparison to their nc counterparts [33, 140, 164]. Additionally, TBs are efficient sinks for dislocations, active sources for mobile partial dislocations [37, 52], and under stress, TBs can migrate rapidly, causing detwinning [29, 92]. Hence, TBs are vital to work hardening capability, strain rate sensitivity and ductility of nt metals. Although nt microstructures readily form during deposition in metals with low-to-medium stacking fault energy (γ_{sf}) [24, 30, 80], such as 330 stainless steel (10–20 mJ/m^2) [189], Ag (22 mJ/m^2) [22], and Cu (45 mJ/m^2) [23], it is still challenging to produce them in high γ_{sf} metals, such as Al (120 – 165 mJ/m^2) [40, 179]. We recently demonstrated a technique for introducing nanotwins into Al by using Ag as a seed layer [190]. Ag has a similar lattice parameter to Al, but much lower γ_{sf}. Coherent Σ3{111} and incoherent Σ3{112} twin boundaries (CTBs and ITBs) nucleated in an Ag seed layer can penetrate into Al via coherent interfaces, as can stacking faults (SFs). Twin boundaries in these Al films contributed to high mechanical strength [190]. Previous studies of Ag/Al multilayer films also reported high Vickers hardness at small h [191], however, the mechanisms behind this strengthening were not clearly identified. Furthermore, the microstructure characterization techniques employed in that study were limited to X-ray diffraction (XRD). In this study, we demonstrate increasing twin and SF density in Al with decreasing *h*. TBs, SFs and a large γ_{sf} mismatch between Ag and Al induce high indentation hardness in Ag/Al multilayer films, with an absence of softening at small *h*.

VI.3 Experimental

Epitaxial Ag/Al multilayer films with equal *h* varying from 1 to 100 nm were deposited onto single crystal Si (111) substrates via magnetron sputtering at room temperature from pure Al (≥ 99.99%) and Ag (99.99%) targets. Total film thickness was ~ 1.5 μm. Single crystal silicon substrates were etched with HF prior to deposition to remove the native oxide layer, and base pressure in the chamber was ~ 8×10^{-8} torr. Microstructures of deposited films were characterized by XRD using a PANalytical X'Pert PRO Materials Research Diffractometer (Cu Kα radiation) and transmission electron microscopy (TEM) on an FEI Tecnai F20 Super Twin microscope operated at 200 kV. Mechanical properties were investigated by an instrumented nanoindentation technique with a Fischerscope HM2000XYp micro-/nano-indenter with Vickers indenter tip. Experimental details of the nanoindentation technique were similar to those reported previously [80]. Heating was minimized during TEM sample preparation to minimize intermixing between Ag and Al.

VI.4 Results

Due to their small lattice mismatch (< 1 %), Ag and Al readily grow epitaxially on top of each other, even when *h* is greater than tens of nm. In XRD profiles, when $h \geq 25$ nm, only a single peak was observed, but at smaller layer thickness satellite peaks appear due to the formation of a superlattice structure, as shown in Figure 41.

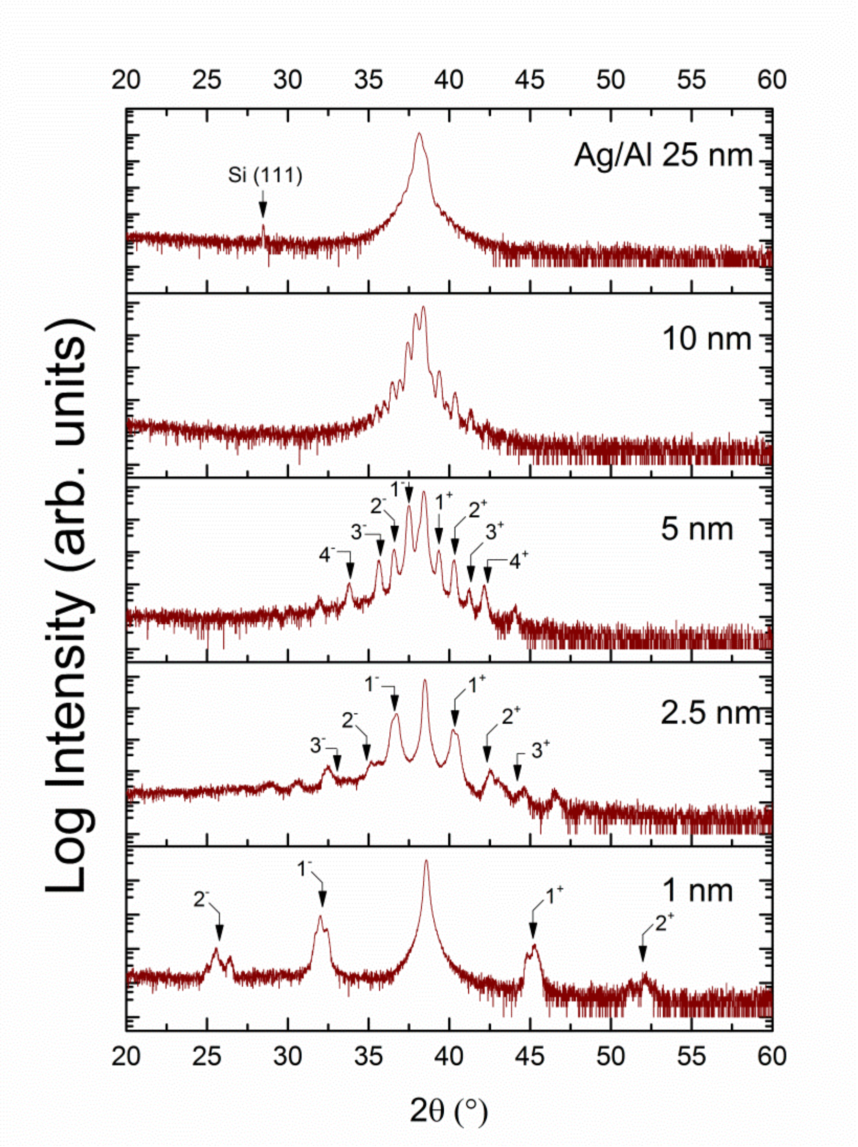

Figure 41: XRD profiles of Ag/Al multilayer films with varying *h* plotted with log intensity to enhance satellite peak visibility. No other film diffraction peaks were detectable outside of the 2θ range presented, indicating epitaxial character for all multilayer films. The lattice parameter mismatch between Ag and Al is < 1%, so when $h \geq 25$ nm only a single peak was present. As *h* decreased to ≤ 10 nm, satellite peaks of multiple orders began to appear. Calculated positions of several orders of satellite peaks are included for $h = 5$, 2.5, and 1 nm.

The position of satellite peaks can be described by

$$\frac{2\sin\theta}{\lambda_{xray}} = \bar{d}^{-1} \pm \frac{n}{\Lambda} \qquad \text{Equation 36}$$

where λ_{xray} is X-ray wavelength, $\bar{d}$ is average interplanar spacing, n is satellite peak order, and Λ is bilayer thickness (i.e. $\Lambda = 2h$) [192]. Peaks corresponding to Ag-Al intermetallic compounds were absent, indicating insignificant intermixing along layer interfaces.

Microstructures of the Ag/Al multilayer films were examined in detail via TEM. A cross-sectional TEM micrograph of the Ag 25 nm/Al 25 nm multilayer film (referred to as Ag/Al 25 nm hereafter) in Figure 42a shows numerous growth defects in Al. The inset selected area electron diffraction (SAD) pattern indicates an epitaxial interface with typical CTB diffraction pattern.

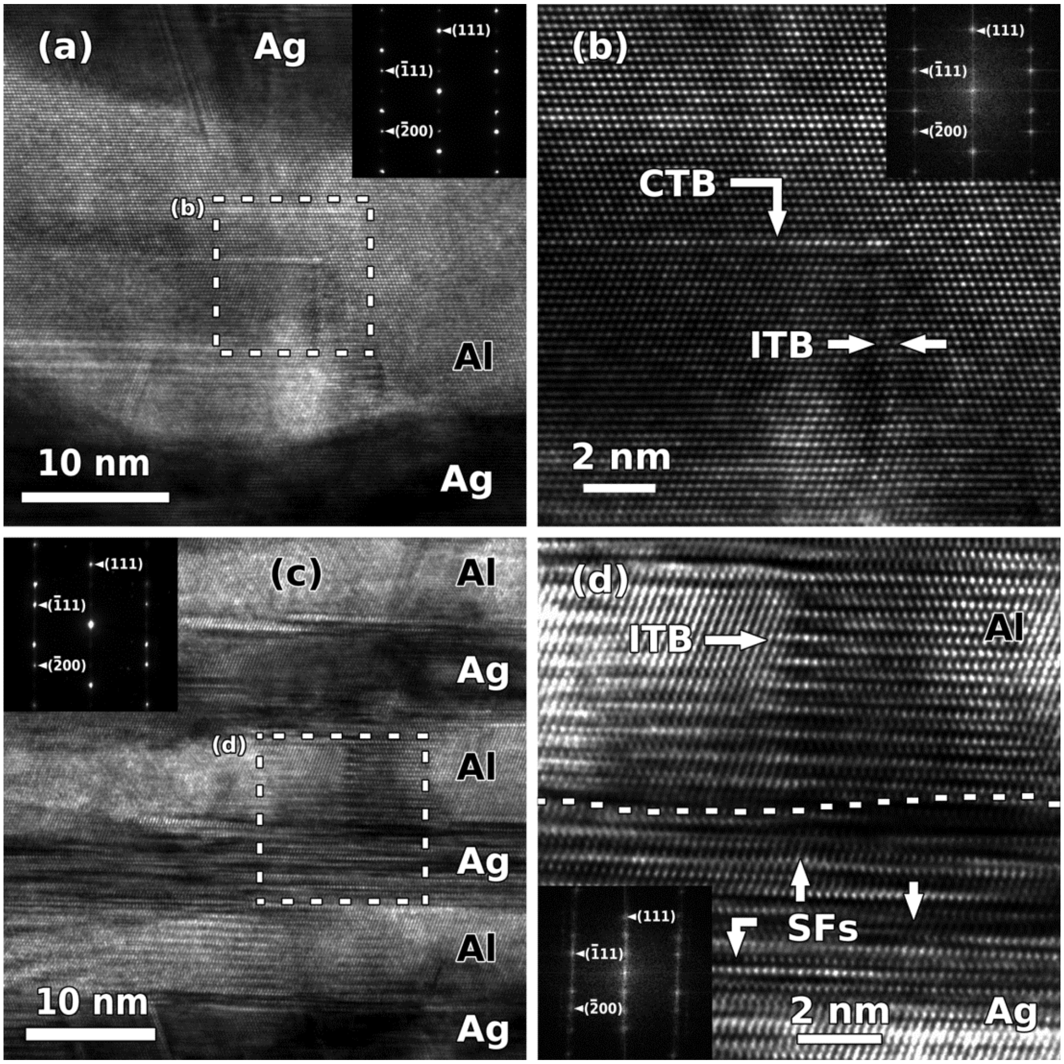

Figure 42: Bright-field cross section TEM micrographs examined along the film [011] zone axis. (a) The Ag/Al 25 nm multilayer film shows ITBs parallel to the growth direction. Abundant CTBs parallel to the substrate were observed in both the Al and Ag layers, but with a greater density of such defects present in Ag. The inset SAD pattern confirms the formation of a mixed ITB/CTB structure. (b) The dotted box in (a) is magnified, showing a long CTB and narrow ITB in Al. (c) The Ag/Al 10 nm multilayer film shows much greater SF density within the Al layers. The SAD pattern shows strong evidence of twins. Additionally it shows some faint streaks due to dense SFs, which appeared more frequently in Ag. (d) The dotted box in (c) is magnified, and the dashed line denotes the layer interface. SFs appear every few atomic planes in Ag. The Al layer shows a broad ITB, several nanometers in width, running through the thickness of the Al layer.

The high resolution TEM (HRTEM) micrograph of the dashed box in Figure 42b shows a CTB, tens of nm in length, and a sharp ITB, 5 nm in thickness, formed in Al. SF density in both Ag and Al layers increased with decreasing *h*, as shown in the Ag/Al 10 nm multilayer film in Figure 42c. In Al, CTB and SF density increased rapidly. The inset SAD pattern also shows an epitaxial twinned pattern, but the diffraction spots appear elongated with traces of streaks, indicating SF formation. The HRTEM micrograph in Figure 42d confirms the presence of high density SFs in both layers, and a broad ITB (several nm wide) in Al. As *h* decreased further, an increasing preference for CTBs and SFs over ITBs quickly developed. When *h* = 1 nm, CTBs and SFs dominated the microstructure, as shown in Figure 43a, with such growth defects occurring every few atomic layers.

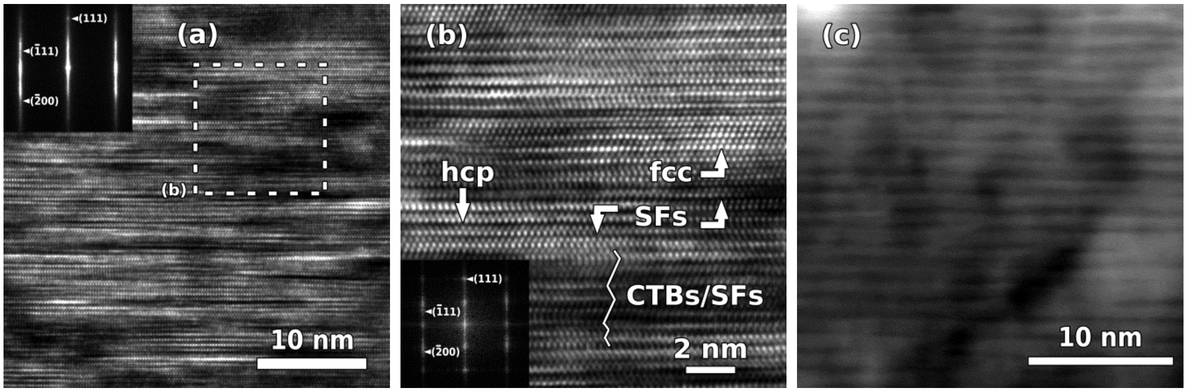

Figure 43: (a) Bright-field cross section TEM micrographs of the Ag/Al 1 nm multilayer film (along the film [011] zone axis). The film exhibits extremely dense twins and SFs, and the streaked SAD pattern confirms this densely faulted structure. (b) A magnified view of the dotted box in (a) shows dense SFs and CTBs occurring every few atomic layers, and a few planes with hcp stacking. Most of the film exhibited frequent stacking defects, although some volumes of fault-free fcc stacking were occasionally observed. (c) A high angle annular dark field scanning TEM (HAADF-STEM) micrograph confirms that the chemically modulated layer structure remained even when *h* = 1 nm.

The SAD pattern shows long streaks arising from these stacking defects. The HRTEM micrograph in Figure 43b shows abundant SFs, CTBs, and small volumes of hcp stacking, while defect-free volumes of fcc phase are scarce. At large *h* intermixing is minimal. The intermixed volume along layer interfaces is small even when *h* = 1 nm, as the chemically modulated Ag/Al layer structure is still clearly visible in STEM micrographs (Figure 43c).

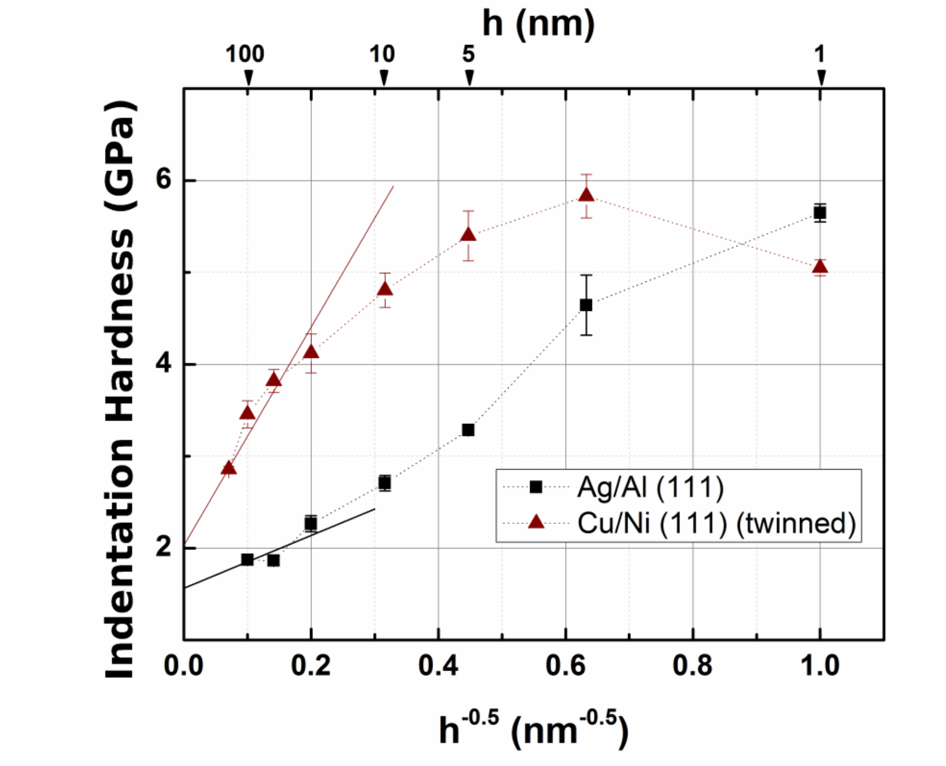

Figure 44: Comparison of indentation hardness as a function of $h^{-0.5}$ between epitaxial Ag/Al and Cu/Ni multilayer films with {111} texture. No softening occurred in Ag/Al at smaller *h*, in contrast to the (111) Cu/Ni system, where softening was observed after a peak hardness at *h* of 2.5 nm. In Ag/Al multilayer films hardness continually increased and reached a maximum (when *h* = 1 nm) comparable to the maximum hardness of Cu/Ni multilayer films.

Indentation hardness values from epitaxial nt Ag/Al multilayer films and {111} textured epitaxial nt Cu/Ni films [92] are compared as a function of $h^{-1/2}$ in Figure 44. For Ag/Al, hardness increased monotonically as *h* decreased from 100 to 1 nm, and maximum hardness was ~ 5.5 GPa. In the previously studied Cu/Ni system, hardness increased with decreasing layer thickness to a similar peak value, followed by softening at smaller *h*.

VI.5 Discussion

VI.5.1 Formation of high-density growth twins and SFs in Al

Although Ag readily forms twins during deformation, annealing, and physical vapor deposition [80], twins of any kind in Al are rare due to its high γ_{sf}. Deformation twins have only been observed in Al under extreme conditions (deformation at cryogenic temperatures or high strain rates) that inhibit conventional slip of full dislocations, and in areas with high local stress concentrations [39, 74-76]. In Ag/Al multilayer films, high density SFs and TBs frequently formed in Al during growth, and SFs dominated the microstructure as *h* decreased. The SF density in Al was unprecedentedly high when $h = 1$ nm, with an average stacking defect spacing smaller than 1 nm. A similarly densely twinned structure was previously observed in sputtered austenitic 330 stainless steel films [24].

Our recent work shows that epitaxial growth of Al on Ag allows Al overlayers to replicate ITBs and CTBs nucleated in the Ag seed layers [190]. Additionally, ITBs or dense SFs in Ag can promote SF nucleation in Al near interfaces, which may then evolve into ITBs in Al. These studies suggest two critical factors for growth defect formation in Al: low stacking fault energy in the seed layer and epitaxial growth of the overlayer on the seed layer.

VI.5.2 High strength of Ag/Al multilayer films

In the continuum dislocation pile-up regime ($h \geq 50$ nm) at the point when the leading dislocation in a pile-up can first cross the barrier, strength can be represented by a form of the Hall-Petch relation derived from classical dislocation mechanics,

$$\tau = \tau_0 + \left(\frac{\tau^* \mu b}{\pi(1-\nu)L} \right)^{1/2}, \qquad \text{Equation 37}$$

where τ is applied shear stress, τ_0 is lattice friction stress, μ is shear modulus, ν is Poisson's ratio, L is separation distance between the dislocation source and barrier ($L \approx h$ in the case of multilayer films), and τ^* is critical stress for slip transmission of a dislocation across a barrier [3]. The rightmost term can be rearranged as

$$\tau^* = \frac{k^2 \pi(1-\nu)}{\mu b}, \qquad \text{Equation 38}$$

where *k* is the Hall-Petch slope. Since the experimentally obtained Hall-Petch slope (when *h* ≥ 50 nm) is a measure of the barrier strength of the obstacles, it can be used to estimate τ^* in the limit where *L* is too small to prohibit the pile-up of more than one dislocation. With μ_{Al} = 26 GPa and ν_{Al} = 0.35, we find that $\tau^* \approx 0.31$ GPa, corresponding to a peak hardness of ~ 2.50 GPa (approximated by the Tabor relation [137], $H \approx 2.7\sigma$, and $\sigma \approx 3\tau^*$ using a Taylor factor of 3). This value is much lower than the experimentally measured maximum hardness of ~ 5.5 GPa. Such a large discrepancy indicates that mechanisms other than layer interfaces contribute to maximum hardness of Ag/Al multilayer films.

At smaller *h* (5-50 nm), conventional dislocation pile-up becomes increasingly difficult. In this regime, multilayer film strength can be modeled by the CLS mechanism

$$\tau_{CLS} = \frac{\mu b}{8\pi h'} \left(\frac{4-\nu}{1-\nu} \right) \ln\left(\frac{\alpha h'}{b} \right), \qquad \text{Equation 39}$$

where *h'* is layer thickness measured parallel to the glide plane, α is a core cutoff parameter (usually ≈ 1 for a compact core), and *b* is Burgers vector [3]. Equation 39 predicts a τ_{CLS} of 1

GPa (or hardness of ~ 8 GPa) when h = 5 nm, which is much greater than the measured indentation hardness, ~ 3.2 GPa. In the Cu/Nb multilayer system, a better estimation was developed by considering finer details of the interface stress state, namely the characteristic interface stress arising from elastic deformation at the interfaces and stress fields arising from dislocation arrays along the interfaces [3]. Interface stress in the Ag/Al system was not addressed in this study and is a subject of future investigation.

Peak hardness in multilayer films typically occurs when h is several nm, and it is determined by the interfaces' ability to impede dislocation transmission. Relevant factors include Koehler stress [88], chemical mismatch [91], the so-called ω interaction (related to slip system continuity across the interface) [89], coherency stress [89], and interface stresses arising from misfit dislocations [90]. Coherency stress makes only small contributions to strength in the Cu/Ni system once h is small enough to allow fully coherent interfaces [89]. Hence, the smaller lattice mismatch in the Ag/Al system (< 1%) than in Cu/Ni (~ 2.6%) implies that the magnitude of the coherency stress is even smaller. As Ag/Al multilayer films have predominantly coherent interfaces even at large h, misfit dislocations also make negligible contributions to hardening. We now attempt to understand the high hardness achieved in the Ag/Al system from the remaining factors that influence τ^*:

$$\tau^* = \tau_K^* + \tau_{ch}^* + \tau_\omega^* . \qquad \text{Equation 40}$$

Here τ_K^* is Koehler stress, τ_{ch}^* is the chemical interaction, and τ_ω^* is the ω interaction. The first term, τ_K^*, arises from the elastic modulus mismatch between the two components. As dislocations approach the harder layer from the softer layer, the image force repels the dislocation with a stress [88]

$$\tau_K^* = \frac{\mu_1(\mu_2 - \mu_1)b}{4\pi(\mu_2 + \mu_1)h}. \qquad \text{Equation 41}$$

Due to the small shear modulus mismatch between Ag and Al (30 and 26 GPa, respectively), τ_K^* is only 0.0004 GPa when h = 100 nm, and only rises to 0.04 GPa when h = 1 nm. This is in contrast to the Cu/Ni multilayer system, wherein the disparate moduli (48 and 76 GPa) result in a much larger τ_K^*, ranging from 0.002 to 0.22 GPa for similar h. Additionally, at small h, τ_K^* is expected to drop since the dislocation core dimension approaches h [89].

The chemical mismatch term, τ_{ch}^*, arises from the stacking fault energy difference, $\delta\gamma$, between the two components, and is approximated by [89]

$$\tau_{ch}^* \approx \frac{\delta\gamma}{b}. \qquad \text{Equation 42}$$

The γ_{sf} of Al is much higher than that of Ag (165 vs. 22 mJ/m^2) [22]. Hence, we obtain a τ_{ch}^* of ~ 0.5 GPa, much greater than τ_K^*. In Cu/Ni films, the γ_{sf} difference is smaller and τ_{ch}^* is ~ 0.4 GPa, comparable to τ_K^*. Hence τ_{ch}^* may make significant contributions to film strength.

Twin boundaries and SFs can contribute to τ^* by interfering with slip plane continuity at the interface. Previous molecular dynamics simulations have shown that the resistance of twinned interfaces to dislocations in the Cu/Ni system can reach 0.03 to 0.04 μ, making τ_ω^* 3 to 4 times greater than τ_K^* [89]. If a similar relation is assumed in the Ag/Al system, we can estimate τ_ω^* to be ~ 0.1 GPa. Hence τ^* is estimated to be ~ 0.65 GPa for an Ag/Al interface when $h = 1$ nm, and the corresponding peak hardness based on this analysis is ~ 5.2 GPa, similar to the experimental observations.

Twin boundaries and SFs within layers can block dislocation transmission with strength similar to grain boundaries [30]. Additionally, we consider resistance to lateral propagation of SFs along directions parallel to layer interfaces. It has been shown that the critical stress to nucleate a partial dislocation in Al is only ~ 200 MPa [177]. However, when a partial dislocation propagating on lateral {111} glide planes encounters a SF, it experiences increasing resistance. One likely scenario is that the SF constricts back to a full mobile dislocation. However, a repulsive force between two parallel partials bounding the SF exists, which (assuming a pair of 60° partials of edge character) can be estimated as

$$\tau = \frac{\mu b^2 (2+\nu)}{8\pi(1-\nu)w}, \qquad \text{Equation 43}$$

where w is SF width [154]. Assuming $w \approx 1$ nm in Al, τ is ~ 1 GPa. This may be an upper-bound estimation as SF width in Al based on experimental observations can be greater than 1 nm. Additionally, shear stress of similar magnitude may lead to ITB migration or dissociation in Al [179].

In nt Cu/Ni films, peak hardness occurred at $h = 2.5$ nm, corresponding to the highest twin density (average twin spacing ~ 3 nm). In these Cu/Ni films twin spacing increased to ~ 6 nm when $h = 1$ nm, the contribution of twin interfaces to hardening decreased, and consequently indentation hardness dropped (see Figure 44) [92, 193]. In Ag/Al films however, average twin spacing was approximately $h/2$ through the entire range studied. Hence, average twin spacing continuously decreased with decreasing h, and correspondingly indentation hardness increased. CTBs and SFs with densities similar to those in Ag/Al films were observed in Cu/330 SS multilayer films [51], another system in which no softening was observed at nanometer-scale h. Indentation modulus remained constant for the h range studied, indicating that elastic hardening associated with the presence of AgAl intermetallic compounds is not measureable [194]. XRD profiles (Figure 41), HAADF-STEM micrographs (Figure 43c), and indentation modulus all suggest insignificant intermixing along layer interfaces, hence, Ag_2Al is likely to play a minor role in hardening, especially at large h.

VI.6 Conclusions

High density growth twins and SFs formed within Al layers in epitaxial Ag/Al multilayer films. SF density in Al increased with decreasing h, while Ag/Al multilayer film hardness increased monotonically up to 5.5 GPa when $h = 1$ nm, in contrast to softening observed in the epitaxial Cu/Ni multilayer system. The high strength achieved in Ag/Al is attributed mainly to the large γ_{sf} difference between Ag and Al, and the resistance of twins and SFs to propagation of partial dislocations.

CHAPTER VII

SUMMARY

In conclusion, several important results stand out. First, nt Ag films with two different orientations were successfully fabricated by magnetron sputtering, and the film microstructures were characterized by TEM and XRD. These films exhibit greatly enhanced hardness in comparison to bulk material. The films also showed orientation-dependent thermal stability, however, both film orientations retain high hardness and relatively small average feature sizes after annealing at high temperatures. A size-dependent barrier strengthening model was developed to explain the mechanical behavior of the films post-annealing.

Most excitingly, nt Al films were synthesized by using nt Ag layers as templates. Thorough investigation of the microstructures of the multilayer films confirmed the formation of CTBs and ITBs in Al, and identified several mechanisms by which twins propagate from Ag into Al during growth. These films also show enhanced hardness, with fine multilayer films showing the most dramatic increase in hardness. The work presented in this dissertation is significant in itself, still, with every success and good result, I have developed more questions about these materials. I hope to continue pursuing a better understanding of the mechanisms active in the formation of these nt microstructures, as well as those governing deformation behavior.

REFERENCES

[1] Hall EO. The deformation and ageing of mild steel: 3. Discussion of results. P Phys Soc Lond B 1951; 64(381): 747-53.

[2] Petch NJ. The cleavage strength of polycrystals. J Iron Steel I 1953; 174(1): 25-8.

[3] Misra A, Hirth JP, Hoagland RG. Length-scale-dependent deformation mechanisms in incoherent metallic multilayered composites. Acta Mater 2005 Oct; 53(18): 4817-24.

[4] Feynman RP. There's plenty of room at the bottom [data storage]. J Microelectromech S 1992; 1(1): 60-6.

[5] Gleiter H. Nanocrystalline materials. Prog Mater Sci 1989; 33(4): 223-315.

[6] Suryanarayana C. Nanocrystalline materials. Int Mater Rev 1995; 40(2): 41-64.

[7] Weertman JR. Hall-Petch strengthening in nanocrystalline metals. Mat Sci Eng A-Struct 1993 Jul 15; 166(1-2): 161-7.

[8] Meyers MA, Mishra A, Benson DJ. Mechanical properties of nanocrystalline materials. Prog Mater Sci 2006 May; 51(4): 427-556.

[9] Sanders PG, Eastman JA, Weertman JR. Elastic and tensile behavior of nanocrystalline copper and palladium. Acta Mater 1997 Oct; 45(10): 4019-25.

[10] Weertman JR, Farkas D, Hemker K, Kung H, Mayo M, Mitra R, Van Swygenhoven H. Structure and mechanical behavior of bulk nanocrystalline materials. MRS Bull 1999 Feb; 24(2): 44-50.

[11] Koch CC. Optimization of strength and ductility in nanocrystalline and ultrafine grained metals. Scr Mater 2003 Oct; 49(7): 657-62.

[12] Chookajorn T, Murdoch HA, Schuh CA. Design of Stable Nanocrystalline Alloys. Science 2012 Aug 24; 337(6097): 951-4.

[13] Wang J, Anderoglu O, Hirth JP, Misra A, Zhang X. Dislocation structures of Σ3 {112} twin boundaries in face centered cubic metals. Appl Phys Lett 2009 Jul 13; 95(2): 021908.

[14] Ernst F, Finnis MW, Hofmann D, Muschik T, Schonberger U, Wolf U, Methfessel M. Theoretical prediction and direct observation of the 9R structure in Ag. Phys Rev Lett 1992 Jul 27; 69(4): 620-3.

[15] Ichinose H, Ishida Y, Baba N, Kanaya K. Lattice imaging analysis of Σ3 coincidence-site-lattice boundaries in gold. Philos Mag A 1985; 52(1): 51-9.

[16] Wolf U, Ernst F, Muschik T, Finnis MW, Fischmeister HF. The influence of grain-boundary inclination on the structure and energy of Σ=3 grain-boundaries in copper. Philos Mag A 1992 Dec; 66(6): 991-1016.

[17] Carter CB, Medlin DL, Angelo JE, Mills MJ. The 112 lateral twin boundary in FCC materials. Mater Sci Forum 1996; 207: 209-12.

[18] Lucadamo G, Medlin DL. Geometric origin of hexagonal close packing at a grain boundary in gold. Science 2003 May 23; 300(5623): 1272-5.

[19] Medlin DL, Mills MJ, Stobbs WM, Daw MS, Cosandey F. HRTEM observations of a Σ=3 (112) bicrystal boundary in aluminum. Mater Res Soc Symp P 1993; 295: 91-6.

[20] Rittner JD, Seidman DN, Merkle KL. Grain-boundary dissociation by the emission of stacking faults. Phys Rev B 1996 Feb 15; 53(8): R4241-R4.

[21] Wang GJ, Vitek V. A Study of the Dependence of the Structure of Σ = 3 Tilt Boundaries in Gold on the Inclination of the Boundary Plane. Mater Res Soc Symp P 1992; 278: 217-22.

[22] Murr LE. Interfacial Phenomena in Metals and Alloys. Reading, MA.: Addison-Wesley Pub. Co., Advanced Book Program; 1975.

[23] Hirth JP, Lothe J. Theory of Dislocations. New York, NY: McGraw-Hill; 1967.

[24] Zhang X, Misra A, Wang H, Nastasi M, Embury JD, Mitchell TE, Hoagland RG, Hirth JP. Nanoscale-twinning-induced strengthening in austenitic stainless steel thin films. Appl Phys Lett 2004 Feb 16; 84(7): 1096-8.

[25] Zhang X, Misra A, Wang H, Lima AL, Hundley MF, Hoagland RG. Effects of deposition parameters on residual stresses, hardness and electrical resistivity of nanoscale twinned 330 stainless steel thin films. J Appl Phys 2005; 97(094302): 5.

[26] Zhu T, Li J, Samanta A, Kim HG, Suresh S. Interfacial plasticity governs strain rate sensitivity and ductility in nanostructured metals. P Natl Acad Sci USA 2007 Feb 27; 104(9): 3031-6.

[27] Jin ZH, Gumbsch P, Albe K, Ma E, Lu K, Gleiter H, Hahn H. Interactions between non-screw lattice dislocations and coherent twin boundaries in face-centered cubic metals. Acta Mater 2008 Mar; 56(5): 1126-35.

[28] Jin ZH, Gumbsch P, Ma E, Albe K, Lu K, Hahn H, Gleiter H. The interaction mechanism of screw dislocations with coherent twin boundaries in different face-centred cubic metals. Scr Mater 2006 Mar; 54(6): 1163-8.

[29] Wang J, Li N, Anderoglu O, Zhang X, Misra A, Huang JY, Hirth JP. Detwinning mechanisms for growth twins in face-centered cubic metals. Acta Mater 2010 Apr; 58(6): 2262-70.

[30] Lu L, Shen YF, Chen XH, Qian LH, Lu K. Ultrahigh strength and high electrical conductivity in copper. Science 2004 Apr 16; 304(5669): 422-6.

[31] Ni S, Wang YB, Liao XZ, Figueiredo RB, Li HQ, Ringer SP, Langdon TG, Zhu YT. The effect of dislocation density on the interactions between dislocations and twin boundaries in nanocrystalline materials. Acta Mater 2012 Apr; 60(6-7): 3181-9.

[32] Lu K, Lu L, Suresh S. Strengthening materials by engineering coherent internal boundaries at the nanoscale. Science 2009 Apr 17; 324(5925): 349-52.

[33] Lu L, Chen X, Huang X, Lu K. Revealing the maximum strength in nanotwinned copper. Science 2009 Jan 30; 323(5914): 607-10.

[34] Wang YB, Sui ML. Atomic-scale in situ observation of lattice dislocations passing through twin boundaries. Appl Phys Lett 2009 Jan 12; 94(2).

[35] Wang YB, Sui ML, Ma E. In situ observation of twin boundary migration in copper with nanoscale twins during tensile deformation. Phil Mag Lett 2007; 87(12): 935-42.

[36] Li N, Wang J, Huang JY, Misra A, Zhang X. Influence of slip transmission on the migration of incoherent twin boundaries in epitaxial nanotwinned Cu. Scr Mater 2011 Jan; 64(2): 149-52.

[37] Li N, Wang J, Misra A, Zhang X, Huang JY, Hirth JP. Twinning dislocation multiplication at a coherent twin boundary. Acta Mater 2011 Sep; 59(15): 5989-96.

[38] Li N, Wang J, Zhang X, Misra A. In-situ TEM study of dislocation-twin boundaries interaction in nanotwinned Cu films. Jom-Us 2011 Sep; 63(9): 62-73.

[39] Yamakov V, Wolf D, Phillpot SR, Gleiter H. Deformation twinning in nanocrystalline Al by molecular dynamics simulation. Acta Mater 2002 Dec 3; 50(20): 5005-20.

[40] Yamakov V, Wolf D, Phillpot SR, Mukherjee AK, Gleiter H. Dislocation processes in the deformation of nanocrystalline aluminium by molecular-dynamics simulation. Nat Mater 2002 Sep; 1(1): 45-8.

[41] Kulkarni Y, Asaro RJ. Are some nanotwinned fcc metals optimal for strength, ductility and grain stability? Acta Mater 2009 Sep; 57(16): 4835-44.

[42] Froseth A, Van Swygenhoven H, Derlet PM. The influence of twins on the mechanical properties of nc-Al. Acta Mater 2004 May 3; 52(8): 2259-68.

[43] Froseth AG, Derlet PM, Van Swygenhoven H. Grown-in twin boundaries affecting deformation mechanisms in nc-metals. Appl Phys Lett 2004 Dec 13; 85(24): 5863-5.

[44] Li X, Wei Y, Lu L, Lu K, Gao H. Dislocation nucleation governed softening and maximum strength in nano-twinned metals. Nature 2010; 464(7290): 877-80.

[45] Shabib I, Miller RE. Deformation characteristics and stress-strain response of nanotwinned copper via molecular dynamics simulation. Acta Mater 2009 Sep; 57(15): 4364-73.

[46] Wang J, Huang HC. Novel deformation mechanism of twinned nanowires. Appl Phys Lett 2006 May 15; 88(20): 203112.

[47] Sansoz F, Huang HC, Warner DH. An atomistic perspective on twinning phenomena in nano-enhanced fcc metals. Jom-Us 2008 Sep; 60(9): 79-84.

[48] Afanasyev KA, Sansoz F. Strengthening in gold nanopillars with nanoscale twins. Nano Lett 2007 Jul; 7(7): 2056-62.

[49] Dahlgren SD. Columnar grains and twins in high-purity sputter-deposited copper. J Vac Sci Technol 1974; 11(4): 832-6.

[50] Merz MD, Dahlgren SD. Tensile-strength and work-hardening of ultrafine-grained high-purity copper. J Appl Phys 1975; 46(8): 3235-7.

[51] Zhang X, Misra A, Wang H, Shen TD, Nastasi M, Mitchell TE, Hirth JP, Hoagland RG, Embury JD. Enhanced hardening in Cu/330 stainless steel multilayers by nanoscale twinning. Acta Mater 2004 Feb 23; 52(4): 995-1002.

[52] Anderoglu O, Misra A, Wang J, Hoagland RG, Hirth JP, Zhang X. Plastic flow stability of nanotwinned Cu foils. Int J Plasticity 2010 Jun; 26(6): 875-86.

[53] Shute CJ, Myers BD, Xie S, Barbee TW, Hodge AM, Weertman JR. Microstructural stability during cyclic loading of multilayer copper/copper samples with nanoscale twinning. Scr Mater 2009 Jun; 60(12): 1073-7.

[54] Zhang K, Weertman JR, Eastman JA. Rapid stress-driven grain coarsening in nanocrystalline Cu at ambient and cryogenic temperatures. Appl Phys Lett 2005 Aug 8; 87(6).

[55] Weertman JR, Shute CJ, Myers BD, Xie S, Li SY, Barbee TW, Hodge AM. Detwinning, damage and crack initiation during cyclic loading of Cu samples containing aligned nanotwins. Acta Mater 2011 Jun; 59(11): 4569-77.

[56] Askeland DR, Fulay PP. The Science and Engineering of Materials. 4th ed. Pacific Grove, CA: Thomson Brooks/Cole; 2003.

[57] Suresh S, Lu L, Schwaiger R, Shan ZW, Dao M, Lu K. Nano-sized twins induce high rate sensitivity of flow stress in pure copper. Acta Mater 2005 Apr; 53(7): 2169-79.

[58] Lu L, Dao M, Zhu T, Li J. Size dependence of rate-controlling deformation mechanisms in nanotwinned copper. Scr Mater 2009 Jun; 60(12): 1062-6.

[59] Okuda S, Kobiyama M, Inami T, Takamura S. Thermal stability of nanocrystalline gold and copper prepared by gas deposition method. Scr Mater 2001 May 18; 44(8-9): 2009-12.

[60] Islamgaliev RK, Chmelik F, Kuzel R. Thermal structure changes in copper and nickel processed by severe plastic deformation. Mat Sci Eng A-Struct 1997 Aug 30; 234: 335-8.

[61] Gunther B, Kumpmann A, Kunze HD. Secondary recrystallization effects in nanostructured elemental metals. Scripta Metall Mater 1992 Oct 1; 27(7): 833-8.

[62] Xu L, Xu D, Tu KN, Cai Y, Wang N, Dixit P, Pang JHL, Miao JM. Structure and migration of (112) step on (111) twin boundaries in nanocrystalline copper. J Appl Phys 2008 Dec 1; 104(11): 113717.

[63] Zhang X, Misra A. Superior thermal stability of coherent twin boundaries in nanotwinned metals. Scr Mater 2012 Jun; 66(11): 860-5.

[64] Anderoglu O, Misra A, Wang H, Zhang X. Thermal stability of sputtered Cu films with nanoscale growth twins. J Appl Phys 2008 May 1; 103(9): 094322.

[65] Zhang X, Misra A, Wang H, Swadener JG, Lima AL, Hundley MF, Hoagland RG. Thermal stability of sputter-deposited 330 austenitic stainless-steel thin films with nanoscale growth twins. Appl Phys Lett 2005 Dec 5; 87(23): 233116.

[66] Anderoglu O, Misra A, Ronning F, Wang H, Zhang X. Significant enhancement of the strength-to-resistivity ratio by nanotwins in epitaxial Cu films. J Appl Phys 2009 Jul 15; 106(2): 024313.

[67] Anderoglu O, Misra A, Wang H, Ronning F, Hundley MF, Zhang X. Epitaxial nanotwinned Cu films with high strength and high conductivity. Appl Phys Lett 2008 Aug 25; 93(8): 083108.

[68] Demkowicz MJ, Anderoglu O, Zhang XH, Misra A. The influence of Σ 3 twin boundaries on the formation of radiation-induced defect clusters in nanotwinned Cu. J Mater Res 2011 Jul; 26(14): 1666-75.

[69] Niewczas M, Hoagland RG. Molecular dynamic studies of the interaction of a/6112 Shockley dislocations with stacking fault tetrahedra in copper. Part II: Intersection of stacking fault tetrahedra by moving twin boundaries. Philos Mag 2009; 89(8): 727-46.

[70] Yu KY, Bufford D, Sun C, Liu Y, Wang H, Kirk MA, Li M, Zhang X. Removal of stacking-fault tetrahedra by twin boundaries in nanotwinned metals. Nat Commun 2013; 4: 1377.

[71] Tadmor EB, Hai S. A Peierls criterion for the onset of deformation twinning at a crack tip. J Mech Phys Solids 2003 May; 51(5): 765-93.

[72] Bernstein N, Tadmor EB. Tight-binding calculations of stacking energies and twinnability in fcc metals. Phys Rev B 2004 Mar; 69(9).

[73] Tadmor EB, Bernstein N. A first-principles measure for the twinnability of FCC metals. J Mech Phys Solids 2004 Nov; 52(11): 2507-19.

[74] Chen MW, Ma E, Hemker KJ, Sheng HW, Wang YM, Cheng XM. Deformation twinning in nanocrystalline aluminum. Science 2003 May 23; 300(5623): 1275-7.

[75] Li BQ, Sui ML, Li B, Ma E, Mao SX. Reversible twinning in pure aluminum. Phys Rev Lett 2009 May 22; 102(20): 205504.

[76] Liao XZ, Zhou F, Lavernia EJ, He DW, Zhu YT. Deformation twins in nanocrystalline Al. Appl Phys Lett 2003 Dec 15; 83(24): 5062-4.

[77] Zhu YTT. Deformation twinning in nanocrystalline fcc copper and aluminum. Nanostructured Materials by High-Pressure Severe Plastic Deformation 2006; 212: 3-11.

[78] Christian JW, Mahajan S. Deformation Twinning. Prog Mater Sci 1995; 39(1-2): 1-157.

[79] Zhu YT, Liao XZ, Wu XL. Deformation twinning in nanocrystalline materials. Prog Mater Sci 2012 Jan; 57(1): 1-62.

[80] Bufford D, Wang H, Zhang X. High strength, epitaxial nanotwinned Ag films. Acta Mater 2011 Jan; 59(1): 93-101.

[81] Suzuki H. Segregation of solute atoms to stacking faults. J Phys Soc JPN 1962; 17(2): 322-5.

[82] Moroz PJ, Taggart R, Polonis DH. Defect structures in low stacking-fault energy Cu-Ge solid-solutions. Mater Sci Eng 1986 May; 79(2): 201-10.

[83] Hirsch J, Lucke K. Deformation mechanisms, microstructure, development, and grain orientation in rolled Cu-aloys. Strength of Metals and Alloys (ICSMA 6) 1983: 965-70.

[84] Zhao YH, Bingert JE, Liao XZ, Cui BZ, Han K, Sergueeva AV, Mukherjee AK, Valiev RZ, Langdon TG, Zhu YTT. Simultaneously increasing the ductility and strength of ultra-fine-grained pure copper. Adv Mater 2006 Nov 17; 18(22): 2949-53.

[85] Zhao YH, Zhu YT, Liao XZ, Horita Z, Langdon TG. Tailoring stacking fault energy for high ductility and high strength in ultrafine grained Cu and its alloy. Appl Phys Lett 2006 Sep 18; 89(12).

[86] Anderson PM, Foecke T, Hazzledine PM. Dislocation-based deformation mechanisms in metallic nanolaminates. MRS Bull 1999 Feb; 24(2): 27-33.

[87] Li QZ, Anderson PM. Dislocation-based modeling of the mechanical behavior of epitaxial metallic multilayer thin films. Acta Mater 2005 Feb; 53(4): 1121-34.

[88] Koehler JS. Attempt to design a strong solid. Phys Rev B 1970; 2(2): 547-51.

[89] Rao SI, Hazzledine PM. Atomistic simulations of dislocation-interface interactions in the Cu-Ni multilayer system. Philos Mag A 2000 Sep; 80(9): 2011-40.

[90] Frank FC, Vandermerwe JH. One-dimensional dislocations: 2. Misfitting monolayers and oriented overgrowth. Proc R Soc Lon Ser-A 1949; 198(1053): 216-25.

[91] Vitek V. Theory of core structures of dislocations in body-centered cubic metals. Cryst Latt Def Amorp 1974; 5(1): 1-34.

[92] Liu Y, Bufford D, Wang H, Sun C, Zhang X. Mechanical properties of highly textured Cu/Ni multilayers. Acta Mater 2011 Mar; 59(5): 1924-33.

[93] Freund LB, Suresh S. Thin Film Materials: Stress, Defect Formation, and Surface Evolution. New York, NY: Cambridge University Press; 2009.

[94] Ohring M. The Materials Science of Thin Films: Deposition and Structure. 2nd ed. San Diego: Academic Press; 2002.

[95] Narayan J, Larson BC. Domain epitaxy: A unified paradigm for thin film growth. J Appl Phys 2003 Jan 1; 93(1): 278-85.

[96] Modlinski R, Ratchev P, Witvrouw A, Puers R, De Wolf I. Creep-resistant aluminum alloys for use in MEMS. J Micromech Microeng 2005 Jul; 15(7): S165-S70.

[97] Curran JE, Page JS, Pick U. The influence of some evaporation parameters on the structure and properties of thin aluminum films. Thin Solid Films 1982; 97(3): 259-76.

[98] Ma ZQ, Was GS. Aluminum metallization for flat-panel displays using ion-beam-assisted physical vapor deposition. J Mater Res 1999 Oct; 14(10): 4051-61.

[99] Van Gils S, Dimogerontakis T, Buytaert G, Stijns E, Terryn H, Skeldon P, Thompson GE, Alexander MR. Optical properties of magnetron-sputtered and rolled aluminum. J Appl Phys 2005 Oct 15; 98(8).

[100] Younse JM. Mirrors on a chip. IEEE Spectrum 1993 Nov; 30(11): 27-31.

[101] Freundchen. Bragg XRD. Wikimedia Commons; 2012 [cited 2013 May]; X-ray diffraction schematic). Available from: http://commons.wikimedia.org/wiki/File:Bragg_XRD.svg.

[102] Bragg WL, Thomson JJ. The diffraction of short electromagnetic waves by a crystal. P Camb Philos Soc 1914 May; 17: 43-57.

[103] Gringer. Scheme TEM en. Wikimedia Commons; 2009 [cited 2013 May]; TEM component schematic). Available from: http://commons.wikimedia.org/wiki/File:Scheme_TEM_en.svg.

[104] Oh SH, Legros M, Kiener D, Dehm G. In situ observation of dislocation nucleation and escape in a submicrometre aluminium single crystal. Nat Mater 2009 Feb; 8(2): 95-100.

[105] Kacher JP, Liu GS, Robertson IM. Visualization of grain boundary/dislocation interactions using tomographic reconstructions. Scr Mater 2011 Apr; 64(7): 677-80.

[106] Kiener D, Hosemann P, Maloy SA, Minor AM. In situ nanocompression testing of irradiated copper. Nat Mater 2011 Aug; 10(8): 608-13.

[107] Williams DB, Carter CB, SpringerLink (Online service). Transmission Electron Microscopy: A Textbook for Materials Science. Boston, MA: Springer US; 2009. Available from: http://dx.doi.org/10.1007/978-0-387-76501-3.

[108] Pharr GM, Oliver WC, Brotzen FR. On the generality of the relationship among contact stiffness, contact area, and elastic-modulus during indentation. J Mater Res 1992 Mar; 7(3): 613-7.

[109] Chen Y, Bakshi SR, Agarwal A. Correlation between nanoindentation and nanoscratch properties of carbon nanotube reinforced aluminum composite coatings. Surf Coat Tech 2010 May 15; 204(16-17): 2709-15.

[110] Chen XH, Lu L, Lu K. Electrical resistivity of ultrafine-grained copper with nanoscale growth twins. J Appl Phys 2007 Oct 15; 102(8): 083708.

[111] Zhang X, Wang H, Chen XH, Lu L, Lu K, Hoagland RG, Misra A. High-strength sputter-deposited Cu foils with preferred orientation of nanoscale growth twins. Appl Phys Lett 2006 Apr 24; 88(17): 173116.

[112] Zhang X, Anderoglu O, Hoagland RG, Misra A. Nanoscale growth twins in sputtered metal films. Jom-Us 2008 Sep; 60(9): 75-8.

[113] Zepeda-Ruiz LA, Sadigh B, Biener J, Hodge AM, Hamza AV. Mechanical response of freestanding Au nanopillars under compression. Appl Phys Lett 2007 Sep 3; 91(10): 101907.

[114] Lu L, Zhu T, Shen YF, Dao M, Lu K, Suresh S. Stress relaxation and the structure size-dependence of plastic deformation in nanotwinned copper. Acta Mater 2009 Oct; 57(17): 5165-73.

[115] Wang J, Li N, Anderoglu O, Zhang X, Misra A, Huang JY, Hirth JP. Detwinning mechanisms for growth twins in face-centered cubic metals. Acta Materialia 2010; 58: 2262–70.

[116] Han K, Hirth JP, Embury JD. Modeling the formation of twins and stacking faults in the Ag-Cu system. Acta Mater 2001 May 25; 49(9): 1537-40.

[117] Legoues FK, Liehr M, Renier M, Krakow W. Microstructure of epitaxial Ag/Si(111) and Ag/Si(100) interfaces. Philos Mag B 1988 Feb; 57(2): 179-89.

[118] Pharr GM, Oliver WC. Nanoindentation of silver-relations between hardness and dislocation-structure. J Mater Res 1989 Jan-Feb; 4(1): 94-101.

[119] Fu YQ, Shearwood C, Xu B, Yu LG, Khor KA. Characterization of spark plasma sintered Ag nanopowders. Nanotechnology 2010 Mar 19; 21(11): 1-7.

[120] Panin AV, Shugurov AR, Oskomov KV. Mechanical properties of thin Ag films on a silicon substrate studied using the nanoindentation technique. Phys Solid State 2005; 47(11): 2055-9.

[121] Cao YF, Allameh S, Nankivil D, Sethiaraj S, Otiti T, Soboyejo W. Nanoindentation measurements of the mechanical properties of polycrystalline Au and Ag thin films on silicon substrates: Effects of grain size and film thickness. Mat Sci Eng A-Struct 2006 Jul 15; 427(1-2): 232-40.

[122] Park KH, Jin HS, Luo L, Gibson WM, Wang GC, Lu TM. Epitaxial growth of thick Ag/Si(111) films. Mater Res Soc Symp P 1988; 102: 271-4.

[123] Park KH, Smith GA, Rajan K, Wang GC. Interface characterization of epitaxial Ag films on Si(100) and Si(111) grown by molecular-beam epitaxy. Metall Trans A 1990 Sep; 21(9): 2323-32.

[124] Nason TC, You L, Lu TM. Room-Temperature Epitaxial-Growth of Ag on Low-Index Si Surfaces by a Partially Ionized Beam. J Appl Phys 1992 Jul 15; 72(2): 466-70.

[125] Hata A, Akimoto K, Horii S, Emoto T, Ichimiya A, Tajiri H, Takahashi T, Sugiyama H, Zhang X, Kawata H. Crystal orientation of silver films on silicon surfaces revealed by surface X-ray diffraction. Surf Rev Lett 2003 Apr-Jun; 10(2-3): 431-4.

[126] Mckinley A, Williams RH, Parke AW. Investigation of thin silver films on cleaved silicon surfaces. J Phys C Solid State 1979; 12(12): 2447-63.

[127] Pronin II, Faradzhev NS, Gomoyunova MV. Visualization of the reconstruction of a silver film on silicon. Tech Phys Lett 1997 Feb; 23(2): 142-3.

[128] Masten A, Wissmann P. Ellipsometric studies on thin silver films epitaxially grown on Si(111). Thin Solid Films 1999 Apr; 343: 187-90.

[129] Ichimiya A, Iwashige H, Lijadi M. Epitaxial growth of silver on an Si(111) root 3x root 3 Au surface at room temperature. Thin Solid Films 1996 Aug 1; 282(1-2): 36-8.

[130] Marechal N, Quesnel E. Silver thin-films deposited by magnetron sputtering. Thin Solid Films 1994 Apr 1; 241(1-2): 34-8.

[131] Qin XY, Wu XJ, Zhang LD. The microhardness of nanocrystalline silver. Nanostruct Mater 1995 Jan; 5(1): 101-10.

[132] Kizuka T, Ichinose H, Ishida Y. Structure and hardness of nanocrystalline silver. J Mater Sci 1997 Mar 15; 32(6): 1501-7.

[133] Kobelev NP, Soiver YM, Andrievskii RA, Gunter B. Microhardness and elastic properties of nanocrystalline silver. Fiz Tverd Tela 1994 Jan; 36(1): 216-22.

[134] Christopher D, Smith R, Richter A. Atomistic modelling of nanoindentation in iron and silver. Nanotechnology 2001 Sep; 12(3): 372-83.

[135] Zhao MH, Slaughter WS, Li M, Mao SX. Material-length-scale-controlled nanoindentation size effects due to strain-gradient plasticity. Acta Mater 2003 Sep 3; 51(15): 4461-9.

[136] Fu YS, C; Xu, B; Yu, L.G.; Khor, K.A. Characterization of spark plasma sintered Ag nanopowders. Nanotechnology 2010; 21(11).

[137] Tabor D. The Hardness of Metals: Oxford University Press; 2000.

[138] Mata M, Anglada M, Alcala J. Contact deformation regimes around sharp indentations and the concept of the characteristic strain. J Mater Res 2002 May; 17(5): 964-76.

[139] Babyak WJ, Rhines FN. The relationship between the boundary area and hardness of recrystallized cartridge brass. T Am I Min Met Eng 1960; 218(1): 21-3.

[140] Lu L, Shen YF, Dao M, Suresh S. Strain rate sensitivity of Cu with nanoscale twins. Scr Mater 2006 Aug; 55(4): 319-22.

[141] Suresh S, Dao M, Lu L, Shen YF. Strength, strain-rate sensitivity and ductility of copper with nanoscale twins. Acta Mater 2006 Dec; 54(20): 5421-32.

[142] Weertman JR, Shute CJ, Myers BD, Xie S, Barbee TW, Hodge AM. Microstructural stability during cyclic loading of multilayer copper/copper samples with nanoscale twinning. Scr Mater 2009 Jun; 60(12): 1073-7.

[143] Gu P, Dao M, Asaro RJ, Suresh S. A unified mechanistic model for size-dependent deformation in nanocrystalline and nanotwinned metals. Acta Materialia 2011 Oct; 59(18): 6861-8.

[144] Koch CC, Morris DG, Lu K, Inoue A. Ductility of nanostructured materials. MRS Bull 1999 Feb; 24(2): 54-8.

[145] Medlin DL, Campbell GH, Carter CB. Stacking defects in the 9R phase at an incoherent twin boundary in copper. Acta Mater 1998 Sep 1; 46(14): 5135-42.

[146] Liu L, Wang J, Gong SK, Mao SX. High resolution transmission electron microscope observation of zero-strain deformation twinning mechanisms in Ag. Phys Rev Lett 2011 Apr 29; 106(17).

[147] Carter CB, Medlin DL, Angelo JE, Mills MJ. The 112 lateral twin boundary in FCC materials. Mater Sci Forum 1996; 207: 209-12.

[148] Nason TC, Yang GR, Park KH, Lu TM. Study of silver diffusion into Si(111) and SiO_2 at moderate temperatures. J Appl Phys 1991 Aug 1; 70(3): 1392-6.

[149] Weber L. Equilibrium solid solubility of silicon in silver. Metall Mater Trans A 2002 Apr; 33(4): 1145-50.

[150] Chevalier PY. Thermodynamic evaluation of the Ag-Si system. Thermochim Acta 1988 Aug 5; 130: 33-41.

[151] Rothman SJ, Peterson NL, Robinson JT. Isotope effect for self-diffusion in single crystals of silver. Phys Status Solidi 1970; 39(2): 635-45.

[152] Bihr J, Mehrer H, Maier K. Comparison between microsectioning studies of low-temperature self-diffusion in silver. Phys Status Solidi A 1978; 50(1): 171-8.

[153] Varotsos P, Alexopoulos K. Calculation of diffusion-coefficients at any temperature and pressure from a single measurement:1. Self-diffusion. Phys Rev B 1980; 22(6): 3130-4.

[154] Hull D, Bacon DJ. Introduction to Dislocations. 4th ed. Oxford: Butterworth Heinemann; 2001.

[155] Clarebro LM, Segall RL, Loretto MH. Faulted defects in quenched copper and silver. Philos Mag 1966; 13(126): 1285-91.

[156] Jang DC, Li XY, Gao HJ, Greer JR. Deformation mechanisms in nanotwinned metal nanopillars. Nat Nanotechnol 2012 Sep; 7(9): 594-601.

[157] Singh BN, Foreman AJE, Trinkaus H. Radiation hardening revisited: role of intracascade clustering. J Nucl Mater 1997 Oct; 249(2-3): 103-15.

[158] Taylor GI. The mechanism of plastic deformation of crystals: Part I. Theoretical. Proc R Soc Lon Ser-A 1934 July 2, 1934; 145(855): 362-87.

[159] Grossbeck ML, Maziasz PJ, Rowcliffe AF. Modeling of strengthening mechanisms in irradiated fusion-reactor 1st wall alloys. J Nucl Mater 1992 Sep; 191: 808-12.

[160] Asaro RJ, Suresh S. Mechanistic models for the activation volume and rate sensitivity in metals with nanocrystalline grains and nano-scale twins. Acta Mater 2005 Jul; 53(12): 3369-82.

[161] Gu P, Kad BK, Dao M. A modified model for deformation via partial dislocations and stacking faults at the nanoscale. Scr Mater 2010 Mar; 62(6): 361-4.

[162] McCall JL, Steele J. Practical Applications of Quantitative Metallography. Philadelphia, Pa. (1916 Race St., Philadelphia 19103): American Society for Testing and Materials; 1984.

[163] Zhu B, Asaro RJ, Krysl P, Bailey R. Transition of deformation mechanisms and its connection to grain size distribution in nanocrystalline metals. Acta Mater 2005 Oct; 53(18): 4825-38.

[164] Ma E, Wang YM, Lu QH, Sui ML, Lu L, Lu K. Strain hardening and large tensile elongation in ultrahigh-strength nano-twinned copper. Appl Phys Lett 2004 Nov 22; 85(21): 4932-4.

[165] You ZS, Lu L, Lu K. Temperature effect on rolling behavior of nano-twinned copper. Scr Mater 2010 Mar; 62(6): 415-8.

[166] Qin EW, Lu L, Tao NR, Lu K. Enhanced fracture toughness of bulk nanocrystalline Cu with embedded nanoscale twins. Scr Mater 2009 Apr; 60(7): 539-42.

[167] You ZS, Lu L, Lu K. Tensile behavior of columnar grained Cu with preferentially oriented nanoscale twins. Acta Mater 2011 Oct; 59(18): 6927-37.

[168] Idrissi H, Wang BJ, Colla MS, Raskin JP, Schryvers D, Pardoen T. Ultrahigh strain hardening in thin palladium films with nanoscale twins. Adv Mater 2011 May 10; 23(18): 2119-22.

[169] Van Swygenhoven H, Derlet PM, Froseth AG. Stacking fault energies and slip in nanocrystalline metals. Nat Mater 2004 Jun; 3(6): 399-403.

[170] Li B, Cao BY, Ramesh KT, Ma E. A nucleation mechanism of deformation twins in pure aluminum. Acta Mater 2009 Sep; 57(15): 4500-7.

[171] Daphalapurkar NP, Ramesh KT. Orientation dependence of the nucleation and growth of partial dislocations and possible twinning mechanisms in aluminum. J Mech Phys Solids 2012 Feb; 60(2): 277-94.

[172] Matthews JW, Blakeslee AE. Defects in epitaxial multilayers: 1. Misfit dislocations. J Cryst Growth 1974; 27(Dec): 118-25.

[173] Kisielowski C, Freitag B, Bischoff M, van Lin H, Lazar S, Knippels G, Tiemeijer P, van der Stam M, von Harrach S, Stekelenburg M, Haider M, Uhlemann S, Muller H, Hartel P, Kabius B, Miller D, Petrov I, Olson EA, Donchev T, Kenik EA, Lupini AR, Bentley J, Pennycook SJ, Anderson IM, Minor AM, Schmid AK, Duden T, Radmilovic V, Ramasse QM, Watanabe M, Erni R, Stach EA, Denes P, Dahmen U. Detection of single atoms and buried defects in three dimensions by aberration-corrected electron microscope with 0.5-angstrom information limit. Microsc Microanal 2008 Oct; 14(5): 469-77.

[174] Pennycook SJ, Jesson DE. High-resolution Z-contrast imaging of crystals. Ultramicroscopy 1991 Aug; 37(1-4): 14-38.

[175] Zhu YT, Liao XZ, Srinivasan SG, Zhao YH, Baskes MI, Zhou F, Lavernia EJ. Nucleation and growth of deformation twins in nanocrystalline aluminum. Appl Phys Lett 2004 Nov 22; 85(21): 5049-51.

[176] Zhu YT, Liao XZ, Srinivasan SG, Lavernia EJ. Nucleation of deformation twins in nanocrystalline face-centered-cubic metals processed by severe plastic deformation. J Appl Phys 2005 Aug 1; 98(3).

[177] Kibey S, Liu JB, Johnson DD, Sehitoglu H. Predicting twinning stress in fcc metals: Linking twin-energy pathways to twin nucleation. Acta Mater 2007 Dec; 55(20): 6843-51.

[178] Asaro RJ, Krysl P, Kad B. Deformation mechanism transitions in nanoscale fcc metals. Phil Mag Lett 2003 Dec; 83(12): 733-43.

[179] Wang J, Misra A, Hirth JP. Shear response of Σ3{112} twin boundaries in face-centered-cubic metals. Phys Rev B 2011 Feb 18; 83(6).

[180] Campbell GH, Chan DK, Medlin DL, Angelo JE, Carter CB. Dynamic observation of the FCC to 9R shear transformation in a copper Σ=3 incoherent twin boundary. Scr Mater 1996 Oct 1; 35(7): 837-42.

[181] Elmustafa AA, Stone DS. Size-dependent hardness in annealed and work hardened at-brass and aluminum polycrystalline materials using activation volume analysis. Mater Lett 2003 Jan; 57(5-6): 1072-8.

[182] Doerner MF, Gardner DS, Nix WD. Plastic properties of thin films on substrates as measured by submicron indentation hardness and substrate curvature techniques. J Mater Res 1986; 1(6): 845-51.

[183] Phillips MA, Clemens BM, Nix WD. Microstructure and nanoindentation hardness of Al/Al_3Sc multilayers. Acta Mater 2003 Jun 27; 51(11): 3171-84.

[184] Lim YY, Chaudhri MM, Enomoto Y. Accurate determination of the mechanical properties of thin aluminum films deposited on sapphire flats using nanoindentations. J Mater Res 1999 Jun; 14(6): 2314-27.

[185] Zhang L, Ohmura T, Emura S, Sekido N, Yin FX, Min XH, Tsuzaki K. Evaluation of matrix strength in ultra-fine grained pure Al by nanoindentation. J Mater Res 2009 Sep; 24(9): 2917-23.

[186] Rajulapati KV, Scattergood RO, Murty KL, Duscher G, Koch CC. Effect of Pb on the mechanical properties of nanocrystalline Al. Scr Mater 2006 Jul; 55(2): 155-8.

[187] Sun XK, Cong HT, Sun M, Yang MC. Preparation and mechanical properties of highly densified nanocrystalline Al. Metall Mater Trans A 2000 Mar; 31(3A): 1017-24.

[188] Bufford D, Bi Z, Jia QX, Wang H, Zhang X. Nanotwins and stacking faults in high-strength epitaxial Ag/Al multilayer films. Appl Phys Lett 2012 Nov 26; 101(22).

[189] Rhodes CG, Thompson AW. Composition dependence of stacking-fault energy in austenitic stainless-steels. Metall Trans A 1977; 8(12): 1901-6.

[190] Bufford D, Liu Y, Zhu Y, Bi Z, Jia QX, Wang H, Zhang X. Formation mechanisms of high-density growth twins in aluminum with high stacking fault energy. Mater Res Lett 2013; 1(1): 51-60.

[191] Kim C, Qadri SB, Scanlon MR, Cammarata RC. Low-dimension structural-properties and microindentation studies of ion-beam-sputtered multilayers of Ag/Al films. Thin Solid Films 1994 Mar 15; 240(1-2): 52-5.

[192] Fullerton EE, Schuller IK, Vanderstraeten H, Bruynseraede Y. Structural refinement of superlattices from X-ray-diffraction. Phys Rev B 1992 Apr 15; 45(16): 9292-310.

[193] Liu Y, Bufford D, Rios S, Wang H, Chen J, Zhang JY, Zhang X. A formation mechanism for ultra-thin nanotwins in highly textured Cu/Ni multilayers. J Appl Phys 2012 Apr 1; 111(7).

[194] Kim C, Qadri SB, Tritt TM, Ehrlich AC, Hues SM, Jacobsen RL, Kumar S, Grimsditch M. Structural, elastic and transport-properties of Ag/Al Multilayer thin-films prepared by ion-beam sputtering. Surf Coat Tech 1991 Dec 10; 49(1-3): 143-9.